ornl

OAK
RIDGE
NATIONAL
LABORATORY

UNION
CARBIDE

ORNL/TM-7298

Characterization and Irradiation Performance of HTGR Biso-Coated Fertile Particles in HFIR Experiments HT-28, -29, and -30

E. L. Long, Jr.
P. Krautwasser
R. L. Beatty
M. J. Kania
C. S. Morgan, Jr.
C. S. Yust

OPERATED BY
UNION CARBIDE CORPORATION
FOR THE UNITED STATES
DEPARTMENT OF ENERGY

Printed in the United States of America. Available from
National Technical Information Service
U.S. Department of Commerce
5285 Port Royal Road, Springfield, Virginia 22161
NTIS price codes—Printed Copy: A05 Microfiche A01

This report was prepared as an account of work sponsored by an agency of the United States Government. Neither the United States Government nor any agency thereof, nor any of their employees, makes any warranty, express or implied, or assumes any legal liability or responsibility for the accuracy, completeness, or usefulness of any information, apparatus, product, or process disclosed, or represents that its use would not infringe privately owned rights. Reference herein to any specific commercial product, process, or service by trade name, trademark, manufacturer, or otherwise, does not necessarily constitute or imply its endorsement, recommendation, or favoring by the United States Government or any agency thereof. The views and opinions of authors expressed herein do not necessarily state or reflect those of the United States Government or any agency thereof.

ORNL/TM-7298
Distribution
Category UC-77

Contract No. W-7405-eng-26

METALS AND CERAMICS DIVISION

HTGR BASE TECHNOLOGY PROGRAM

Fueled Graphite Development (189a 01330)

CHARACTERIZATION AND IRRADIATION PERFORMANCE OF HTGR BISO-COATED FERTILE PARTICLES IN HFIR EXPERIMENTS HT-28, -29, and -30

E. L. Long, Jr., P. Krautwasser, R. L. Beatty, M. J. Kania,
C. S. Morgan, Jr., and C. S. Yust

Date Published: July 1980

OAK RIDGE NATIONAL LABORATORY
Oak Ridge, Tennessee 37830
operated by
UNION CARBIDE CORPORATION
for the
DEPARTMENT OF ENERGY

CONTENTS

ABSTRACT 1
INTRODUCTION 1
DESCRIPTION OF CAPSULES 3
PREPARATION OF COATED PARTICLES AND BONDED FUEL RODS 5
Coated Particles 5
Fuel Rods 11
CHARACTERIZATION OF COATINGS 11
Optical Anisotropy 11
Plasma Oxidation Etching 13
Transmission Electron Microscopy 15
Permeability of LTI Coatings 17
Chlorine Leaching 19
Static-Pressure Mercury Intrusion 19
Small-Angle X-Ray Scattering (SAXS) 21
Pore size distribution 22
Comparison of relative volume of pores smaller than 2.5 nm with immersion density 25
Comparison of medium-sized pores with LTI microstructure 25
Comparison of NAF with plasma oxidation results 30
Comparison of NAF with neon permeability of unirradiated coatings 31
Comparison of NAF with static-pressure mercury intrusion measurements 32
Comparison of NAF with hot gaseous chlorine leach analysis 35
CAPSULE, LOADING, OPERATION, FLUENCE, AND BURNUP 37
THERMAL ANALYSIS 37
POSTIRRADIATION EXAMINATION 47
Capsule Disassembly 47
HT-28 47
HT-29 47
HT-30 48
Capsule Gas Sampling 48
Dimensional Measurements 49

Visual Examination 51

Particle Failure Determination for Fuel Rods 51

Fission-Gas Release-to-Birth Ratios, Fission Gas Contents, and Long-Term Chlorine Leaching Studies 57

Permeability of LTI Coatings of Inert Particles in HT-30 59

Other Materials in HT-28 and -29 60

COMPARISON OF NAF WITH IRRADIATION PERFORMANCE 60

PERMEABILITY — GENERAL REMARKS 63

Preirradiation Permeability 63

Irradiation-Induced Permeability 63

CONCLUSIONS 64

ACKNOWLEDGMENTS 65

REFERENCES 66

APPENDIX 71

CHARACTERIZATION AND IRRADIATION PERFORMANCE OF HTGR BISO-COATED FERTILE PARTICLES IN HFIR EXPERIMENTS HT-28, -29, and -30

E. L. Long, Jr., P. Krautwasser,* R. L. Beatty, M. J. Kania, C. S. Morgan, Jr., and C. S. Yust

ABSTRACT

Capsules HT-28, -29, and -30 were irradiated in the target region of the High Flux Isotope Reactor at ORNL to determine the relative fast-neutron stability of pyrolytic carbons that had been prepared in a small laboratory coating furnace with various deposition conditions. The pyrolytic carbon coatings of 22 batches of particles of HTGR design were characterized by various methods, including optical anisotropy measurements, hot gaseous chlorine leaching, plasma oxidation, small-angle x-ray scattering (SAXS) measurements, mercury intrusion, immersion density, and, in a few cases, neon-helium permeability measurements. The results of the above measurements were used to quantify microstructural differences between pyrolytic coatings derived at various conditions and to correlate the performance of the coatings with the measured properties. The most consistent results were obtained by comparing various pore size distributions within the coatings (determined from SAXS measurements) with immersion density, mercury intrusion, chlorine leaching, and neon-helium permeability results and with irradiation performance of the coatings. This study also demonstrated that care must be exercised if experiments on coatings containing inert carbon kernels that were codeposited along with dense thoria kernels are to yield meaningful results.

INTRODUCTION

The release of solid and gaseous fission products from Biso-coated particles depends on the integrity of the outer pyrocarbon coating during irradiation as well as the diffusion coefficients of fission products in the kernel and the coatings. Irradiation experiments suggest that irradiation stability and fission product migration are sensitive to coating

*Institüt für Reactorstoffe, Kernforschungsanlange Jülich, Federal Republic of Germany.

geometry and to the pyrocarbon microstructure. The microstructure in turn is strongly influenced by the deposition conditions.[1] For example, the principal factors that may alter the microstructure significantly are deposition rate and temperature, hydrocarbon gas, gas flux, and fluidization of the fuel kernels.

Irradiation experiments HT-28, -29, and -30 were designed to test the performance of Biso-coated fertile particles that were prepared in a 64-mm (2.5-in.) coater by systematically varying the deposition temperatures and hydrocarbon gas concentrations. Twenty-two batches of particles that had outer low-temperature isotropic (LTI) coatings with subtle differences in microstructure were prepared. The coatings were characterized by various methods, including optical anistropy measurements, hot gaseous chlorine leaching, ceramography, plasma oxidation, small-angle x-ray scattering (SAXS) measurements, mercury intrusion, immersion density, and, in some cases, neon-helium permeability measurements.

The particles were irradiated in both the forms of loose particles and fuel compacts in the flux-trap region of the High Flux Isotope Reactor (HFIR) at ORNL to fluences and temperatures below and exceeding high-temperature reactor (HTR) design requirements. The failure fractions were established during postirradiation examination by visual inspection of the loose particles and by hot gaseous chlorine leaching of a select number of fuel rods. In a few cases the fission-gas inventory of individual fuel particles was determined.

The ultimate goal of these tests was to correlate the irradiation stability of coatings with a set of measurable properties with emphasis on the characterization of microstructural features of pyrocarbon.

A previous series of experiments, HT-17, -18, and -19, was designed specifically to determine limits on coating anisotropy that would allow adequate performance as a function of fast-neutron fluence.[2] However, results of those experiments were ambiguous and did not produce the clear-cut definition of the anisotropy limits desired. Thus, a major conclusion drawn from the above experiments was that characterization methods used and resultant measurements were inadequate to predict irradiation performance.

A performance comparison between particles irradiated in bonded rods and in loose particle holders was a secondary objective of these experiments. A few anomalous results from earlier HFIR target (HT) experiments have raised the question whether coatings may be broken by particle-particle ratchetting from coating dimensional changes during irradiation. The bonded (slug-injected) rods for these tests were intended to provide a more realistic coating test environment.

A third objective of these experiments was the irradiation of coatings that could be examined for microstructural changes induced by the irradiation. For this purpose particles with inert carbon kernels were included in the end plugs of capsule HT-30 at no expense to the capsule fuel capacity. We anticipated that these particles could be removed from the hot cells for evaluation.

DESCRIPTION OF CAPSULES

A typical HT-capsule design is shown in Fig. 1. However, capsules HT-28, -29, and -30 differed with respect to fuel loading, temperature, and fill gas. All test fertile particles for HT-28 and -29 were loaded into annular Poco graphite holders similar to those used in earlier experiments, including HT-17, -18, and -19.[3] Capsules HT-28 and -29 each contained 32 experimental thoria positions, 22 with particles prepared at General Atomic Company (GA) and 10 with particles prepared at ORNL. Both capsules also contained uranium-bearing particles, 6.5% enriched in ^{235}U, for heat generation during the early part of the irradiation. Capsule HT-28 was designed for a four-cycle irradiation. As in the earlier capsules HT-12 through -15 and -17 through -19, the uranium was distributed in 20 annular loose-particle holders and 4 magazine end plugs, and the sealed capsule atmosphere was argon. The particle holder design surface temperatures in HT-28 were 1250°C for the two central magazines and 900°C for the end magazines. Capsule HT-29 was an isothermal design with 900°C holder surface design temperature and was irradiated for five HFIR cycles. The relatively low temperature in HT-29 allowed use of helium, which in turn required a much higher total heavy metal loading. The uranium-containing driver particles and part of the thorium were placed in 20

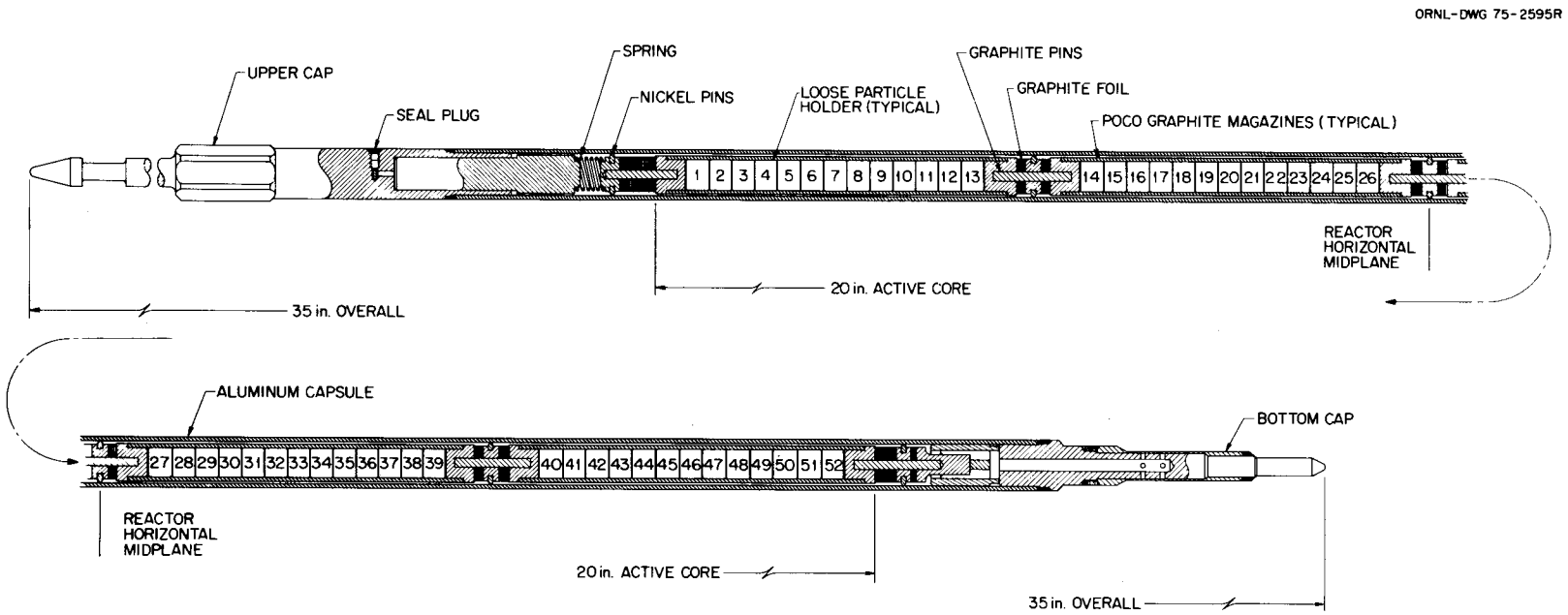

Fig. 1. Design Arrangement for High Flux Isotope Reactor Target Capsules HT-28, -29, and -30 (1 in. = 25.4 mm).

molded rods since the annular machined holders did not have sufficient fuel volume. The inert particles were placed in the end plugs of the Poco graphite magazines to avoid disturbance of the power generation profiles calculated for these capsules.

Capsule HT-30 was designed for a four-cycle irradiation period and contained only coated thoria and inert particles prepared at ORNL. All the test fertile particles were fabricated into bonded rods. The bonded-rod specimens were selected over loose-particle holders to provide more realistic test conditions for this capsule. The test specimens were nominally 9.58 mm in diameter by 6.98 mm long (0.377 by 0.275 in.). The dimensions allowed space for 52 fuel rods, each of which contained only thoria and inert carbon particles. The uranium used in HT-28 and -29 for power generation was deleted from HT-30 to allow approximately 60% increase in capsule thorium loading. Advantages of the increased fertile particle test capacity were considered to outweigh the resulting lower-than-design operating temperatures during the first two irradiation cycles for this capsule. The rod surface design temperatures were 1250°C for the two center magazines and 900°C for the end magazines. The HT-30 atmosphere was neon.

In summary, capsules HT-28 and -29 contained unbonded specimens of fertile particles produced by ORNL and GA. Additional specimens of inert particles with zirconium carbide coatings, wafers of hot-pressed zirconium carbide, and extruded graphite produced by the Los Alamos Scientific Laboratory (LASL) were included as unfueled spacers and in magazine end plugs. Capsule HT-30 contained bonded rods with ORNL fertile particles in all fuel positions and unbonded ORNL inert particles in magazine end plugs.

PREPARATION OF COATED PARTICLES AND BONDED FUEL RODS

Coated Particles

Table 1 shows the conditions and properties of LTI coatings deposited on buffer-coated fertile kernels in a 64-mm (2.5-in.) coating furnace. The grouping in Table 1 shows the multiple combinations of hydrocarbon concentration and deposition rate used in preparing the coating set.

Table 1. Deposition Conditions and Properties of LTI MAPP-Gas[a] Coatings[b] Irradiated in Capsules HT-28, -29, and -30

MAPP Gas		Deposition		Surface Connected Porosity[c] (%)	Density, Mg/m^3			Batch
Concentration (%)	Flux ($m^3/min\text{-}m^2$)	Temperature (°C)	Rate (μm/min)		As Deposited[d]	After 15 min at 1800°C[d]	Corrected[c]	
100	557[e]	1275	23.0	9.62	1.989	2.053	1.855	OR-2275-AHT
100	286[f]	1275	14.1	8.13	1.973	2.019	1.855	OR-2266-HT
100	135[g]	1275	7.3	8.33	1.948	1.982	1.817	OR-2291-HT
100	77[g]	1275	4.9	7.98	1.924	1.975	1.817	OR-2297-HT
100	557[e]	1325	28.0	15.16	1.948	1.957	1.660	OR-2274-HT
100	286[f]	1325	15.7	9.75	1.918	1.949	1.759	OR-2265-HT
100	135[g]	1325	8.6	10.06	1.868	1.882	1.693	OR-2290-HT
100	77[g]	1325	5.6	10.86	1.854	1.898	1.692	OR-2296-AHT
50	293[e]	1275	10.7	5.34	1.974	2.015	1.907	OR-2271-HT
50	143[f]	1275	6.5	5.19	1.966	2.009	1.905	OR-2262-HT
50	68[g]	1275	3.6	4.13	1.934	1.961	1.880	OR-2294-HT
50	38[g]	1275	2.3	4.18	1.888	1.910	1.830	OR-2299-HT
50	293[e]	1325	12.5	7.91	1.884	1.908	1.757	OR-2269-HT
50	143[f]	1325	7.4	5.38	1.853	1.886	1.785	OR-2261-HT
50	68[g]	1325	3.9	5.47	1.813	1.832	1.731	OR-2293-HT
50	38[g]	1325	2.5	4.99	1.806	1.823	1.732	OR-2298-HT
25	146[e]	1275	5.2	3.81	1.968	2.009	1.933	OR-2273-HT
25	73[f]	1275	3.2	3.04	1.950	1.986	1.926	OR-2264-HT
25	34[g]	1275	1.8	3.10	1.897	1.912	1.852	OR-2295-HT
25	146[e]	1325	6.2	4.33	1.840	1.860	1.780	OR-2272-HT
25	73[f]	1325	3.6	3.56	1.816	1.837	1.771	OR-2263-HT
15	84[e]	1275	3.1	3.24	1.945	1.977	1.913	OR-2276-HT

[a]MAPP gas is marketed by Airco, Inc., Murray, N.J., and consists primarily of methylacetylene and propadiene with alkanes as stabilizers.

[b]Biso particles or nominal design 500-μm thoria kernel, 85-μm buffer, 85-μm LTI. Buffer deposited at nominal 24 μm/min from C_2H_2 at 1125°C.

[c]Determined by mercury porosimetry (103 MPa) as percent of LTI volume, assuming 4-μm infiltration of buffer.

[d]Measured by gradient column technique.

[e]High flux obtained by using approximately half usual charge volume.

[f]Typical flux on 350-g, 125-cm^3 charge of buffer-coated fertile particles in 64-mm-ID coating tube.

[g]Low flux obtained for given concentration by diluting bed with low-density carbon particles to reduce fluidizing flow requirement.

Deposition rate depends on all parameters of the system and is a direct function of both hydrocarbon concentration and total gas flux. The workable range of gas flux that can be employed is determined by the particle size and density as well as the batch size and coating chamber geometry. For a given coater, batch size, and fuel type, for example, 500-μm-diam thoria, the deposition rate can be varied by changing only the hydrocarbon concentration. However, since the same coating conditions could not be applied to smaller, lower density fissile particles, comparing coatings on the different particle types on the basis of deposition rate may not be valid. For this reason different fluidizing conditions were used in preparing the coating set: (1) 350-g beds of buffer coated 500-μm-diam thoria kernels were coated; (2) the batch size and surface area were reduced 50% at the same gas flow rates, thereby increasing the gas flux by a factor of 2; (3) the thoria bed was diluted with low-density carbon particles to reduce fluidizing flow requirements, which resulted in approximately the same surface areas but a lower gas flux, as in the first case; and (4) the carbon-diluted batch size was reduced 50% with the same fluidizing gas flow as case (3), which effectively increased the gas flux. In this manner the deposition rate was varied independently of hydrocarbon concentration, thereby simulating the range of coating conditions applicable to both fissile and fertile particles. Coating temperature was also varied, which resulted in different densities. The coatings produced in this manner had a range of properties and microstructures that could be correlated with irradiation performance. These coatings were irradiated at a variety of temperatures and fluences as loose particles and as bonded fuel rods. In addition to the coating set listed in Table 1, capsule HT-30 contained four candidate coatings deposited in a 130-mm-ID (5-in.) prototype coater and one coating produced in a 25-mm-ID (1-in.) coater (previously irradiated without failure[4] in capsules HT-12 through -15) for comparison. These particles, all of the nominal Biso-coated fertile design, are listed in Table 2.

Deposition conditions for the LTI coatings on inert kernels in capsule HT-30 are given in Table 3. Coating properties for both fertile and inert particles are given in Tables 4 and 5, respectively. The loose particles in HT-28 and -29 were loaded into Poco graphite holders.

Table 2. Deposition Conditions and Properties of LTI Propylene Coatings[a] Irradiated in Capsule HT-30

Batch	C_3H_6 Concentration (%)	Deposition		Density[b] After 30 min at 1800°C (Mg/m^3)
		Temperature (°C)	Rate (μm/min)	
OR-1849-HT[c]	75[d]	1300	21.5	1.940
J-488[e]	50[d]	1350	7.2	1.976
J-489[e]	50[d]	1350	5.8	1.904
J-490[e]	100	1350	6.2	1.992
J-491[e]	100	1350	9.1	2.004

[a]Biso particles of nominal design 500-μm thoria kernel, 80-μm buffer, 75-μm LTI.

[b]Measured by gradient column.

[c]Deposited in 25-mm (1-in.) coater. Buffer deposited at 22.7 μm/min from C_2H_2 at 1200°C.

[d]Helium diluent.

[e]Deposited in 0.13-m (5-in.) coater. Buffer deposited at nominal 25 um/min from C_2H_2 at 1350°C.

Table 3. Deposition Conditions for LTI Coatings on Inert Kernels in Capsule HT-30[a,b]

Batch	Outer LTI[c]	
	Temperature (°C)	Deposition Rate (μm/min)
OR-2290-HT	1325	8.6
OR-2291-HT	1275	7.6
OR-2293-HT	1325	3.9
OR-2294-HT	1275	3.3
OR-2295-HT	1275	1.7
OR-2296-AHT	1325	5.2
OR-2297-AHT	1275	4.5
OR-2298-HT	1325	2.4
OR-2299-HT	1275	2.1
OR-2323-AH[d]	1275	7.9

[a]All batches except OR-2323-AH coated in same furnace runs as fertile particles.

[b]All buffer coatings applied with C_2H_2 at 1250°C with a deposition rate of 5.2 μm/min except where noted otherwise.

[c]All coatings applied with MAPP gas, which is marketed by Airco, Inc., Murray, N.J., and consists primarily of methylacetylene and propadiene with alkanes as stabilizers.

[d]Triso coated: buffer deposited at 1275°C with C_2H_2 at 6.1 μm/min. SiC deposited at 1550°C with CH_3SiCl_3 at 0.2 μm/min.

Table 4. Properties of LTI Coatings on Fertile Kernels in Capsules for HT-28, -29, and -30

Batch	Thorium Content (%)	Kernel		Buffer		LTI			
		Diameter[a] (μm)	Density (Mg/m^3)	Thickness[a] (μm)	Density (Mg/m^3)	Thickness[a] (μm)	Density[a,b] (Mg/m^3)		Corrected Density[c] (Mg/m^3)
OR-1849-HT	66.52	508 (1.6)	9.72	79.4 (6.7)	*d*	74.7 (4.3)	1.940	*d*	*d*
OR-2261-HT	53.72	506 (2.5)	10.0	95.8 (10.8)	1.15	88.9 (6.5)	1.886	(0.005)	1.785
OR-2262-HT	52.72	507 (2.5)	10.0	98.0 (13.5)	1.15	85.1 (5.6)	2.009	(0.007)	1.905
OR-2263-HT	53.18	506 (2.9)	10.0	92.8 (10.7)	1.16	90.5 (6.4)	1.837	(0.006)	1.771
OR-2264-HT	52.14	507 (2.4)	10.0	96.5 (11.1)	1.16	91.6 (5.9)	1.986	(0.007)	1.926
OR-2265-HT	52.00	508 (2.6)	10.0	96.1 (13.1)	1.15	94.2 (8.1)	1.949	(0.008)	1.759
OR-2266-HT	52.32	506 (2.6)	10.0	94.8 (15.8)	1.15	91.3 (6.8)	2.019	(0.013)	1.855
OR-2269-HT	55.93	507 (2.4)	10.0	88.8 (10.8)	1.17	81.4 (6.8)	1.908	(0.007)	1.757
OR-2271-HT	55.22	507 (3.1)	10.0	88.6 (14.6)	1.17	80.3 (5.8)	2.015	(0.010)	1.907
OR-2272-HT	55.44	506 (2.2)	10.0	86.8 (13.2)	1.17	83.0 (4.8)	1.860	(0.006)	1.780
OR-2273-HT	54.22	507 (2.3)	10.0	89.2 (7.6)	1.17	83.5 (4.8)	2.009	(0.006)	1.933
OR-2274-HT	53.19	507 (2.5)	10.0	99.7 (12.3)	1.15	90.8 (8.1)	1.957	(0.012)	1.660
OR-2275-AHT	52.88	507 (2.3)	10.0	93.0 (11.1)	1.15	87.4 (8.4)	2.053	(0.009)	1.855
OR-2276-HT	52.54	507 (2.9)	10.0	93.8 (12.6)	1.15	84.7 (4.8)	1.977	(0.009)	1.913
OR-2290-HT	52.98	507 (2.2)	10.0	95.3 (12.4)	1.12	94.4 (6.4)	1.882	(0.008)	1.693
OR-2291-HT	52.34	507 (2.3)	10.0	95.1 (14.9)	1.12	87.6 (5.7)	1.982	(0.007)	1.817
OR-2293-HT	52.78	506 (2.7)	10.0	97.6 (13.9)	1.12	89.0 (5.1)	1.832	(0.004)	1.731
OR-2294-HT	50.57	506 (2.3)	10.0	90.0 (15.6)	1.12	92.7 (7.0)	1.961	(0.007)	1.880
OR-2295-HT	50.93	505 (2.4)	10.0	95.1 (13.0)	1.12	93.1 (6.4)	1.912	(0.011)	1.852
OR-2269-AHT	52.81	506 (2.5)	10.0	97.1 (14.6)	1.12	89.3 (7.5)	1.898	(0.007)	1.692
OR-2297-AHT	51.62	505 (2.6)	10.0	96.5 (12.3)	1.12	90.2 (7.3)	1.975	(0.011)	1.817
OR-2298-HT	54.59	506 (2.5)	10.0	94.5 (14.3)	1.12	84.4 (5.8)	1.823	(0.012)	1.723
OR-2299-HT	51.37	508 (2.4)	10.0	94.5 (13.1)	1.12	91.6 (5.6)	1.910	(0.005)	1.852
J-488	56.85	497.2 (2.7)	9.95	87.4 (18.2)	1.28	78.7 (6.6)	1.976	(0.008)	*d*
J-489	58.46	496.8 (2.2)	9.95	74.7 (13.8)	1.17	76.9 (5.3)	1.904	(0.009)	*d*
J-490	58.42	495.6 (2.8)	9.95	81.7 (15.0)	1.24	74.8 (5.4)	1.922	(0.010)	*d*
J-491	58.22	495.6 (3.1)	9.95	83.8 (13.8)	1.23	75.6 (5.9)	2.004	(0.006)	*d*

[a]Mean values (standard deviations).

[b]Determined by density gradient column.

[c]Determined by mercury porosimetry (103 MPa) as percent of LTI volume, assuming 4-μm infiltration of buffer.

[d]Not determined.

Table 4. Properties of LTI Coatings on Fertile Kernels in Capsules for HT-28, -29, and -30

Batch	Kernel			Buffer			LTI			
	Diameter[a] (μm)		Density (Mg/m^3)	Thickness[a] (μm)		Density (Mg/m^3)	Thickness[a] (μm)		Density[a,b] (Mg/m^3)	
OR-2290-HT[c]	451.2	(27.6)	1.33	83.2	(10.2)	1.14	94.5	(6.7)	1.864	(0.0063)
OR-2291-HT	451.2	(27.6)	1.33	83.2	(10.2)	1.14	91.3	(5.8)	1.948	(0.0053)
OR-2293-HT	451.2	(27.6)	1.33	83.2	(10.2)	1.14	90.2	(5.6)	1.813	(0.0041)
OR-2294-HT	459.8	(29.3)	1.33	81.4	(9.6)	1.13	86.9	(4.3)	1.934	(0.0041)
OR-2295-HT	459.8	(29.3)	1.33	81.4	(9.6)	1.13	90.6	(5.9)	1.987	(0.0035)
OR-2296-HT	344.3	(15.8)	1.43	83.7	(11.0)	0.93	82.7	(5.6)	1.854	(0.0075)
OR-2297-AHT	344.3	(15.8)	1.43	83.7	(11.0)	0.93	83.1	(5.3)	1.924	(0.0074)
OR-2298-HT	338.0	(15.4)	1.43	82.1	(9.7)	0.92	80.6	(4.6)	1.806	(0.0079)
OR-2299-HT[c]	344.3	(15.8)	1.43	83.7	(11.0)	0.93	81.0	(5.6)	1.888	(0.0035)
OR-2323-AH[d]	331.9	(14.5)	1.42	109.1	(13.7)	0.86	51.0	(4.2)	1.980	(0.006)

[a]Mean values (standard deviations).

[b]Determined by density gradient column.

[c]Coated in same furnace runs with fertile particles. (Batches OR-2290-HT through -2299-HT.)

[d]Triso particle: inner LTI thickness = 53.4 μm, density — not determined; SiC thickness = 42.5 μm, density = 3.205 Mg/m^3.

Fuel Rods

The fuel rod specimens for HT-30 were prepared by the slug-injection process. The bonding matrix was composed of 29 wt % grade 6353 natural flake graphite* and 71 wt % A-240 petroleum pitch.† The specimens were formed at 170°C and 4.83 MPa. They were carbonized in graphite powder (for support) at 1000°C, then annealed at 1800°C for 30 min.

CHARACTERIZATION OF COATINGS

Characterization of the coatings involved the efforts of personnel at ORNL; GA, San Diego, California; and Kernforschungsanlange (KFA) Jülich, Federal Republic of Germany. The results from this characterization effort and the existing interrelationships are reported below.

Optical Anisotropy

Optical anisotropy measurements were made on all the LTI coatings used in HT-28, -29, and -30. The coatings were examined by the "Optical Anisotropy Factor" (OAF) technique developed by the Österreichische Studiengesellschaft für Atomenergie (ÖSGAE), Seibersdorf, Austria. The Bacon Anisotropy Factors (BAF_o) were determined optically to permit cross checking with other techniques such as OAF, which is done with air-spaced microscope objectives, or x-ray BAF. The advantages of the ÖSGAE approach lie in the speed of analysis (relative to other techniques) and in the 20 or more anisotropy points that can be established as one performs a radial scan of a single coating. Thus, gradients of anisotropy can be established.

---

*Product of Asbury Graphite Mills, Inc., Asbury, New Jersey 08802.

†Product of Ashland Oil, Inc., P.O. Box 391, Ashland, Kentucky 41101.

The results of optical anisotropy measurements on LTI coatings used in HT-28, -29, and -30 for the undiluted fluidized bed were

Batch	BAF_o
OR-2274-HT	1.033
2275-AHT	1.037
2269-HT	1.032
2265-HT	1.033
2271-HT	
2266-HT	1.037
2272-HT	1.027
2261-HT	1.024
2262-HT	1.026
2273-HT	1.038
2263-HT	1.027
2276-HT	1.048
2264-HT	1.028

The measurements for the diluted fluidized bed were

Batch	BAF_o
OR-2296-AHT	1.037
2290-HT	1.027
2298-HT	1.030
2297-AHT	1.032
2294-HT	1.045
2291-HT	1.033
2293-HT	
2299-HT	1.028
2295-HT	1.048

These results are the mean values of three coatings selected at random and measured with a 4- by 26-μm slit, stepping 4 μm per radial increment.

Duplicate samples polished at ORNL and GA were used in this investigation. The polishing procedure that suffices for the BAF measurements on GA-propylene or mixed-gas coatings was not satisfactory for the coatings from MAPP* gas. Additional polishing was necessary for the GA mount since the coating material was very soft and easily spalled under the action of the diamond paste.

---

*MAPP gas is marketed by Airco, Inc., Murray, New Jersey, and consists primarily of methylacetylene and propadiene with alkanes as stabilizers.

Plasma Oxidation Etching

The structures of the pyrocarbon coatings were revealed through selective etching with an oxygen plasma.[5] This technique was explored in the hope that it could be used to predict the fast-neutron damage resistance of the coatings. Each of the MAPP-gas-derived coatings used in this series of experiments was subjected to this etching technique. Two types of etched structures are normally found in pyrocarbon coatings. One consists of continuous and concentric bands at regular radial intervals across the coating when observed at the particle midplane. In the other the etching is more localized as lenticular regions in the coating at the particle midplane. The type of etch pattern that develops in a given pyrocarbon coating appears to be strongly dependent on the concentration of the deposition gas in the coater. The continuous banded type of structure (considered "poor" structure) was characteristic of coater MAPP-gas concentrations of 15 and 25%, while the localized etching (considered "good" structure) was associated with MAPP-gas concentrations of 50 and 100% [Figs. 2(a) and (b)]. An estimated rating of the performance of the coatings for particles used in capsules HT-28, -29, and -30 with 1 being the best performer and 4 the poorest is listed below. The results for coatings derived in an undiluted fluidized bed were

Batch	Rating
OR-2275-AHT	1
2266-HT	2
2274-HT	1
2265-HT	2
2271-HT	1
2262-HT	3
2269-HT	2
2261-HT	3
2273-HT	2
2264-HT	3
2272-HT	2
2263-HT	1
2276-HT	

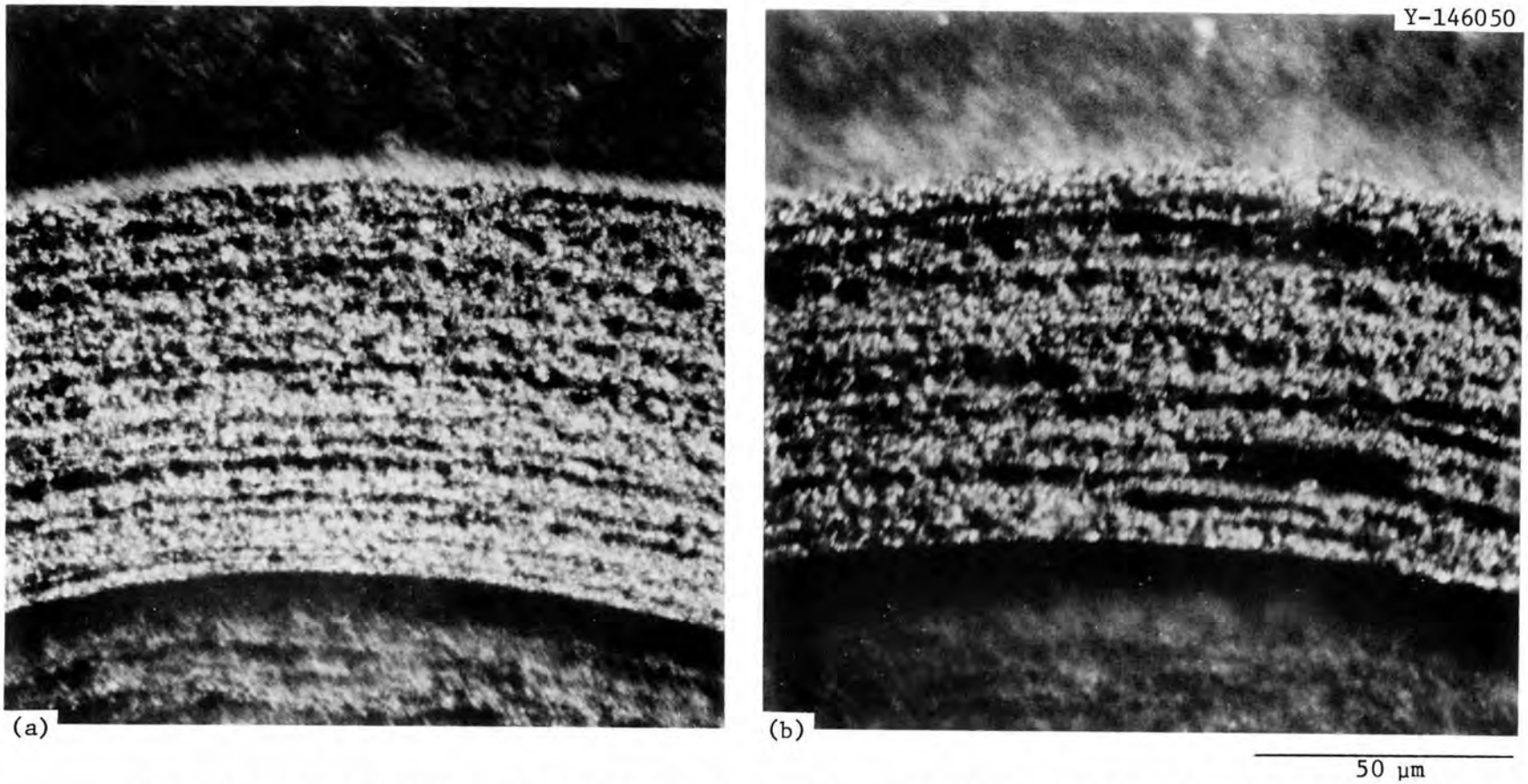

Fig. 2. Plasma Etching. (a) Continuous banded type structure considered "poor." (b) Localized etching type structure considered "good."

The results from coatings derived in a diluted fluidized bed were

Batch	Rating
OR-2291-HT	3
2297-AHT	4
2290-HT	3
2296-HT	3
2294-HT	3
2299-HT	2
2293-HT	3
2298-HT	1
2295-HT	1

Transmission Electron Microscopy

Transmission electron microscopy (TEM) has been utilized as one of the characterization techniques for pyrocarbon coatings. It had been previously determined[6] that the variation in microstructure produced by using a wide range of deposition conditions could be distinguished by TEM examination. Specifically, three different microstructural components were noted, and the extent and distribution of these components could be related to other coating characteristics. Accordingly, the coatings were characterized in the as-deposited condition.

Particles from the following batches were examined by TEM: OR-2265-HT, -2266-HT, -2269-HT, -2271-HT, and -2276-HT derived from MAPP gas and OR-1849-HT, J-488, -489, -490, and -491 derived from propylene. The results show the coatings to be composed of sphere-like growth features similar to those observed in the original study and stacked together to form the coating. The outer portion of each growth consists of a circumferentially aligned layered structure often referred to as "mosaic" structure. The centers of the growth features contain clusters of small spheres having a tangled-fiber appearance (Fig. 3). These small spheres are most likely the nuclei for growth. In general, the agglomeration of growth features that comprises the coating contains many partial features, that is, growth features that are only sectors or spheres. All the coatings examined contained growth features of this type.

Another general characteristic of the coating microstructure is the presence of two size ranges of growth features, possibly resulting from inhomogeneous deposition conditions. This tendency can be distinguished

C 11600

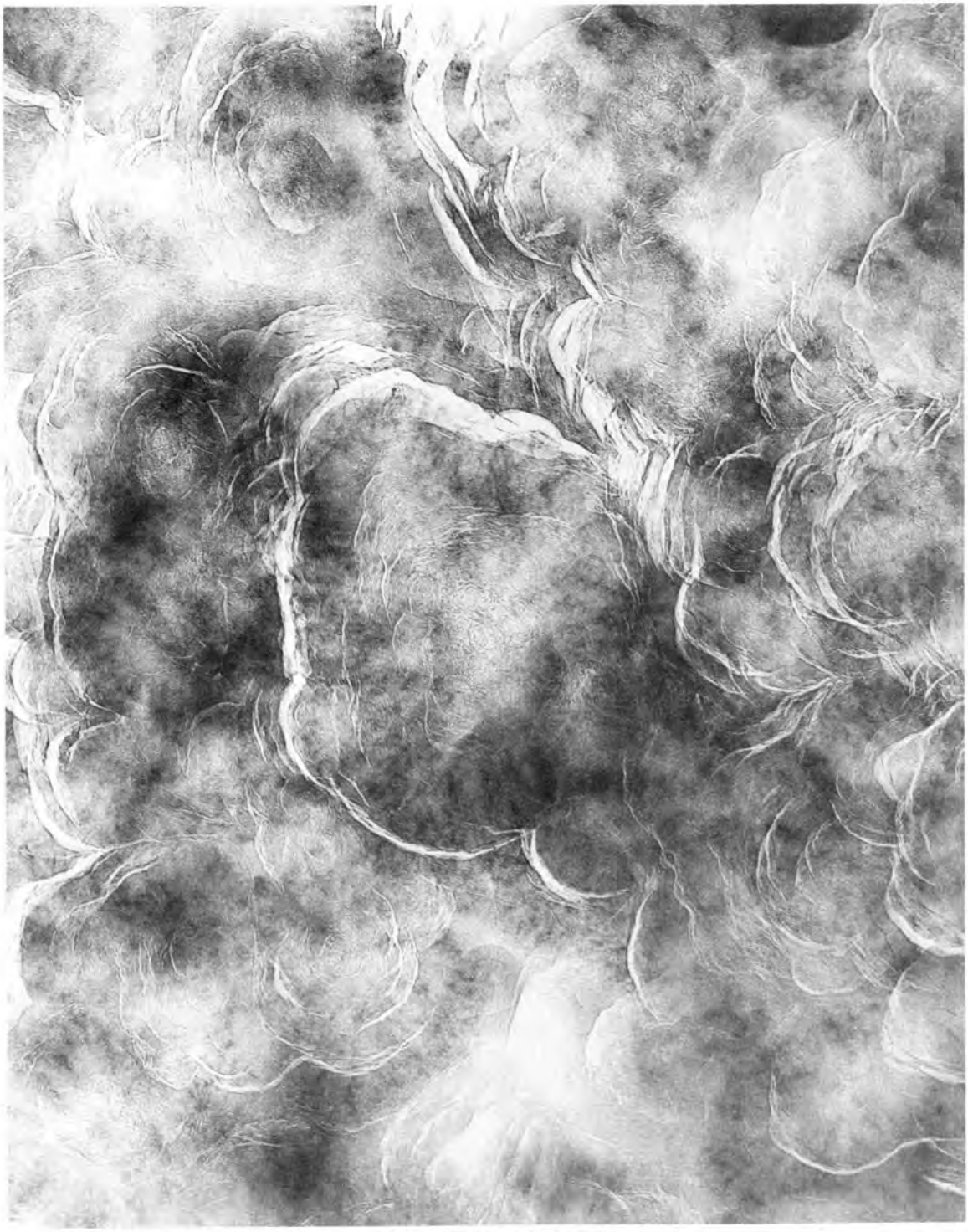

0.5 μm

Fig. 3. Transmission Electron Micrography of Particle Coating Showing Sphere-Like Growth Features.

in the microstructure as bands within which the growth features are predominantly large or small. The resultant inhomogeneous distribution of growth feature sizes may be related to the etch patterns produced by plasma oxidation etching. In general, the growth feature sizes were distinctly smaller in the MAPP-gas-derived coatings than in the propylene-derived coatings.

The coatings considered in this work were all produced in approximately the same temperature range, 1275 to 1350°C. Although coating microstructure can change significantly with deposition temperature, coatings produced within these temperature limits were all very similar in appearance. Coating differences detected by other characterization methods were not discernible by the TEM techniques applied to this study.

Permeability of LTI Coatings

The permeabilities of the LTI coatings on most of the fertile particles and on one batch of inert particles used in HT-28, -29, and -30 were determined on unirradiated samples. The permeabilities were evaluated by heating the particles for 1 h at 1375°C in equal amounts of helium and neon at a total pressure of 0.1 MPa and then by determining the quantity of the gases that had diffused into the void volume, primarily in the buffer layer. The ratio obtained for the quantity of neon and helium in the particle represents a measure of permeability, and these results are given in Table 6. The intrinsic permeability of the pyrocarbon coating can be obtained by accounting for the geometric factors and is represented by

$$F_{\mathrm{Ne}} = (vA/lt)\ \ln(1 - h_{\mathrm{Ne}}/h_{\mathrm{He}})\ ,$$

where

F_{Ne} = admittance factor for neon,

v = void volume of the fuel particle,

A = surface area,

l = LTI thickness,

t = time of heat treatment in the neon-helium atmosphere,

Table 6. Measurement of Permeability of Pyrocarbon Coatings[a]

Batch	Deposition Conditions			Particle Diameter (μm)	LTI Thickness (μm)	He[c] (pmol)	Ne[c] (pmol)	Ne/He Ratio	F_{Ne}[d] (fm^2/s)	Particle Permeability Factor, $F_{Ne}(A/l)$ (fm^3/s)
	Temperature (°C)	MAPP Gas[b] (%)	Coating Rate (μm/min)							
OR-2263-HT	1325	25	3.6	873	90.5	151 (17)	19 (3)	0.13	64	1.67
OR-2276-HT	1275	15	3.1	864	84.7	195 (39)	25 (2)	0.13	78	2.17
OR-2273-HT	1275	25	5.2	852	83.5	163 (22)	23 (3)	0.14	73	2.00
OR-2294-HT	1275	50	3.6	871	92.7	183 (47)	27 (3)	0.15	92	2.37
OR-2299-HT	1275	50	2.3	880	81.0	204 (34)	39 (4)	0.19	114	3.42
OR-2262-HT	1275	50	6.5	873	85.1	166 (38)	33 (4)	0.20	105	2.95
OR-2261-HT	1325	50	7.4	875	88.9	162 (39)	38 (4)	0.23	123	3.33
OR-2271-HT	1275	50	10.7	845	80.3	160 (32)	37 (3)	0.23	119	3.32
OR-2293-HT	1325	50	3.9	879	89.0	163 (25)	38 (4)	0.23	124	3.39
OR-2298-HT	1325	50	2.5	863	84.4	176 (25)	43 (6)	0.24	138	3.83
OR-2297-HT	1275	100	4.9	878	90.2	184 (32)	50 (9)	0.27	172	4.61
OR-2291-HT[c]	1275	100	7.6	872	87.6	153	41	0.27	140	3.82
J-489	1350	50	5.8	800	76.9	133 (34)	37 (11)	0.28	133	3.48
J-490	1350	100	6.2	809	74.8	118 (26)	34 (6)	0.29	117	3.22
OR-2265-HT	1325	100	15.7	889	94.2	167 (24)	54 (10)	0.32	194	5.11
OR-2269-HT	1325	50	12.5	847	81.4	181 (32)	74 (10)	0.41	274	7.6
OR-2275-HT	1275	100	23.0	868	89.4	204 (30)	84 (15)	0.41	315	8.5
OR-2296-HT	1325	100	5.6	879	89.3	216 (37)	96 (14)	0.44	365	9.9
OR-2274-HT	1325	100	28.0	888	90.8	203 (31)	102 (16)	0.50	409	11.2

[a]All fertile particles except as noted.

[b]MAPP gas is marketed by Airco, Inc., Murray, N.J., and consists primarily of methylacetylene and propadiene with alkanes as stabilizers.

[c]Numbers in parentheses are standard deviations.

[d]$F_{Ne} = (vA/lt)\ \ln(1 - h_{Ne}/h_{He})$, where F_{Ne} is an admittance factor for neon, v is the void volume of the fuel particle, A is the surface area, l is the LTI thickness, t is the time of heat treatment in the neon-helium atmosphere, and h_{Ne} and h_{He} are moles of neon and helium gases entering the particles.

h_{Ne} = moles of neon entering the particle,

h_{He} = moles of helium entering the particle.

Another permeability value represented by $F_{Ne}(A/l)$ best represents the ability of the particle to retain a given volume of gas. These values along with particle dimensions and deposition conditions are included in Table 6.

Since particles had similar dimensions the comparative values between batches for F_{Ne} and for $F_{Ne}(A/l)$ are little changed and are relatively similar to the range of values for the neon-to-helium ratios. Permeability tended to increase with deposition rate.

Chlorine Leaching

In an effort to determine if any of the deposition conditions had provided porous coatings, samples of all the Biso-coated fertile particles were evaluated by hot gaseous chlorine leaching at ORNL and GA. Unirradiated particles were chlorine leached at 1500°C with chlorine gas at ORNL,[7] whereas GA employed carbonyl chloride (phosgene) gas at 950°C. The ORNL leaching times ranged from 16 to 32 h, while GA leached samples in 20-min intervals; both facilities used 2 to 3 samples. Batches (OR-2274-HT and -2275-AHT) had permeable coatings. Data obtained by GA is displayed in Fig. 4.

Static-Pressure Mercury Intrusion

The relative volumes of mercury intruded at a pressure of 69 MPa into 2- to 3-g samples of particles from an undiluted fluidized bed were

Batch	Mercury Intrusion (mL/kg particle)	Batch	Mercury Intrusion (mL/kg particle)
OR-2274-HT	27.1	2261-HT	9.7
2275-AHT	16.0	2262-HT	7.8
2269-HT	13.0	2273-HT	6.1
2265-HT	18.3	2263-HT	5.8
2271-HT	9.7	2276-HT	6.4
2266-HT	13.6	2264-HT	5.4
2272-HT	7.0		

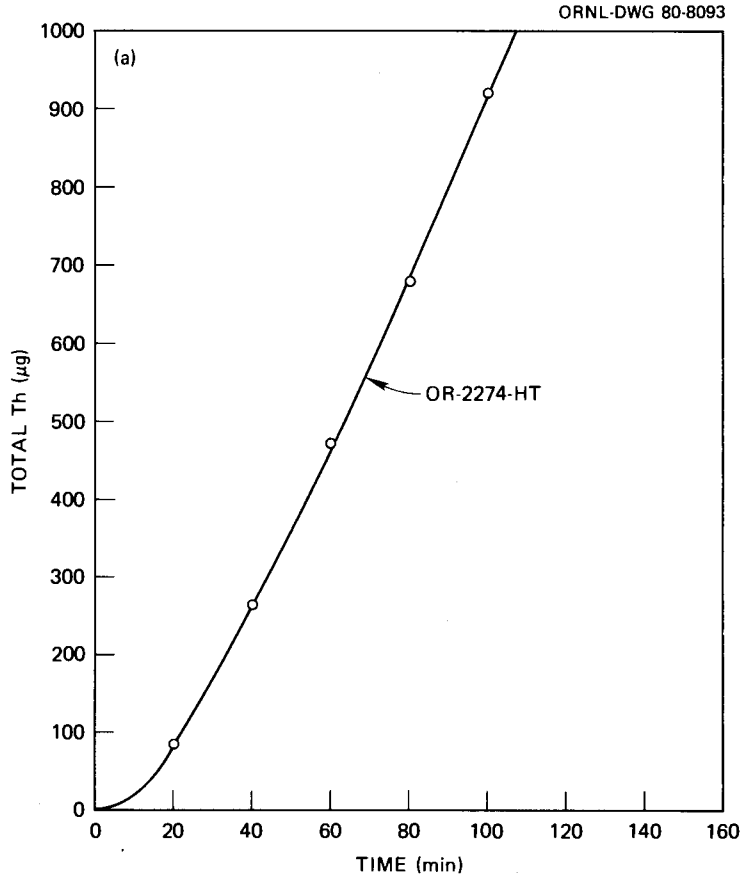

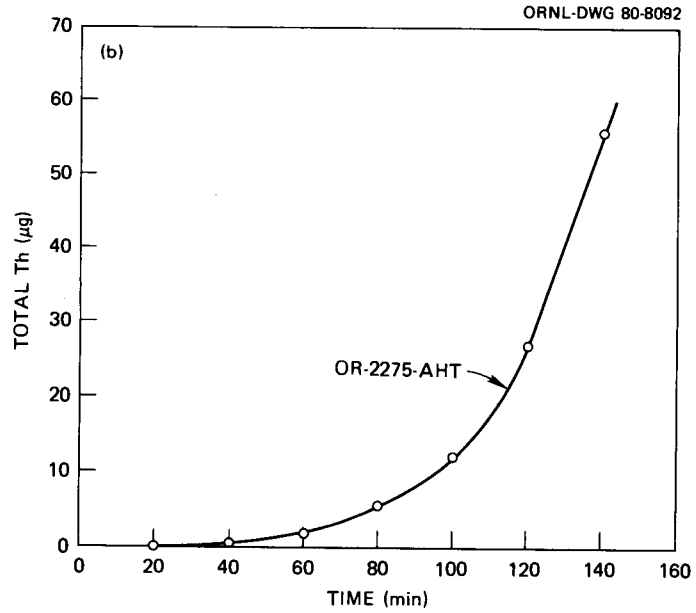

Fig. 4. Gaseous Leaching Rates for Samples of Particles from Batches (a) OR-2274-HT and (b) OR-2275-AHT Indicated That These LTI Coatings Were Permeable.

The relative volumes intruded into particle samples from a diluted fluidized bed were

Batch	Mercury Intrusion (mL/kg particle)
OR-2296-AHT	17.5
2290-HT	18.3
2298-HT	6.6
2297-AHT	13.1
2294-HT	7.1
2291-HT	12.7
2293-HT	9.8
2299-HT	7.9
2295-HT	5.9

The Fuel Test Techniques Branch of GA measured the intrusion with a conventional Aminco mercury porosimeter. Note that the intrusion measurements are reported in milliliters of mercury per kilogram of particle. Particles from batch OR-2274-HT yielded an intrusion value that indicated the mercury had completely penetrated the LTI into the buffer layer. Similar measurements were made at ORNL at pressures up to 103 MPa. These results are reported as percent surface connected porosity in Table 1.

Small-Angle X-Ray Scattering (SAXS)

As part of the U.S.-Federal Republic of Germany exchange program, the Institut für Reactorwerkstoffe (IRW) at KFA Jülich characterized the microstructure of the ORNL coatings from SAXS measurements. These results are compared with other preirradiation measurements and later in this report with irradiation performance.

Pores in the forms of voids, cracks, gaps, and misfitting layers ranging from about 1 to 100 nm can be detected by SAXS.[8] For scattering angles up to 3° from the beam axis, the scattered x-ray intensity depends on the number, size, and shape of the pores. As will be shown later, the significant feature of measuring the microporosity of pyrocarbon is the pore size distribution rather than the total porosity. Therefore, evaluation of the pore size distribution from the scattering curve was approached with a modified Guinier analysis method.[9]

The x-ray measurements were performed on fractured pieces of outer pyrocarbon coatings that had been separated from the buffer layer. The coatings from more than 50 particles are required for each SAXS

measurement. Although it is not possible to determine the pore size distribution of a single coating, more representative average values for a batch of particles are obtained by using at least 50 coatings.

A Kratky camera with a stepscanning device, a Cu $K\alpha$ radiation, and a proportional counter in connection with a discriminator and a teletype was used to measure and register the scattered x-ray intensity. Based on experience with detailed SAXS studies the evaluation procedure[9] was modified to provide a relatively simple routine characterization method. Instead of measuring the entire scattering curve, the scattered intensity was recorded at only seven positions. The angles chosen were such that the intensities were proportional to the concentration of pores with diameters of 1.0, 2.5, 5.0, 10, 25, 50, and 100 nm. These diameters corresponded to pores with the average volume of pore size intervals listed in Table 7. To eliminate the effects of x-ray beam geometry and camera alignment and to facilitate the comparison of different pyrocarbon coatings, the measured pore concentrations of the different pore size intervals were compared with a reference sample. The reference sample was arbitrarily assigned the value of 100% for each pore size interval. This allowed a relatively accurate comparison of different samples with a reproducibility of better than 1%. This simplified method required only 1 h for the measurement and evaluation of the relative pore size histogram. For quality control purposes only, the relative pore size distribution was significant. However, the absolute pore spectra could be calculated, if desired, since the absolute pore size distribution of the reference sample was known.

Pore size distribution

The relative pore size distributions from 0 to 20 nm for MAPP-gas-derived coatings are shown in the next four figures. Although the pore spectra of these coatings differ markedly from coatings derived from propene or methane, the pore size distributions of MAPP-gas-derived coatings are similar to coatings derived from acetylene-propene gas mixtures used at Hochtemperaturreaktor-Brenn-element-Gessellschaft (HOBEG), Hanau, Federal Republic of Germany, and KFA. The relative pore size distributions*

*The relative pore volume of each pore diameter is based on comparison with a reference sample that is arbitrarily assigned the value of 100% for each pore size.

Table 7. Upper and Lower Diameter Limits of the Different Pore Size Intervals Determined from Small-Angle X-Ray Scattering Measurements

Pore Diameter Limits, nm		Total Volume of Each Pore Size Interval (nm^3)	Average Pore Diameter[a] (nm)
Lower	Upper		
0.7	1.1	8.0×10^{-1}	1.0
1.1	3.0	1.4×10^{1}	2.5
3.0	6.0	1.0×10^{4}	5.0
6.0	12.1	8.1×10^{4}	10.0
12.1	30.8	1.4×10^{6}	25.0
30.8	60.5	1.0×10^{7}	50.0
60.5	121.1	8.1×10^{7}	100.0

[a]Pore diameters were calculated for the average pore volume for each pore size interval.

for coatings derived from MAPP gas at 1275°C as a function of coating rate are shown in Fig. 5. Note that as the coating rate increases, the number of pores smaller than 5 nm decreases and the number of larger pores increases. The pore spectra of coatings deposited at 1275°C in a diluted bed of thoria and inert-carbon kernels are shown in Fig. 6. Under these simulated fissile-particle-coating conditions the thoria kernels reached the desired-low-gas-flow conditions and maintained a stable fluidized bed. The increased surface area of a diluted bed at a given gas flow rate effectively lowered the gas flux and resulted in a lower deposition rate. Because of the lower deposition rate the concentration of the smaller pores is higher in the coatings from the diluted bed compared with that in the undiluted bed at the same deposition temperature. The variation in pore size distribution (i.e., decrease in number of smaller pores and increase in the number of larger pores with increasing deposition rate) is the same for both beds. Also, the number of pores with diameters ranging from 2.5 to 5.0 nm is higher in Fig. 6 than in Fig. 5, which appears to be an anomaly and may be indicative of a different fluidizing behavior of the two beds.

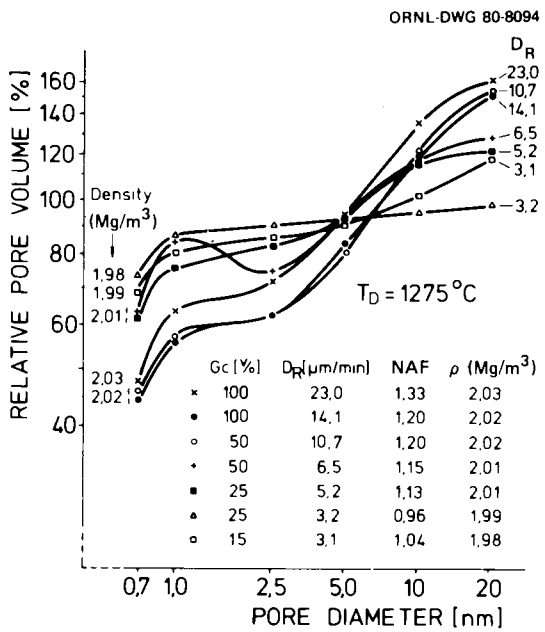

Fig. 5. Relative Pore Volumes in Coatings Derived from Various Concentrations of MAPP Gas in Normal Beds at 1275°C as a Function of Pore Diameter. D_R = deposition rate, T_D = deposition temperature, G_C = coating gas concentration, NAF = normalized amount of fiber component, and ρ = density.

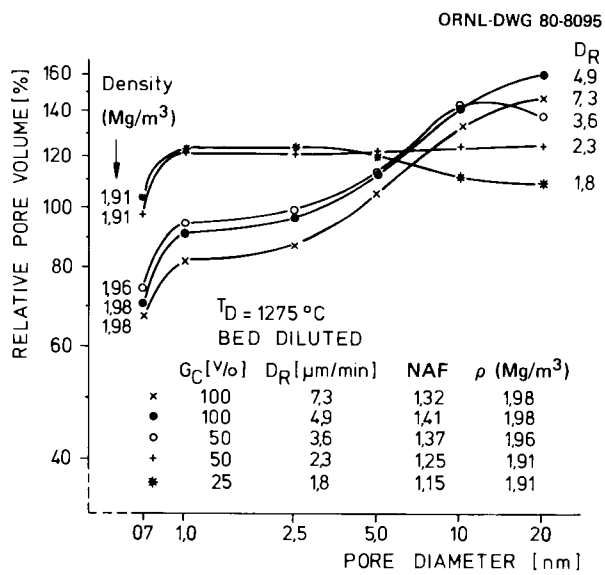

Fig. 6. Relative Pore Volumes in Coatings Derived from Various Concentrations of MAPP Gas in Diluted Beds at 1275°C as a Function of Pore Diameter. D_R = deposition rate, T_D = deposition tempeature, G_C = coating gas concentration, NAF = normalized amount of fiber component, and ρ = density.

The pore spectra of coatings deposited at 1325°C (Figs. 7 and 8) show similar variations with deposition rate as the coatings deposited at 1275°C, although the concentration of pores to 5 nm are much higher in the higher temperature coatings. As observed for the lower temperature coatings, the coatings deposited in a diluted fissile-type bed of particles contain more porosity than the coatings in an undiluted fertile-type bed.

Comparison of relative volume of pores smaller than 2.5 nm with immersion density

The porosity in pyrocarbons with immersion densities greater than 1.45 Mg/m^3 primarily results from pores less than 2.5 nm in diameter.[9] For a given deposition temperature the number of small pores decreases with increasing deposition rate, which leads to an increase in immersion density. The correlation of immersion density with deposition rate is shown in Fig. 9 for coatings deposited at 1275 and 1325°C. The variation in density is more apparent at lower deposition rates.[9] As expected, the immersion densities of coatings deposited at 1275°C are higher than those of coatings deposited at 1325°C. By comparison, coatings deposited in diluted beds of particles (Fig. 10) were not as consistent as those deposited in undiluted beds. This could be a reflection of a slight shift in the coating parameters that could result from the large difference in the density of the thoria kernels compared with the low-density inert carbon kernels.

The correlation of the relative volume of pores smaller than 2.5 nm in all the MAPP-gas-derived coatings used in this series of irradiation tests is shown in Fig. 11. This correlation confirms that the small pores are the major influence on immersion density variations in pyrocarbon coatings.

Comparison of medium-sized pores with LTI microstructure

The TEM and SAXS measurements revealed that the microstructural variations observed in LTI coatings could be described by two microstructural constitutents with very different pore size distributions. Coatings

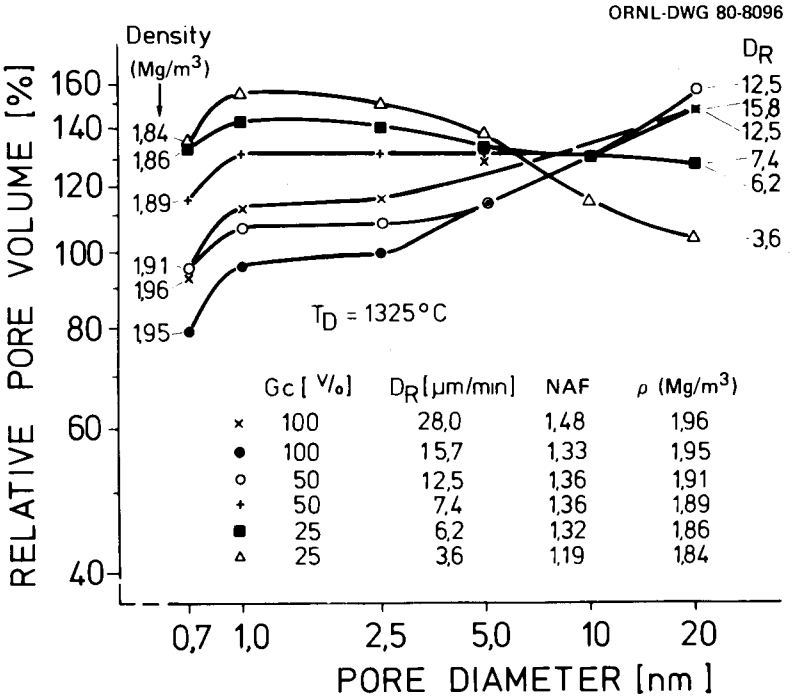

Fig. 7. Relative Pore Volumes in Coatings Derived from Various Concentrations of MAPP Gas in Normal Beds at 1325°C as a Function of Pore Diameter. D_R = deposition rate, T_D = deposition temperature, G_C = coating gas concentration, NAF = normalized amount of fiber component, and p = density.

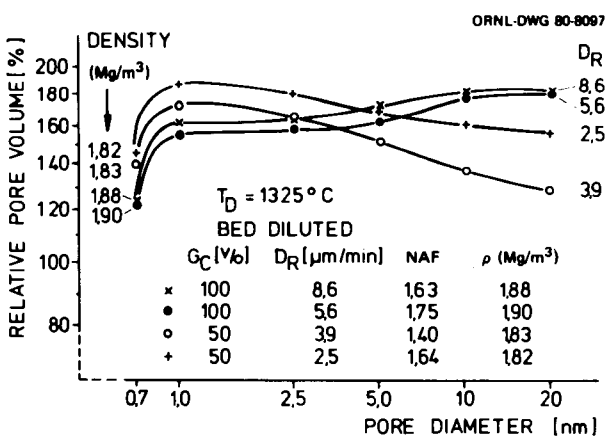

Fig. 8. Relative Pore Volumes in Coatings Derived from Various Concentrations of MAPP Gas in Diluted Beds at 1325°C as a Function of Pore Diameter. D_R = deposition rate, T_D = deposition temperature, G_C = coating gas concentration, NAF = normalized amount of fiber component, and ρ = density.

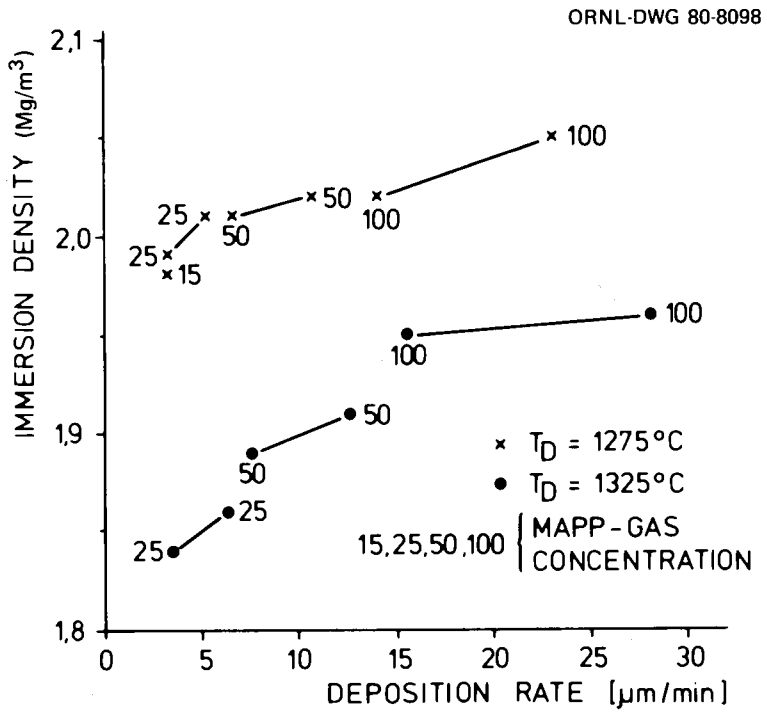

Fig. 9. Immersion Densities of Coatings Derived from Various Concentrations of MAPP Gas in Normal Beds at 1275 and 1325°C as a Function of Deposition Rate. T_D = deposition temperature.

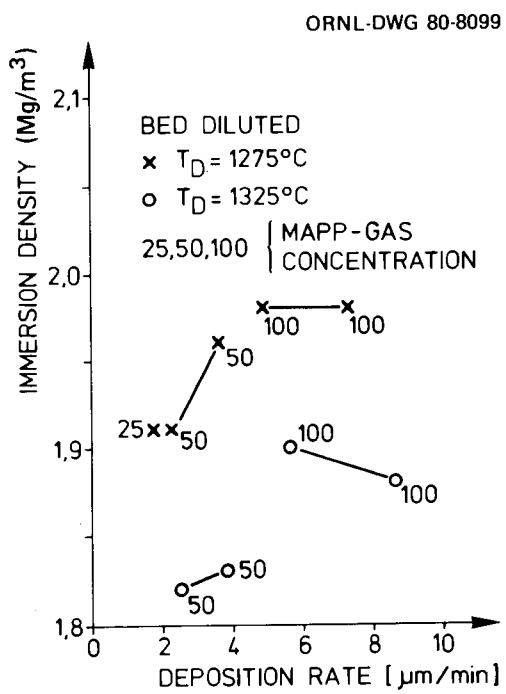

Fig. 10. Immersion Densities of Coatings Derived from Various Concentrations of MAPP Gas in Diluted Beds at 1275 and 1325°C as a Function of Deposition Rate. T_D = deposition temperature.

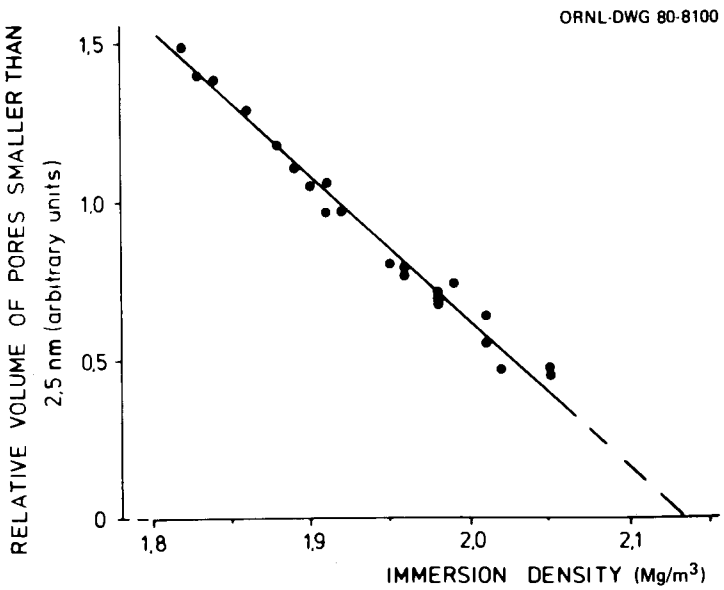

Fig. 11. Relative Volume of Pores with Diameters Smaller than 2.5 nm in MAPP-Gas-Derived Coatings as a Function of Immersion Density.

deposited in the temperature range between 1250 and 1400°C (LTI) may consist of a "mosaic" component and a "fiber" component or of an intermediate microstructural state.[6] The crystallites in the mosaic component derived at about 1250°C are closely packed and well aligned in regions that extend up to 1 μm. The fiber component deposited at 1400°C consists of an interwoven network of tangled fibers containing a varying amount of fine porosity.[10]

Comparison of TEM micrographs and pore size distributions showed that the ratio of the mosaic component and the fiber material or an intermediate state in the microstructure of the components can be correlated with the relative concentration of pores ranging from 6 to 25 nm in diameter. Therefore, a parametric property, the normalized amount of fiber component (NAF),* is derived from this pore concentration.

In Fig 12 the NAF of MAPP-gas-derived coatings is shown as a function of deposition rate. At both deposition temperatures the NAF is increasing with deposition rate. The coatings deposited at 1325°C had distinctly

---

* The NAF is calculated according to the formula NAF = $(2C_{10} + C_{20})/3$, where C_{10} and C_{20} are the relative pore concentrations of the pore size intervals ranging from 6 to 12 nm and from 12.1 to 25 nm, respectively. In Figs. 5 through 8 the NAF was calculated according to the formula NAF = $(C_5 = 2C_{10} = C_{20})/4$, which was used in the past where C_5 is the relative concentration of the pore size interval from 3 to 6 nm.

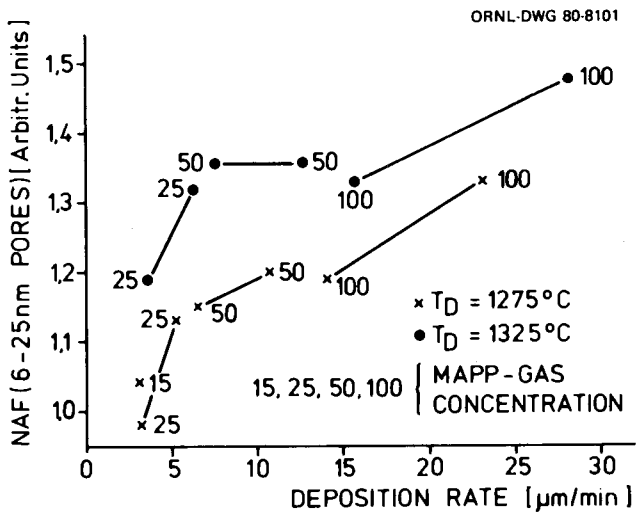

Fig. 12. The Normalized Amount of Fiber Component (NAF) Values for Coatings Derived from Various Concentrations of MAPP Gas in Normal Beds at 1275 and 1325°C as a Function of Deposition Rate. T_D = deposition temperature.

Table 8. Results from Neon-to-Helium, NAF, and ROC Determinations on Particles Used in Capsules HT-28, -29, and -30

Batch	Deposition		Ne/He	NAF[a]	ROC[b]
	Temperature (°C)	Coating Rate (μm/min)			
	Undiluted-Fluidized-Bed Particles				
OR-2275-AHT	1275	23.0	0.41	1.46	1
OR-2266-HT	1275	14.1	c	1.31	2
OR-2271-HT	1275	10.7	0.23	1.34	1
OR-2262-HT	1275	6.5	0.20	1.22	3
OR-2273-HT	1275	5.2	0.14	1.19	2
OR-2264-HT	1275	3.2	c	0.97	3
OR-2276-HT	1275	3.1	0.13	1.09	
OR-2274-HT	1325	28.0	0.50	1.54	1
OR-2265-HT	1325	15.7	0.32	1.39	2
OR-2269-HT	1325	12.5	0.40	1.42	2
OR-2261-HT	1325	7.4	0.23	1.30	3
OR-2272-HT	1325	6.2	c	1.31	2
OR-2263-HT	1325	3.6	0.13	1.12	1
	Diluted-Fluidized-Bed Particles				
OR-2291-HT	1275	7.6	0.27	1.40	3
OR-2297-AHT	1275	4.9	0.27	1.50	4
OR-2294-HT	1275	3.6	0.15	1.44	3
OR-2299-HT	1275	2.3	0.19	1.26	2
OR-2295-HT	1275	1.8	c	1.12	1
OR-2290-HT	1325	8.6	c	1.65	3
OR-2296-HT	1325	5.6	0.44	1.78	3
OR-2293-HT	1325	3.9	0.23	1.36	3
OR-2298-HT	1325	2.5	0.24	1.62	1

[a]Normalized amount of fiber component.

[b]Relative amount of readily oxidized carbon listed for groups in order of decreasing amounts, that is, 1 is greatest amount and 4 is least amount.

[c]Not available.

higher NAF values. This is in agreement with the observed increase of NAF of propene-derived coatings with increasing deposition temperatures from 1250 to 1400°C. The NAF values for the MAPP-gas-derived coatings used in irradiation test capsules HT-28, -29, and -30 are given in Table 8. The mean values for coatings deposited at 1275 and 1325°C decrease with a decrease in gas flux, that is, gas flow and concentration. Despite the lower hydrocarbon flux (deposition rate), the coating deposition on the thoria kernels in the diluted beds consistently yielded higher NAF values than the coatings deposited in the undiluted beds. This indicates again a different fluidizing behavior of the diluted and undiluted or fissile- and fertile-type beds in the coating furnace.

Comparison of NAF with plasma oxidation results

The different oxidation rates of the mosaic component and the fiber material in a radio-frequency-excited oxygen plasma was used as an additional method to characterize pyrocarbon coatings.[11] The plasma oxidation technique allowed an estimation of the volume ratio of the two components in LTI coatings. As the porous low-density fiber component contained a large unprotected surface area parallel to the *C*-axis, the oxidation rate of the fiber material is high compared to the highly ordered, dense mosaic component. Investigations by TEM proved that the fiber component was readily oxidizable carbon (ROC) as defined by plasma oxidation. Since NAF is related to the fiber component, a relation was found between NAF and ROC.

The estimated amounts of ROC in the plasma-oxidized ceramographic sections of the MAPP-gas-derived coatings are listed in Table 8. The listing of the groups of coatings was arranged so that each group had the same gas concentration and deposition temperature. The amount of ROC is generally higher in the coatings deposited at 1325°C compared with the lower deposition temperature. In addition, a decrease in ROC was associated with a decrease in gas concentration. Both these effects agree with the NAF values for these coatings. Although the plasma oxidation values are only estimates and therefore can vary slightly, the variations observed between ROC and NAF seem to be real. Variations of ROC values can result from the appearance of the sections, the distribution of ROC within the coating, and the subjectivity of the estimation.

However, when comparing the ROC values listed in Table 8 the particles from the diluted beds at a given set of deposition conditions are different from the normal-bed particles.

Comparison of NAF with neon permeability of unirradiated coatings

Since higher NAF values indicate an increasing amount of fibers containing high concentrations of interconnected porosity, the gaseous permeability of coatings is expected to increase with increasing NAF. Neon permeability of the unirradiated particles was measured in an effort to obtain information about the permeability of pyrocarbon to the gaseous fission products xenon and krypton during irradiation.[8] The permeability of a coating is measured by determining the neon-helium gas mixture in a particle after being subjected to a 1:1 neon-to-helium ratio atmosphere at 10^5 Pa and 1648 K.

The neon-to-helium ratios for the majority of the coatings used in these irradiation tests are listed in Table 8. The correlation of the neon-to-helium ratios with the NAF values is shown in Fig. 13. The permeability to neon increases with increasing NAF, that is, with the amount of tangled fiber component. At NAF values below 1.2 the neon permeability is nearly constant, probably governed by diffusion. At higher NAF values the permeability increases remarkably with the increase in concentration of interconnected porosity in the fiber component. As the permeability is related to the NAF, the preirradiation gas permeability of LTI coatings increases with increasing temperature and increasing deposition rate. It can be seen in Fig. 13 that the coatings deposited at 1275°C and at low deposition rates have low neon-to-helium ratios in contrast with coatings derived with high deposition rates at 1325°C. Note also that the majority of NAF values for the coatings deposited in the mixed beds of thoria and inert carbon kernels do not fit the neon-helium correlation. This is another indication that the microstructures of coatings deposited in a diluted fissile-type bed are different from those deposited in an undiluted fertile-type bed.

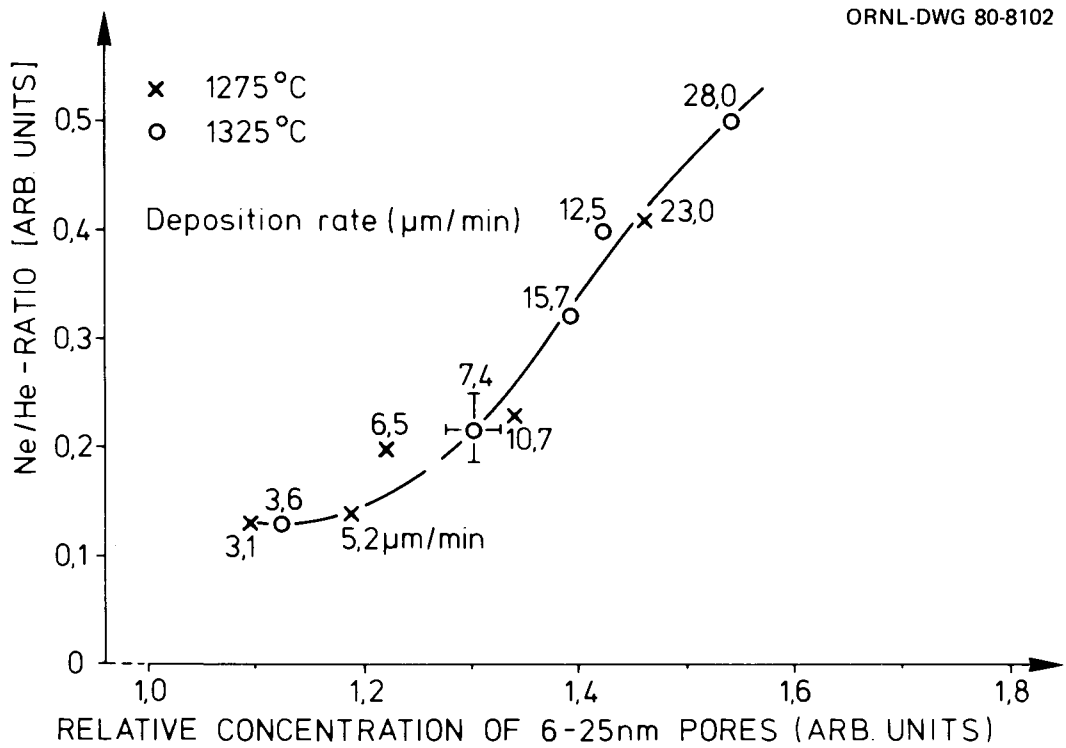

Fig. 13. Neon-Helium Permeability Values for Coatings Derived from MAPP Gas at 1275 and 1325°C as a Function of Normalized Amount of Fiber Component (NAF).

Comparison of NAF with static-pressure mercury intrusion measurements

Generally, the intruded mercury volume increased as the deposition temperature and rate increased. The intruded mercury is shown as a function of deposition rate in Fig. 14. Again, a difference in material properties is indicated between particles prepared in a normal vs diluted bed. As shown in Fig. 14, for a given deposition rate the particles prepared in a diluted bed have the more permeable coatings, reflecting the effect of a higher concentration of hydrocarbon. At a relative volume of intruded mercury of about 20, the mercury penetrated the LTI layer and filled the void volume of the buffer, which corresponded to a neon-to-helium ratio of about 0.4 to 0.5 (Fig. 15) for these coatings.

The mercury intrusion values as a function of NAF are shown in Fig. 16. Again, a difference between the coatings prepared in the normal vs diluted beds is evident. At NAF values between about 1.4 and 1.5

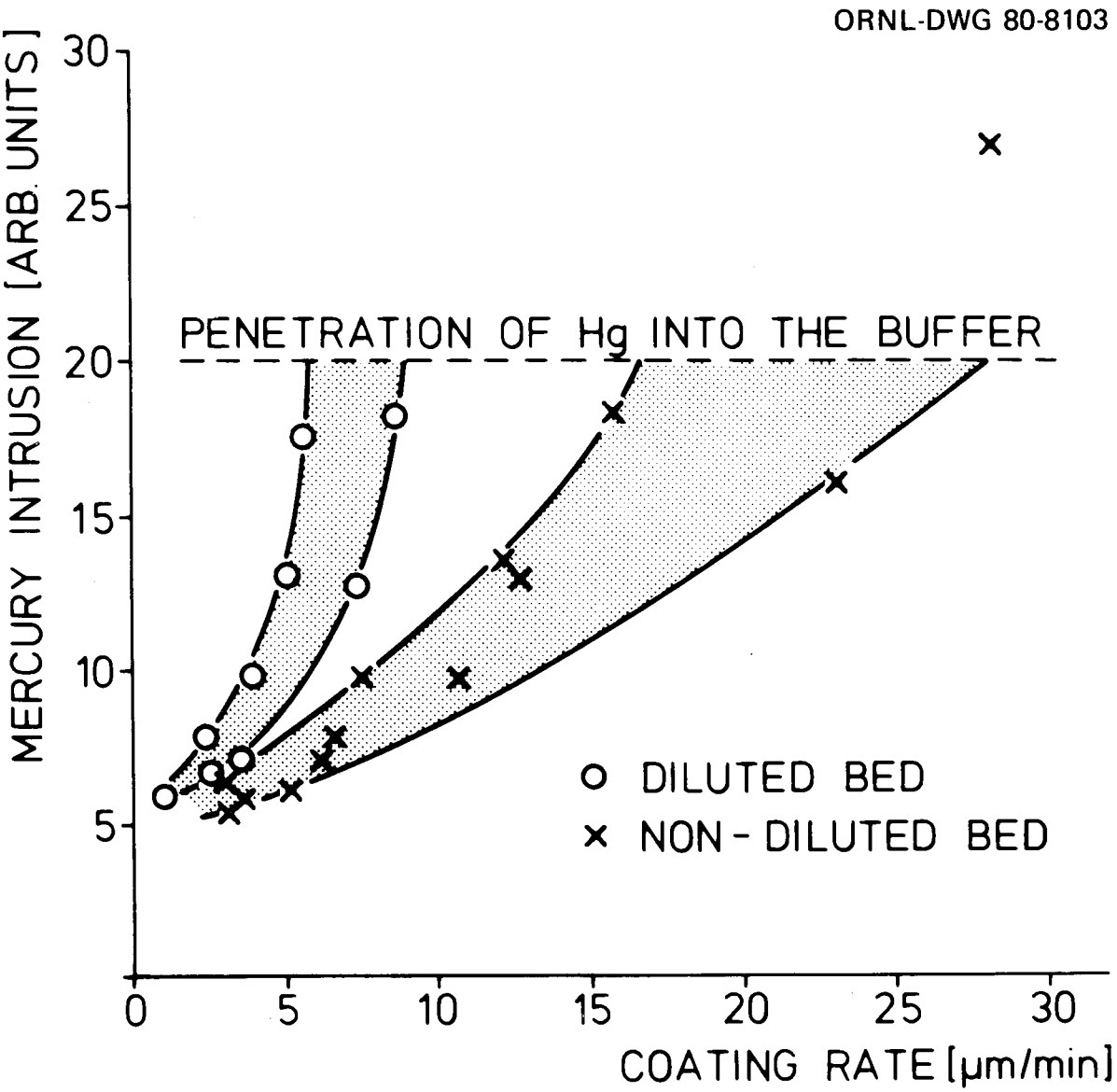

Fig. 14. Mercury Intrusion Values for Coatings Derived from MAPP Gas in Diluted and Nondiluted Beds as a Function of Coating Rate.

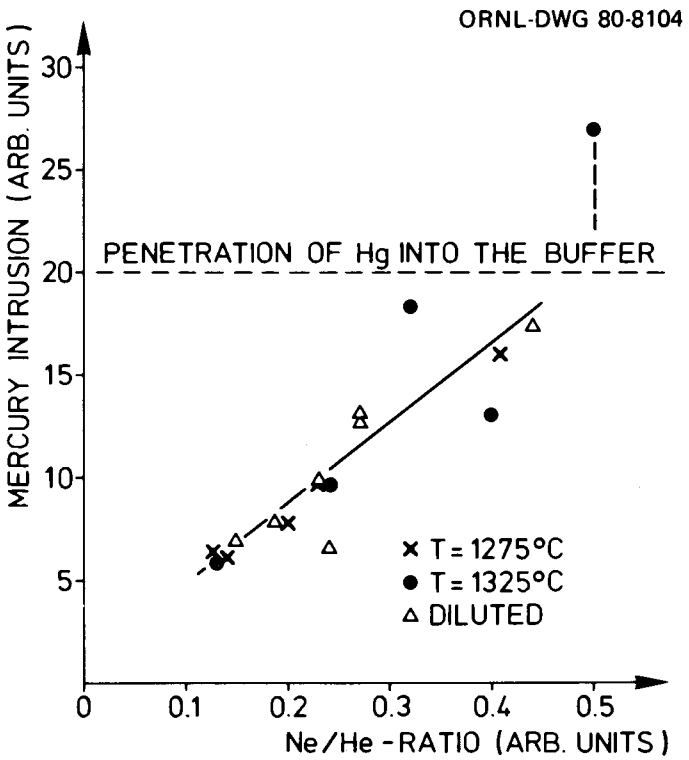

Fig. 15. Mercury Intrusion Values for Coatings Derived from MAPP Gas at 1275 and 1325°C as a Function of Neon-Helium Permeability Measurements.

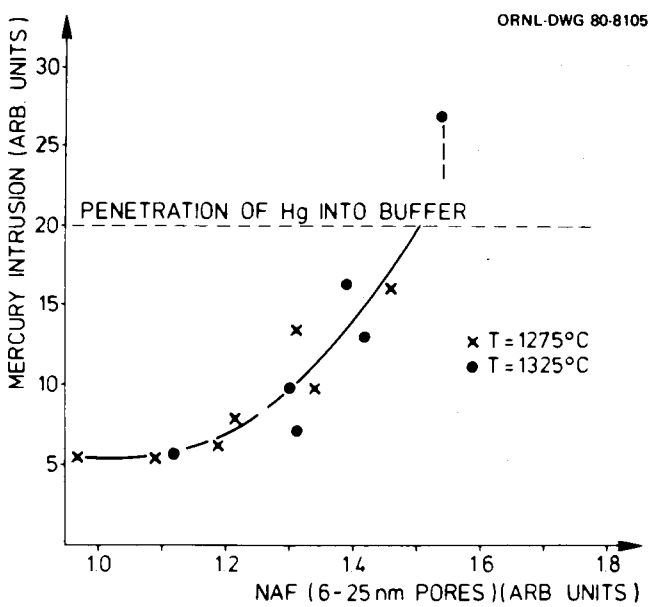

Fig. 16. Mercury Intrusion Values for Coatings Derived from MAPP Gas at 1275 and 1325°C as a Function of Normalized Amount of Fiber Component (NAF).

the mercury filled the void volume of the buffer. The relationship between mercury intrusion and NAF values (Fig. 16) is nonlinear, as was the relationship between the neon-to-helium ratio and NAF values (Fig. 13). As indicated in Figs. 13 and 16, the permeability markedly increased as the NAF values increased, which reflects the increase in the number of large interconnected pores. The relationship between the "mercury permeability" and "neon permeability" appears to be linear (Fig. 15). The reasons for the linear and nonlinear correlations are that when NAF values are compared with permeability measurements, microstructural differences and physical measurements are also compared, whereas with the two permeability measurements, two physical measurements for essentially the same property are compared.

Comparison of NAF with hot gaseous chlorine leach analysis

Leaching Biso-coated particles with hot gaseous chlorine can be used to identify failed or permeable coatings before and after irradiation. A listing of NAF values, neon-to-helium ratios, mercury intrusion, and chlorine leach results is given in Table 9 for the particles used in capsules HT-28 through -30. The particles listed in Table 9 were separated into two groups: coatings that were deposited in diluted beds and those that were deposited in nondiluted beds. The batches of particles in each of the two groups are listed in decreasing order of probability of permeability according to the NAF values. The coatings from batches OR-2274-HT and -2275-HT were leachable before irradiation. Although these two batches were deposited at both high and low temperatures, both batches were produced at deposition rates of 23 and 28 μm/min. The deposition conditions produced microstructures that contained large amounts of the porous fiber component, which resulted in the highest NAF values (1.46 and 1.54) of the "nondiluted" particles. In agreement with high NAF values, these coatings showed high permeability to neon (Fig. 13). Also, the mercury intrusion measurement of coatings from OR-2274-HT yielded the highest value of all coatings listed in Table 9.

Table 9. Summary of NAF, Neon-Helium, Mercury Intrusion, and Chlorine Leach Measurements Compared with Deposition Rates for Particles Used in HT-28, -29, and -30

Batch	Coating Rate (μm/min)	NAF[a]	Ne/He	Mercury Intrusion (mL/kg particle)	Chlorine Leach[b]		BAF_o[c] (ORNL Mounts)
					GA	ORNL	
			Undiluted-Fluidized-Bed Particles				
OR-2274-HT	28.0	1.54	0.50	27.1	L	L	1.033
OR-2275-AHT	23.0	1.46	0.41	16.0	L	L	1.037
OR-2269-HT	12.5	1.42	0.40	13.0			1.032
OR-2265-HT	15.7	1.39	0.32	18.3			1.033
OR-2271-HT	10.7	1.34	0.23	9.7			
OR-2266-HT	14.1	1.31	*d*	13.6			1.037
OR-2272-HT	6.2	1.31	*d*	7.0			1.027
OR-2261-HT	7.4	1.30	0.23–0.25	9.7			1.024
OR-2262-HT	6.5	1.22	0.20	7.8			1.026
OR-2273-HT	5.2	1.19	0.14	6.1			1.038
OR-2263-HT	3.6	1.12		5.8			1.027
OR-2276-HT	3.1	1.09	0.13	6.4			1.048
OR-2264-HT	3.2	0.97	*d*	5.4			1.028
			Diluted-Fluidized-Bed Particles				
OR-2296-AHT	5.6	1.78	0.44	17.5			1.037
OR-2290-HT	8.6	1.65	*d*	18.3			1.027
OR-2298-HT	2.5	1.62	0.24	6.6			1.030
OR-2297-HT	4.9	1.50	0.27	13.1			1.032
OR-2294-HT	3.6	1.44	0.15	7.1			1.045
OR-2291-HT	7.3	1.40	0.27	12.7			1.033
OR-2293-HT	3.9	1.36	0.23	9.8			
OR-2299-HT	2.3	1.26	0.19	7.9			1.028
OR-2295-HT	1.8	1.19	*d*	5.9			1.048

[a]Normalized amount of fiber component.

[b]GA = General Atomic Company; ORNL = Oak Ridge National Laboratory; L = leachable.

[c]BAF_o = Bacon Anisotropy Factor determined optically.

[d]Not available.

CAPSULE LOADING, OPERATION, FLUENCE, AND BURNUP

The fuel loadings for all three capsules are shown in Table 10. Capsules HT-28 and -30 were irradiated for four HFIR cycles from February 4 to May 9, 1975. Capsule HT-29 received five cycles of irradiation from February 4 to June 3, 1975. The loading sequence and irradiation conditions for HT-28, -29, and -30 are shown, respectively, in Tables 11 through 13. Irradiation histories for all capsules are given in Tables 14 and 15.

All three capsules were successfully irradiated and transferred to the hot cells for examination.

Table 10. Fuel Loadings for Capsules HT-28, -29, and -30

Capsule	Thorium Loading per Specimen, g	
	Low-Temperature Magazines	High-Temperature Magazines
HT-28	0.0234	0.0331
HT-29	0.0600	0.0351
HT-30	0.0249	0.0339

THERMAL ANALYSIS

Target capsules HT-28, -29, and -30 contained no provisions for real-time temperature monitoring or for a sweep-gas system for temperature control. Thus design and operating temperatures were determined by thermal modeling computer codes. Design conditions for capsules HT-28 and -30 were for two

Table 11. Capsule HT-28 Loading Scheme, Design Operating Temperature, Neutron Fluences, and Heavy Metal Burnup

Capsule Position[a]	Specimen Lot[b]	Design Temperature[c] (°C)	Estimated Fluence, neutrons/m^2 <0.414 eV (<0.0663 aJ)	Estimated Fluence, neutrons/m^2 >0.18 MeV (>29 fJ)	Estimated ^{232}Th Burnup (% FIMA[d])
E-S-1	LASL[e]	900			
1-A	LASL[f]				
2, 4, 5, 7	GA[g]	900			
8	OR-2294-HT	900	14.3×10^{25}	6.07×10^{25}	6.30
10	OR-2266-HT	900	14.9	6.54	6.70
11, 13	GA[g]	900			
M-S-1	LASL[e]	1250			
15, 17, 18, 20	GA[g]	1250			
21	OR-2294-HT	1250	20.4	8.77	8.69
23	OR-2266-HT	1250	20.9	8.88	8.80
24, 26	GA[g]	1250			
27	GA[g]	1250			
29	OR-2273-HT	1250	21.1	8.92	8.85
30	OR-2297-HT	1250	20.9	8.88	8.80
32	OR-2262-HT	1250	20.4	8.77	8.69
33, 35, 36, 38	GA[g]	1250			
M-S-2	LASL[e]	1250			
40	GA[g]	900			
42	OR-2273-HT	900	15.4	6.77	6.90
43	OR-2297-HT	900	14.9	6.54	6.70
45	OR-2262-HT	900	14.3	6.07	6.30
46, 48, 49, 51	GA[g]	900			
E-S-2	LASL[e]	900			

[a]Positions (1 through 52) not listed contained uranium (6.5% enriched in ^{235}U) for heat generation only.

[b]LASL = Los Alamos Scientific Laboratory; GA = General Atomic Company.

[c]Graphite holder surface temperature.

[d]Fissions per initial metal atom.

[e]LASL loose inert particles in graphite end plug.

[f]LASL hot-pressed ZrC wafer placed in end (replacing graphite screw) of uranium-loaded particle holder.

[g]GA Biso-coated fertile particles.

Table 12. Capsule HT-29 Loading Scheme, Neutron Fluences, and Heavy Metal Burnup[a]

Capsule Position[b]	Specimen Lot[c]	Estimated Fluence, neutrons/m^2 <0.414 eV (<0.0663 aJ)	Estimated Fluence, neutrons/m^2 >0.18 MeV (>29 fJ)	Estimated ^{232}Th Burnup (% FIMA[d])
E-S-1	LASL[e]			
1-A	LASL[f]			
2	OR-2264-HT	14.4×10^{25}	5.73×10^{25}	7.15
4	OR-2294-HT	15.6	6.40	7.85
5, 7, 8, 9, 10, 11, 13	GA[g]			
E-L-1	LASL[c]			
M-S-1	LASL[e]			
14-A	LASL[f]			
15	OR-2291-HT	23.2	10.21	11.40
17, 18, 20, 21	GA[g]			
23	OR-2262-HT	26.2	11.12	12.20
24, 26	GA[g]			
M-L-1	LASL[e]			
M-L-2	LASL[e]			
27	GA[g]			
29	OR-2299-HT	26.5	11.17	12.30
30	OR-2261-HT	26.2	11.12	12.20
32, 33, 35, 36	GA[g]			
38	OR-2290-HT	23.2	10.21	11.40
39-A	LASL[d]			
M-S-2	LASL[e]			
E-L-2	LASL[e]			
40, 42, 43, 45, 46	GA[g]			
48	OR-2298-HT	16.2	6.69	8.20
49	OR-2293-HT	15.6	6.40	7.85
51	OR-2263-HT	14.4	5.73	7.15
52-A	LASL[f]			
E-S-2	LASL[e]			

[a]Graphite holder design surface temperature was 900°C.

[b]Positions (1 through 52) not listed contained uranium (6.5% enriched in ^{235}U) in warm-molded rods for heat generation only.

[c]LASL = Los Alamos Scientific Laboratory; GA = General Atomic Company.

[d]Fissions per initial metal atom.

[e]LASL loose inert particles in graphite end plug.

[f]LASL extruded graphite wafer accommodated for shortening adjacent uranium-loaded rod.

[g]GA Biso fertile particles.

Table 13. Capsule HT-30 Loading Scheme, Design Operating Temperature, Neutron Fluences, and Heavy Metal Burnup

Capsule Position[a]	Specimen Lot		Estimated Fluence, n/m^2		Estimated ^{232}Th Burnup (% FIMA[b])
	First Position	Second Position	<0.414 eV (<0.0663 aJ)	>0.18 MeV (>29 fJ)	
E-S-1,-2	Inerts[c]	Inerts[c]		3.8×10^{25}	
1, 52	OR-2276-HT	OR-2295-HT	11.1×10^{25}	4.31	4.61
2, 51	OR-2298-HT	OR-2263-HT	11.5	4.58	4.90
3, 50	J-488[d]	J-490[d]	12.0	4.92	5.12
4, 49	OR-2299-HT	OR-2264-HT	12.5	5.11	5.40
5, 48	OR-2290-HT	OR-2269-HT	12.9	5.34	5.62
6, 47	OR-2291-HT	OR-2271-HT	13.4	5.61	5.85
7, 46	OR-2293-HT	OR-2262-HT	13.8	5.84	6.10
8, 45	OR-2294-HT	OR-2262-HT	14.3	6.07	6.30
9, 44	OR-2265-HT	OR-2296-AHT	14.6	6.31	6.50
10, 43	OR-2266-HT	OR-2297-AHT	14.9	6.54	6.70
11, 42	OR-2274-HT	OR-2273-HT	15.4	6.77	6.90
12, 41	OR-2275-AHT	OR-2272-HT	15.8	6.99	7.10
13, 40	J-489[d]	J-491	16.1	7.15	7.21
E-L-I,-2	Inerts[c]	Inerts[c]		7.4	
M-S-1,-2	Inerts[c]	Inerts[c]		7.7	
14, 39	J-489[d]	J-491[d]	18.1	8.00	8.09
15, 38	OR-2276-HT	OR-1849-HT[e]	18.5	8.15	8.21
16, 37	OR-2298-HT	OR-2263-HT	18.9	8.27	8.30
17, 36	OR-2299-HT	OR-2264-HT	19.2	8.42	8.40
18, 35	OR-2290-HT	OR-2269-HT	19.6	8.52	8.49
19, 34	OR-2291-HT	OR-2271-HT	19.8	8.61	8.59
20, 33	OR-2293-HT	OR-2261-HT	20.1	8.69	8.62
21, 32	OR-2294-HT	OR-2262-HT	20.4	8.77	8.69
22, 31	OR-2265-HT	OR-2296-AHT	20.6	8.84	8.75
23, 30	OR-2266-HT	OR-2297-AHT	20.9	8.88	8.80
24, 29	OR-2274-HT	OR-2273-HT	21.1	8.92	8.85
25, 28	OR-2275-AHT	OR-2272-HT	21.3	8.96	8.88
26, 27	J-488[d]	J-490[d]	21.5	9.00	8.91
M-L-1,-2	Inerts[c]	Inerts[d]		9.0	

[a]Specimens 1–13 and 40–52 had 900°C design surface temperature; specimens 14–39 had 1250°C design surface temperature.

[b]Fissions per inital metal atom.

[c]Magazine end plugs in the upper portion of the capsule contained inert batches OR-2291-HT and OR-2323-AH. Magazine end plugs in the lower portion of the capsule contained inert batches OR-2290-HT, OR-2293-HT, OR-2294-HT, OR-2295-HT, OR-2296-AHT, OR-2297-AHT, OR-2298-HT, and OR-2299-HT.

[d]Biso-coated particles prepared in 0.13-m (5-in.) coater.

[e]Reference batch irradiated in HT-12 through -15.

4 cycles ∴ ~ 2.25×10^{25} n/m² cycle

2.25×10^{21} n/m²/cycle

Table 14. Reactor Power and Irradiation History[a] for HT-28 and -30

Cycle	Begin		End		Irradiation Time, h	
	Time	Date	Time	Date	During Cycle	Accumulated
117	1700	2/4/75	1800	2/26/75	527.76	527.76
118A	1732	2/28/75	1726	3/6/75	143.28	671.04
119	1524	3/7/75	0233	3/30/77	539.04	1210.08
118B	1821	3/30/75	0639	4/16/75	396.00	1606.08
120	0153	4/17/75	0400	5/9/75	529.92	2136.00

[a]HT-28 and -30 were irradiated in target positions A-3 and F-7, respectively.

Table 15. Reactor Power and Irradiation History[a] for HT-29

Cycle	Begin		End		Irradiation Time, h	
	Time	Date	Time	Date	During Cycle	Accumulated
117	1700	2/4/75	1800	2/26/75	527.76	527.76
118A	1732	2/28/75	1726	3/6/75	143.28	671.04
119	1524	3/7/75	0233	3/30/75	539.04	1210.08
118B	1821	3/30/75	0639	4/16/75	396.00	1606.08
120	0153	4/17/75	0400	5/9/75	529.92	2136.00
121	2125	5/11/75	0918	6/3/75	539.28	2675.28

[a]HT-29 was irradiated in target position E-2.

temperature regions, 900 and 1250°C. Capsule HT-28 contained loose fertile particles in specially designed holders. Low-enriched uranium (7% ^{235}U) particles were interspersed along the length of the capsule for initial heat generation. The static backfill gas was argon. The HT-30 capsule contained fertile particles in bonded fuel rods only. Thorium alone constituted the initial fuel makeup. The static backfill gas for HT-30 was neon.

Capsule HT-29 was designed for particle surface operating temperatures of 900°C. This capsule was isothermally designed and contained loose fertile test particles in specially designed holders. Driver fuel rods were fabricated by using low-enriched uranium (7% ^{235}U), and in some cases thorium was included to maintain desired 900°C temperatures throughout capsule life. The static backfill gas of HT-29 was helium (higher thermal conductivity than neon or argon) to increase heat transfer to capsule surface.

Operating temperature histories were obtained by using a modified version of the thermal modeling code HTCAP.[12] This code calculates maximum particle surface operating temperatures at specific time intervals for the life of the irradiation experiment. Modifications were necessary to account for the life of the different types of fuel specimens — loose particles vs fuel rods — and for some heater rods containing both fissile and fertile fuels. Temperature calculations were then based upon the physical and thermal properties of capsule components as functions of temperature and fast-neutron fluence, time-dependent fission-heat generation rates, axial-position-dependent gamma heating rates, and coolant temperature at the aluminum containment surface. The calculational procedure is described in detail in ref. 12.

Tables 16 and 17 describe the range in particle surface operating temperatures for the loose fertile particles irradiated in capsules HT-28 and -29, respectively, for each irradiation cycle. Table 18 describes the range in centerline temperature for each fuel rod in capsule HT-30 during each irradiation cycle. The Appendix contains detailed time-temperature histories and fission-heat generation histories for all specimens (both GA and ORNL) irradiated in capsules HT-28, -29, and -30.

Table 16. Maximum Particle Surface Temperatures for Capsule HT-28

Position	ORNL[a] Particle Batch	Particle Diameter (μm)	Temperature Range for HFIR[b] Cycles, °C				
			117	118A	119	118B	120
8	OR-2294-HT	871	945–1019	1059–1066	1090–1153	1177–1204	1220–1231
10	2266-HT	878	947–1029	1072–1084	1108–1174	1195–1217	1236–1249
21	2294-HT	871	1230–1323	1373–1378	1406–1460	1486–1505	1519–1527
23	2266-HT	878	1233–1325	1378–1385	1410–1468	1490–1510	1524–1530
29	2273-HT	852	1243–1333	1387–1396	1421–1479	1504–1524	1535–1546
30	2297-HT	878	1234–1328	1380–1385	1410–1468	1491–1508	1524–1530
32	2262-HT	873	1232–1318	1373–1378	1406–1461	1489–1505	1519–1525
42	2273-HT	852	958–1043	1091–1103	1125–1193	1217–1243	1260–1270
43	2297-HT	878	950–1032	1075–1087	1111–1174	1196–1222	1238–1252
45	2262-HT	873	947–1019	1061–1066	1093–1156	1178–1204	1218–1231

[a]Oak Ridge National Laboratory.

[b]High Flux Isotope Reactor.

Table 17. Maximum Particle Surface Temperatures for Capsule HT-29

Position	ORNL[a] Particle Batch	Particle Diameter (μm)	Temperature Range for HFIR[b] Cycles, °C					
			117	118A	119	118B	120	121
2	OR-2264-HT	883	829–968	833–849	830–843	852–863	872–883	889–898
4	2294-HT	871	702–754	747–751	768–808	830–850	865–879	889–895
15	2291-HT	872	806–907	835–845	848–875	890–903	909–918	919–934
23	2262-HT	873	734–787	831–832	853–898	918–935	949–955	960–970
29	2299-HT	880	734–788	831–833	851–898	919–933	947–953	961–971
30	2261-HT	875	731–787	831–832	853–898	919–935	949–955	960–970
38	2290-HT	886	809–907	835–848	848–876	890–898	909–918	917–929
48	2298-HT	864	709–771	752–755	772–813	840–863	875–885	899–905
49	2293-HT	879	702–754	750–753	768–806	830–853	865–877	892–895
51	2263-HT	873	834–975	839–855	838–849	863–869	883–889	895–902

[a]Oak Ridge National Laboratory.

[b]High Flux Isotope Reactor.

Table 18. Centerline Temperatures for Fuel Rods Irradiated in Capsule HT-30

Fuel Rod Position	ORNL[a] Particle Batch	Particle Diameter (μm)	Temperature Range for HFIR[b] Cycles, °C				
			117	118A	119	118B	120
1	OR-2276-HT	864	680–728	746–757	765–809	817–839	847–859
2	OR-2298-HT	865	687–758	782–793	810–866	880–908	916–934
3	J-488	829	686–758	782–796	810–864	881–906	917–934
4	OR-2299-HT	880	693–768	793–807	824–880	895–920	931–949
5	OR-2290-HT	886	693–774	801–812	829–884	901–927	938–952
6	OR-2291-HT	872	693–773	798–815	829–886	904–929	941–955
7	OR-2293-HT	879	700–789	815–832	846–904	922–947	961–976
8	OR-2294-HT	871	693–780	806–820	838–896	911–936	951–965
9	OR-2265-HT	889	681–769	795–812	827–883	901–927	938–950
10	OR-2266-HT	878	691–786	815–832	847–906	924–949	964–973
11	OR-2274-HT	888	692–788	817–835	853–912	930–953	968–979
12	OR-2275-HT	868	685–785	818–829	848–907	925–951	966–975
13	J-489	800	684–761	785–796	810–857	870–890	902–910
14	J-489	800	862–992	1034–1047	1071–1139	1163–1185	1202–1213
15	OR-2276-HT	864	867–1035	1087–1109	1135–1216	1243–1271	1291–1303
16	OR-2298-HT	864	876–1051	1103–1122	1149–1232	1260–1287	1311–1319
17	OR-2299-HT	880	867–1037	1087–1106	1133–1211	1239–1266	1290–1298
18	OR-2290-HT	886	876–1050	1103–1122	1149–1227	1258–1286	1306–1318
19	OR-2291-HT	872	892–1073	1128–1145	1178–1256	1287–1312	1335–1344
20	OR-2293-HT	879	878–1060	1113–1130	1163–1241	1270–1294	1318–1326
21	OR-2294-HT	871	886–1065	1119–1138	1165–1247	1275–1300	1321–1329
22	OR-2265-HT	889	903–1087	1143–1162	1195–1274	1303–1327	1351–1362
23	OR-2266-HT	878	898–1079	1135–1154	1182–1261	1292–1317	1337–1346
24	OR-2274-HT	888	874–1045	1098–1117	1143–1219	1247–1272	1290–1298
25	OR-2275-HT	868	904–1091	1148–1167	1195–1275	1306–1331	1354–1366
26	J-488	829	894–1038	1083–1096	1121–1185	1211–1233	1250–1259
27	J-490	809	891–1035	1077–1093	1115–1182	1205–1226	1244–1250
28	OR-2272-HT	846	890–1075	1132–1151	1182–1258	1290–1315	1338–1347
29	OR-2273-HT	852	890–1069	1123–1142	1170–1249	1278–1303	1324–1332
30	OR-2297-HT	878	891–1075	1131–1147	1178–1257	1286–1310	1334–1342
31	OR-2296-HT	879	892–1073	1129–1148	1176–1257	1286–1311	1331–1343
32	OR-2262-HT	873	888–1071	1124–1143	1174–1250	1284–1309	1329–1338
33	OR-2261-HT	875	881–1063	1116–1135	1166–1242	1273–1300	1321–1329
34	OR-2271-HT	845	882–1058	1113–1135	1163–1241	1269–1297	1317–1329
35	OR-2269-HT	847	887–1068	1123–1139	1172–1253	1281–1309	1329–1341
36	OR-2264-HT	883	869–1039	1092–1114	1141–1219	1246–1274	1294–1303
37	OR-2263-HT	873	873–1048	1098–1119	1149–1230	1257–1282	1305–1317
38	OR-1849-HT	816	869–1040	1095–1114	1143–1221	1248–1282	1302–1311
39	J-491	814	858–988	1031–1044	1067–1135	1156–1181	1198–1207
40	J-491	814	676–750	777–789	804–849	862–882	897–902
41	OR-2272-HT	846	680–780	812–827	845–902	920–946	961–970
42	OR-2273-HT	852	692–791	821–835	856–915	933–956	971–983
43	OR-2297-HT	878	693–788	820–835	850–909	927–952	967–982
44	OR-2296-HT	879	688–780	806–823	841–896	914–937	952–963
45	OR-2262-HT	873	695–783	811–825	843–901	916–942	953–968
46	OR-2261-HT	875	691–775	803–817	832–890	907–933	944–959
47	OR-2271-HT	845	689–769	794–808	825–883	898–923	934–952
48	OR-2269-HT	847	691–768	795–807	824–878	895–921	932–947
49	OR-2264-HT	883	689–765	789–806	820–877	894–920	931–946
50	J-490	809	694–769	793–807	821–877	894–920	931–945
51	OR-2263-HT	873	681–753	774–788	799–855	872–897	905–922
52	OR-2295-HT	881	686–737	752–763	773–815	829–845	856–867

[a]Oak Ridge National Laboratory.

[b]High Flux Isotope Reactor.

Thermal analysis provided operating temperatures for capsules HT-28, -29, and -30 as follows:

HT-28 — operating temperatures for this capsule were much higher than initially designed (low temperature — 900°C; high temperature — 1250°C). In the low-temperature region operating temperatures ranged from about 950°C at beginning of life (BOL) to about 1250°C at end of life (EOL). In the high-temperature region the operating temperatures ranged from 1230°C at BOL to 1530°C at EOL. Only for the last irradiation cycle, 120, were the temperatures relatively stable, and at that point they were about 300°C higher than design for both regions.

HT-29 — this capsule operated closer to design temperatures than the HT-28. This resulted from the capsule redesign and from the preirradiation calculations being based on results from capsules HT-12 through -15 and HT-17 through -19. The operating temperatures ranged from a minimum of 200°C below design of 900°C at BOL to nearly 75°C above design at EOL.

HT-30 — operating temperatures for this capsule more closely matched the designed temperatures than did HT-28 or -29. The main reason for the lower temperatures during most of the irradiation was the use of only thorium as the initiated fuel. In the low-temperature region (design 900°C), operating temperatures ranged from 680°C to BOL to about 930°C at EOL. For the high-temperature region (design 1250°C), operating temperatures ranged from 870°C at BOL to a peak of 1350°C at EOL. In both low- and high-temperature regions, design temperatures were not reached until the latter part of cycle 118B or 120. The operating temperatures followed the axial flux profile of HFIR: low temperatures resulted in low flux at capsule ends, and high temperatures resulted in high flux near reactor horizontal midplane. Since no fissile material was present initially, the operating temperatures at BOL result from only gamma heating in the capsule components. This temperature (fuel centerline) increases with time as some of the ^{232}Th is converted to the fissile ^{233}U. The amount of ^{233}U present as a function of time can be determined by the linear heat rates shown in the Appendix.

POSTIRRADIATION EXAMINATION

Capsule Disassembly

HT-28

A circumferential cut was made through the bottom of capsule HT-28 for the removal of magazines, and all were removed easily. Removing the particle holders from the low-temperature magazines 1 and 4 was not difficult, and they were in good condition. Magazines from the high-temperature region had to be slit to remove the crucibles. In these two magazines some of the zirconium "getter" wafers adhered to the holders and caused them to stick together. However, the reaction with the zirconium was not extensive enough to contact any particles. The particles from all holders were recovered for visual examination.

HT-29

A circumferential cut was made through the bottom of the capsule, and all graphite magazines were removed easily. The results of removal are as follows:

Magazine 1 — holder 1 was crushed during removal. All other holders were removed successfully, and the particles were recovered.

Magazine 2 — this magazine had to be progressively chipped open to remove the holders. Holder 23 was crushed, but all particles were thought to be recovered. Holder 18 was inadvertently crushed, and the particles were removed while the holder was still in the magazine. Holder 20 also had particles removed while still in the magazine. All other holders were removed in good condition. Holder 21 was crushed when the cap was being unscrewed, but all particles were believed to have been recovered.

Magazine 3 — the top end plug (ML-2) came out with holder 27. The magazine had to be slit open to remove the other holder, but they apparently were not damaged during this operation. Many of the holders stuck together. We could not separate holder 32 from 33 and 35 from 36.

Holders 32 and 33 were both broken during disassembly. Some of the particles from holder 33 were recovered separately, but the rest from holder 33 and all from 32 were mixed together. All other holders were opened, and the particles were recovered.

Magazine 4 — all the holders were easily removed. The particles were recovered for further examination.

HT-30

The capsule was cut open at the bottom, and all magazines were removed easily. The results of removal are as follows:

Magazine 1 — both top and bottom end plugs were removed without spilling any particles. The fuel rods were removed intact.

Magazine 2 — the loose particles in the top end plug were spilled, but their identity was maintained.

Magazine 3 — the loose inert particles fell out of the top end plug. They remained in the bottom end plug until later removal. Rods 35 through 39 came out at the same time. Rods 38 and 39 were positively identified. Rods 35 through 37 were not; however, they were put into what was believed the right order. All rods were removed intact. There was no apparent reaction with the zirconium wafers.

Magazine 4 — all rods were removed intact.

Capsule Gas Sampling

Gas samples were taken from all three capsules before disassembly and were analyzed by mass spectrometry. The results of the analyses in Table 19 confirmed that the correct backfill gas was used and that no leaks developed during irradiation, although the moisture contents were higher than expected. The higher krypton and xenon contents in HT-28 indicated that more coating failures or fast-neutron-induced pyrocarbon permeability occurred in this capsule than in either HT-29 or -30.

Table 19. Capsule Gas Sample Analyses

Gas	Quantity, %		
	HT-28	HT-29	HT-30
H_2	0.1	0.04	<0.1
He	7.1	98.99	5.9
H_2O	0.9	0.34	1.7
Ne			89.5
N_2 + CO	0.3	0.22	0.4
O_2	0.1	0.02	0.2
Ar	89.3	0.24	2.2
CO_2	0.1	0.03	0.1
Kr	0.2	0.03	<0.05
Xe	2.0	0.09	<0.05

Dimensional Measurements

Dimensions were measured for graphite holders in HT-28 and -29 and for fuel rod specimens in HT-30. Dimensional changes for these are given in Tables 20 and 21.

Table 20. Average Diametral Dimensional Changes on Graphite Holders for HT-28 and -29

Position	HT-28		HT-29	
	Change (%)	Fast Fluence[a] (neutrons/m^2)	Change (%)	Fast Fluence[a] (neutrons/m^2)
2	+1.30	4.58×10^{-25}	+0.83	5.73×10^{-25}
4	+1.40	5.11	+1.14	6.40
5	+1.12	5.34	+0.86	6.69
7	+1.30	5.84	+0.62	7.32
8	+1.38	6.07	+1.12	7.61
10	+1.22	6.54	+0.68	8.19
11	+1.19	6.77	+0.70	8.48
13	+1.12	7.15	+0.60	8.96
15	+0.34	8.15	+0.44	10.21
17	+0.75	8.42	+0.99	10.55
18	+0.86	8.52	*b*	10.67
20	+0.68	8.69	*b*	10.88
21	+0.75	8.77	*b*	10.98
23	+1.12	8.88	*b*	11.12
24	+0.91	8.92	+0.99	11.17
26	+0.73	9.00	*c*	11.27
27	+0.73	9.00	*b*	11.27
29	+1.14	8.92	+1.09	11.17
30	+0.96	8.88	+1.40	11.12
32	+0.86	8.77	+1.43	10.98
33	+0.49	8.69	+1.48	10.88
35	+1.04	8.52	+1.12	10.67
36	+0.57	8.42	+1.25	10.55
38	+0.60	8.15	+0.73	10.21
40	+0.75	7.15	+0.73	8.96
42	+0.99	6.77	*b*	8.48
43	+0.99	6.54	*b*	8.19
45	+1.32	6.07	+1.12	7.61
46	+1.01	5.84	+0.78	7.32
48	+1.12	5.34		6.69
49	+1.35	5.11	+1.43	6.40
51	+1.35	4.58	+0.86	5.73

[a]>0.18 MeV (>29 fJ).

[b]Damaged or crushed during disassembly.

[c]Not determined.

Table 21. Summary of Results of Dimensional Measurements on Fuel Rods from HT-30

Capsule Position	Postirradiation Diameter (mm)	Postirradiation Diameter (in.)	$\Delta D/D^a$ (%)	Postirradiation Diameter (mm)	Postirradiation Diameter (in.)	$\Delta L/L^b$ (%)	Design Temperature (°C)	Fast Fluence[c] (neutrons/m^2)
1	9.322	0.3670	−2.86	7.028	0.2767	−1.95	900	4.31×10^{25}
2	9.291	0.3658	−2.97	6.502	0.2560	−2.51	900	4.58
3	9.301	0.3662	−3.02	6.520	0.2567	−2.43	900	4.92
4	9.225	0.3632	−3.61	6.642	0.2615	−1.88	900	5.11
5	9.228	0.3633	−3.61	6.546	0.2577	−2.83	900	5.34
6	9.223	0.3631	−3.71	6.571	0.2587	−2.96	900	5.61
7	9.192	0.3619	−3.75	6.543	0.2576	−3.34	900	5.84
8	9.205	0.3624	−3.87	6.500	0.2559	−3.69	900	6.07
9	9.202	0.3623	−4.23	6.472	0.2548	−3.56	900	6.31
10	9.189	0.3618	−3.98	6.492	0.2556	−3.73	900	6.54
11	9.180	0.3614	−3.99	6.576	0.2589	−2.85	900	6.77
12	9.197	0.3621	−3.88	6.513	0.2564	−3.68	900	6.99
13	9.195	0.3620	−3.77	6.363	0.2505	−3.13	900	7.15
14	8.994	0.3541	−5.97	6.568	0.2586	−3.00	1250	8.00
15	8.941	0.3540	−6.10	6.533	0.2572	−5.48	1250	8.15
16	9.027	0.3554	−5.50	6.624	0.2608	−2.47	1250	8.27
17	9.007	0.3546	−6.19	6.436	0.2534	−5.90	1250	8.42
18	9.017	0.3550	−5.86	6.421	0.2528	−7.70	1250	8.52
19	9.007	0.3546	−5.67	6.464	0.2545	−5.46	1250	8.61
20	9.002	0.3544	−6.04	6.452	0.2540	−5.79	1250	8.69
21	9.027	0.3554	−5.75	6.774	0.2667	−2.31	1250	8.77
22	9.032	0.3556	−5.25	6.566	0.2585	−6.20	1250	8.84
23	9.017	0.3550	−5.46	6.591	0.2595	−6.15	1250	8.88
24	8.979	0.3535	−6.58	6.436	0.2534	−8.19	1250	8.92
25	9.014	0.3549	−5.51	6.472	0.2548	−6.43	1250	8.96
26	9.022	0.3552	−5.66	6.533	0.2572	−4.28	1250	9.00
27	9.032	0.3556	−5.63	6.452	0.2540	−6.03	1250	9.00
28	9.017	0.3550	−5.81	6.480	0.2551	−5.87	1250	8.96
29	9.007	0.3546	−6.12	6.480	0.2551	−4.28	1250	8.92
30	9.004	0.3545	−5.92	6.444	0.2537	−6.52	1250	8.88
31	9.022	0.3552	−5.68	6.627	0.2609	−3.51	1250	8.84
32	8.989	0.3539	−6.03	6.444	0.2537	−6.42	1250	8.77
33	8.984	0.3537	−6.16	6.515	0.2565	−5.73	1250	8.69
34	8.997	0.3542	−5.97	6.490	0.2555	−5.27	1250	8.61
35	9.002	0.3544	−5.69	6.525	0.2569	−4.00	1250	8.52
36	8.979	0.3535	−5.30	6.485	0.2553	−7.26	1250	8.42
37	9.025	0.3553	−5.58	6.403	0.2521	−6.32	1250	8.27
38	9.002	0.3544	−5.84	6.528	0.2570	−3.75	1250	8.15
39	9.032	0.3556	−5.58	6.528	0.2570	−4.43	1250	8.00
40	9.180	0.3614	−4.11	6.467	0.2546	−2.97	900	7.15
41	9.195	0.3620	−4.00	6.462	0.2544	−3.53	900	6.99
42	9.208	0.3625	−3.69	6.447	0.2538	−3.53	900	6.77
43	9.195	0.3620	−3.80	6.528	0.2570	−6.51	900	6.54
44	9.197	0.3621	−3.95	6.756	0.2660	−3.90	900	6.31
45	9.202	0.3623	−3.72	6.637	0.2613	−3.61	900	6.07
46	9.205	0.3624	−3.69	6.528	0.2570	−6.51	900	5.84
47	9.230	0.3634	−3.61	6.538	0.2574	−5.61	900	5.61
48	9.246	0.3640	−3.55	6.449	0.2539	−3.39	900	5.34
49	9.240	0.3638	−3.45	6.614	0.2604	−3.05	900	5.11
50	9.279	0.3653	−2.95	6.513	0.2564	−2.55	900	4.92
51	9.317	0.3668	−2.89	6.657	0.2621	−2.96	900	4.58
52	9.327	0.3672	−2.70	6.612	0.2603	−1.77	900	4.31

[a] D = diameter.

[b] L = length.

[c] >0.18 MeV (>29 fJ).

Visual Examination

The loose particles from HT-28 and -29 were loaded into a holder designed so that each particle could be examined with the aid of a stereomicroscope and could be photographed. Most of the loose particles had a grayish or white deposit on the coatings. The particles from each holder were counted. In some cases numbers of failed particles could only be estimated because of the debris. The percent of failed particles is given in Tables 22 and 23.

The fuel rod specimens from HT-30 were examined and photographed (Fig. 17). A summary of the visual examination is given below.

Rods 1 through 13 — no unusual features visible, no debonding, and no apparent broken particles. All rods had some matrix cracks, but these were relatively small and did not extend through any one rod.

Rods 14 through 26 — rods 14, 16, 19, and 24 had some debonding at the edges, and some of the other rods had a few particles missing at the edges. Broken particles were not evident.

Rods 27 through 39 — practically every rod had a few particles missing on the edges, but broken particles were not evident.

Rods 40 through 52 — little or no debonding was apparent, and apparently no broken particles were evident.

Particle Failure Determination for Fuel Rods

The particle failure fractions for experiments HT-28 and -29 were determined by visual examination, as previously described (Tables 22 and 23). Particle failure of the bonded rods was determined by chlorine leaching. Fuel rods from the high- and low-temperature magazines of capsule HT-30 and unirradiated Biso-coated thoria particle samples from the various particle lots used to load the rods were subjected to chlorine leach at 1000°C to determine the postirradiation particle failure fraction. The chlorine leach data for the irradiated rods and corresponding archive particles are presented in Table 24. With only three exceptions the rods and particles contained essentially no defective

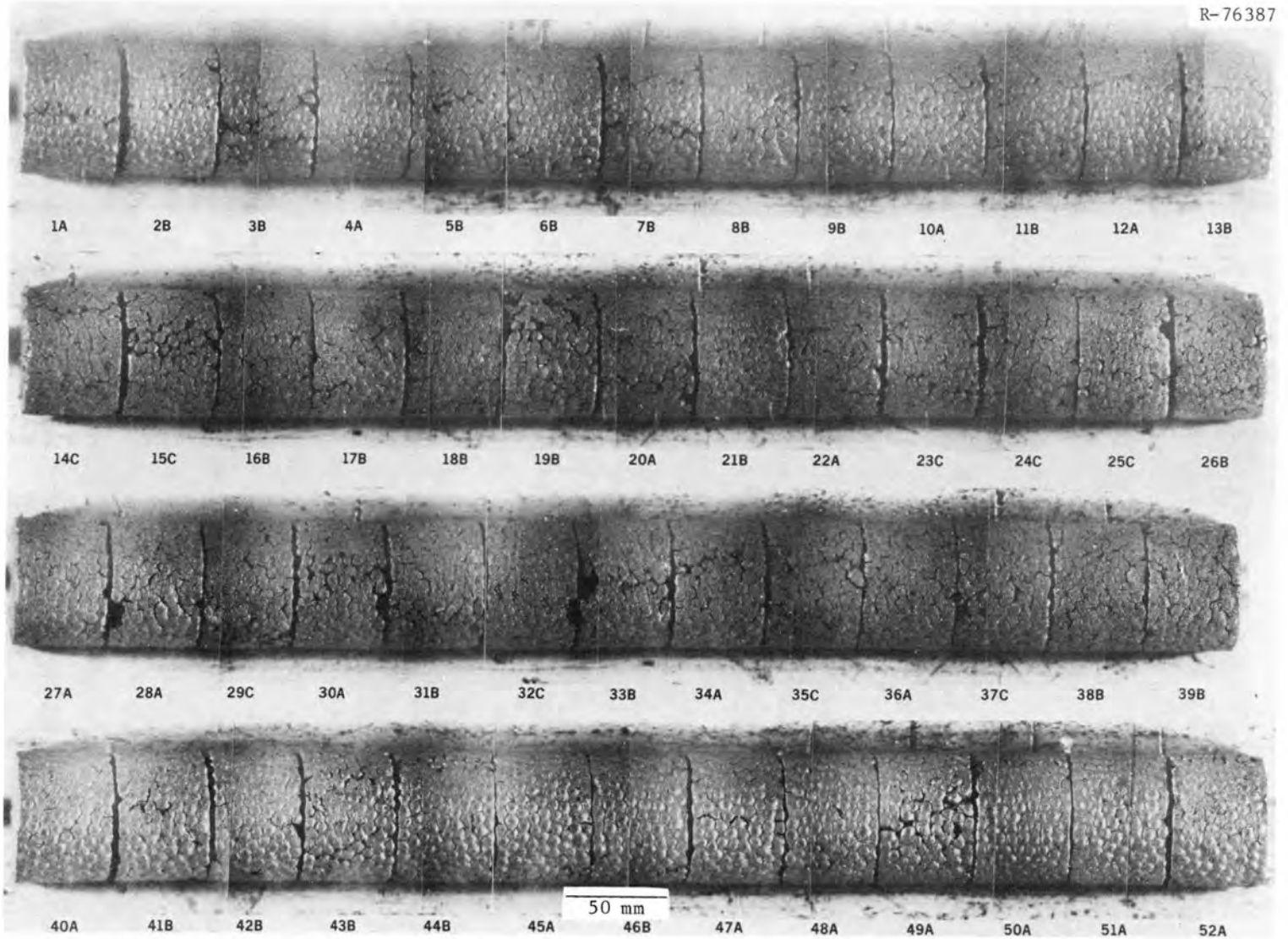

Fig. 17. General Appearance of Fuel Rod Specimens from HT-30 After Irradiation.

Table 22. Results of Stereoexamination of Loose Coated Particles From HT-28

Capsule Position	Specimen Lot	Design Temperature (°C)	Number of Particles		Failed Particles (%)	Fast Fluence[a] (neutrons/m^2)	Burnup (% FIMA[b])	Number of Particles Irradiated
			Intact	Failed				
2	6252-04[c]	900	34	0	0	4.58×10^{-25}	4.90	34
4	6252-03[c]	900	35	1	2.8	5.11	5.40	36
5	6542-28	900	37	2	5.1	5.34	5.62	41
7	6252-05[c]	900	34	2	5.6	5.84	6.10	36
8	OR-2294-HT	900	37	0	0	6.07	6.30	39
10	OR-2666-HT	900	39	1	2.5	6.54	6.70	39
11	6542-22	900	31	7	18.4	6.77	6.90	41
13	6542-01	900	37	5	11.9	7.15	7.21	41
15	6542-28	1250	56	0	0	8.15	8.21	57
17	6542-30	1250	51	0	0	8.42	8.40	51
18	6252-04[c]	1250	40	3–4[d]	6.9–9.0[d]	8.52	8.49	47
20	6252-03[c]	1250	29	6–7[d]	17.1–19.4[d]	8.69	8.62	51
21	OR-2294-HT	1250	54	0	0	8.77	8.69	55
23	OR-2266-HT	1250	56	0	0	8.88	8.80	55
24	6542-22	1250	58	0	0	8.92	8.85	58
26	6542-01	1250	58	0	0	9.00	8.91	58
27	6542-24	1250	54	0	0	9.00	8.91	54
29	OR-2273-HT	1250	25	7–9[d]	21.8–26.4[d]	8.92	8.85	55
30	OR-2297-AHT	1250	55	1–2[d]	1.8–3.5[d]	8.88	8.80	55
32	OR-2262-HT	1250	53	0	0	8.77	8.69	55
33	6542-35	1250	57	0	0	8.69	8.62	57
35	6542-29	1250	58	0	0	8.52	8.49	58
36	6542-34	1250	51	0	0	8.42	8.40	58
38	6542-27	1250	53	0	0	8.15	8.21	53
40	6542-24	900	38	0	0	7.15	7.21	38
42	OR-2273-HT	900	39	0	0	6.77	6.90	39
43	OR-2297-AHT	900	39	0	0	6.54	6.70	39
45	OR-2262-HT	900	38	0	0	6.07	6.30	39
46	6542-35	900	38	2	5.0	5.84	6.10	40
48	6542-29	900	41	0	0	5.34	5.62	41
49	6542-34	900	41	0	0	5.11	5.40	41
51	6542-27	900	37	0	0	4.58	4.90	37

[a]>0.18 MeV (>29 fJ).

[b]Fissions per initial metal atom.

[c]Triso-coated gas particles; all others Biso-coated.

[d]Estimated range from coating fragments; conservative coating failure fraction.

Table 23. Results[a] of Stereoexamination of Loose Coated Particles From HT-29

Capsule Position	Specimen Lot	Number of Particles		Failed Particles (%)	Fast Fluence[b] (neutrons/m^2)	Burnup (% FIMA[c])	Number of Particles Irradiated
		Intact	Failed				
2	OR-2264	90	0	0	5.73×10^{-25}	7.15	100
4	OR-2294	100	0	0	6.40	7.85	100
5	6542-22	102	1–2	1–2	6.69	8.20	106
7	6542-01	103	0	0	7.32	8.80	105
8[d]	6252-04	86	0	0	7.61	9.09	86
10[d]	6252-03	93	0	0	8.19	9.60	93
11	6542-28	104	0–1[e]	0–0.95	8.48	9.89	104
13	6542-30	93	0	0	8.96	10.30	93
15	OR-2291	59	0	0	10.21	11.40	59
17[d]	6252-04	50	0	0	10.55	11.70	50
18[d]	6252-03	53	0	0	10.67	11.80	54
20[d]	6252-05	53	0	0	10.88	12.00	54
21	6542-30	53	1	1.85	10.98	12.10	54
23	OR-2262	59	1[e]	1.67	11.12	12.20	59
24	6542-22	54	3–4[e]	5.26–6.90	11.17	12.30	58
26	6542-01	63	0	0	11.27	12.40	62
27	6542-24	54	0	0	11.27	12.40	54
29	OR-2299	59	0	0	11.17	12.30	59
30	OR-2261	58	0	0	11.12	12.20	59
32	6542-35	79[f]	0	0	10.98	12.10	60
33	6542-29	41[f]	0	0	10.88	12.00	62
35	6542-34	57	0	0	10.67	11.30	62
36	6542-27	54	0	0	10.55	11.70	56
38	OR-2290	59	0	0	10.21	11.40	59
40	6542-34	106	0	0	8.96	10.30	106
42	6542-29	198[g]	0	0	8.48	9.89	106
43[d,g]	6252-05				8.19	9.60	92
45	6542-27	90	0	0	7.61	9.09	96
46	6542-24	99	0	0	7.32	8.80	99
48	OR-2298	23–24	0	0	6.69	8.20	100
49	OR-2293	99	0	0	6.40	7.85	100
51	OR-2263	100	0	0	5.73	7.15	100

[a]Design temperature, 900°C.

[b]>0.18 MeV (>29 fJ).

[c]Fissions per initial metal atom.

[d]Triso-coated General Atomic Company particles; all others Biso-coated.

[e]Estimated from coating fragments; conservative coating failure fraction.

[f]Some particles from crucible 33 mixed with 32.

[g]Particles from crucibles 42 and 43 mixed together.

Table 24. Chlorine Leach Analyses for Irradiated Rods and Archive Paricles Used in HT-30

Irradiated Rods[a]			Unirradiated Particles[a]		
Capsule Position	Chlorination Time[b] (h)	Thorium Recovered (μg)	Batch	Chlorination Time[b] (h)	Thorium Recovered (μg)
12	32	<5	OR-2275-AHT		
13	32	<5	J-489		
14[c]	20	0.6	J-489	18	0.5
15[d]	*d*	*d*	OR-2276-HT	19	0.5
16	24	1.6	OR-2298-HT	18	0.5
17	18	1.6	OR-2299-HT	18	0.5
18	18	1.6	OR-2290-HT	18	1.6
19	18	0.5	OR-2291-HT	18	1.6
20	18	1.1	OR-2293-HT	18	0.0
21	18	4.7	OR-2294-HT	20	1.1
22	18	2.1	OR-2265-HT	20	1.1
23	18	4.7	OR-2266-HT	18	0.0
24	18	1.1	OR-2274-HT	19	410
25[c]	20	0.6	OR-2275-HT	16	1.6
26	18	1.6	J-488	19	0.0
27	20	1.1	J-490	20	1.1
28	19	1.6	OR-2272-HT	20	1.1
29	19	1.1	OR-2273-HT	20	0.5
30	19	1.1	OR-2297-HT	20	1.6
31	19	420	OR-2296-HT	20	0.5
32[c]	20	0.6	OR-2262-HT	16	0.5
33	20	1.1	OR-2261-HT	20	0.0
34	20	1.6	OR-2271-HT	16	0.0
35	60	393	OR-2269-HT	20	0.0
36[c]	20	0.6	OR-2264-HT	20	1.1
37	16	4.2	OR-2263-HT	19	0.0
38	20	2.1	OR-2295-HT	20	1.6
39[c]	20	0.6	J-491	22	0.5
40	32	<5	J-491		
45	32	<5	OR-2262-HT		
49	32	<5	OR-2264-HT		

[a]Fuel rods 14 through 39 and unirradiated samples contained 57 Biso-coated thoria particles. Each contained 0.0339 g Th. Rods 12, 13, 40, 45, and 49 each contained 42 particles (0.0249 g Th). Thoria content of a particle = 595 μg.

[b]All samples leached at 1000°C.

[c]Rod sent to General Atomic Company for release-to-birth ratio measurement before chlorine leaching.

[d]Accidently destroyed because of air leakage into the system.

or failed particles and, in general, the thorium recovered by chlorine leach corresponds to the precision of the thorium analyses, ±1 μg.

Long-time chlorine leach data for one sample of loose unirradiated particles and one irradiated rod, which contained defective particles, are presented in Table 25. For both cases the sample was repeatedly chlorinated for approximately 20-h intervals, and after each chlorination interval the amount of thorium removed was determined. A radiograph of 57 unirradiated particles from OR-2274-HT after the final chlorination showed 5 particles with kernels completely removed and 8 particles with 5 to 90% of the kernel removed. The chlorination data and the radiograph indicate that the apparent particle failures result from permeable coatings. However, the corresponding irradiated rod HT-30-24 yielded only about 1 μg Th (i.e., zero failure fraction). This disparity may result from sealing of the particle coating by the rod binder in the irradiated specimen or indicate that much longer chlorination times are required for fuel rods.

Table 25. Results from Long-Time Chlorination of Unirradiated Loose Particles and an Irradiated Fuel Rod Used in HT-30

Unirradiated Loose Particles (OR-2274-HT)			Irradiated Fuel Rod 31 (OR-2296-HT)		
Chlorination Time (h)	Thorium		Chlorination Time (h)	Thorium	
	Recovered (μg)	Leached (%)		Recovered (μg)	Leached (%)
19	410	1.2	19	420	1.2
38	545	1.6	38	436	1.3
57	1565	4.6	60	441	1.3
76	2680	7.9	80	450	1.3
95	3440	10	100	471	1.4
114	3912	12	120	557	1.6
134	4504	13	148	919	2.7

The chlorine leach data for irradiated rod HT-30-31 indicated that one defective particle with a cracked coating was detected in the initial chlorination interval and that permeability of the coatings developed with successive chlorinaion intervals. The leach results from the corresponding unirradiated sample (OR-2296-HT), however, did not indicate either defective or permeable coatings.

Fission-Gas Release-to-Birth Ratios, Fission Gas Contents, and Long-Term Chlorine Leaching Studies

Five fuel rods from the high-temperature region of HT-30 were evaluated by activation analysis in the Training, Research, Isotope, General Atomic (TRIGA) reactor at GA. The rods selected for activation analysis contained particles with neon-to-helium ratios that ranged from 0.13 to 0.41 and NAF values from 0.97 to 1.46 and particles from one batch (OR-2275-HT) that indicated thorium loss during chlorine leaching of the as-deposited coatings. The release-to-birth (R/B) ratios for ^{85m}Kr obtained during the test in TRIGA at 1100°C for 0.5 h gave no indication of defective particles. The R/B values are listed in Table 26. Subsequent to the TRIGA test the five fuel rods were returned to ORNL for chlorine leaching and fission-gas inventory measurements. The results from chlorine leaching (p. 51) appeared to confirm the R/B data: no failed or permeable coatings were indicated in these particular rods.

After chlorine leaching, the five rods were electrolytically deconsolidated, and the solid fission-product inventories of four or five particles from each rod were determined by gamma spectrometry. The results showed that Zr, Ru, Cs, and Ce were retained in the particles. Fission-gas inventories for the individual particles were calculated from the gamma spectrometric results. The fission-gas inventories were measured by cracking individual particles at 1000°C and by measuring the volume of noble gases present after gettering the active gases. Typical release values of 40 to 50% of the fission gases generated in dense thoria kernels at irradiation conditions for HT-30 would be expected.

Particles from the fifth batch (OR-2275-HT) had an average fission-gas content of only 13%. Since the particles from batch OR-2275-HT had the highest neon-to-helium ratios and the highest NAF value and were leachable before irradiation, the coatings probably were permeable and released a portion of the fission-gas inventory during irradiation.

This result questions the validity of using the R/B TRIGA test for identifying particles with permeable coatings. Also, why chlorine leaching did not indicate that the coatings were permeable in the irradiated fuel rod is questionable. Since only a portion of the fission gas

Table 26. Results of Fission-Gas Release-to-Birth and Release Measurements on Five Rods from Capsule HT-30

Irradiation Rod and Particle	Batch	Design Irradiation Conditions			TRIGA[c] R/B ^{85m}Kr	Burnup Determination by Fission Product Inventory, % FIMA[a]				Average Burnup[d] (% FIMA[a])	Kr and Xe Released (%)	Ne/He	NAF[e]
		Burnup (% FIMA[a])	Fast Fluence,[b] HTGR (neutrons/m^2)	Temperature (°C)		^{95}Zr	^{106}Ru	^{137}Cs	^{144}Ce				
HT-30-14-1						6.82	7.27	7.97	6.91	7.00	54.8		
2	J489	7.5	7.6×10^{25}	1250	3.9×10^{-6}	6.64	7.55	7.87	6.91	7.03	51.1	0.28	*f*
3						6.89	7.29	8.03	7.14	7.11	46.7		
4						7.17	7.53	8.12	7.03	7.24	47.3		
HT-30-25-1						5.44	5.90	6.18	5.34	5.56	21.4		
2						6.16	6.38	6.46	5.62	6.05	3.2	0.41	1.46
3	OR2275	8.4	8.6	1250	2.2	5.66	5.54	6.33	5.40	5.53	7.7		
4						5.89	6.02	6.43	5.56	5.82	17.0		
5						5.47	5.83	6.32	5.51	5.60	17.7		
HT-30-32-1						5.99	6.33	6.84	5.93	6.08	35.7		
2						6.28	6.50	6.96	5.99	6.26	39.8		
3	OR2262	8.2	8.4	1250	12.0	5.71	6.70	7.06	6.31	6.24	40.2	0.20	1.22
4						6.20	6.68	6.99	5.99	6.29	46.0		
HT-30-36-1						6.52	6.61	7.19	6.20	6.44	34.7		
2						6.46	7.61	7.41	6.31	6.79	46.1		
3						6.85	7.05	7.26	6.36	6.75	42.3		
4	OR2264	7.9	8.1	1250	2.5	6.55	7.06	7.39	6.52	6.71	38.0	0.13	0.97
HT-30-39-1						7.08	7.68	7.97	6.91	7.22	33.6		
2						7.05	7.74	8.10	7.20	7.33	45.0		
3	J491	7.5	7.6	1250	4.2	7.23	7.12	7.88	7.03	7.13	36.7	0.41	*f*
4						6.85	7.51	7.79	6.68	7.01	43.2		

[a]Fissions per initial metal atom.

[b]>0.18 MeV (>29 fJ).

[c]Training, research, isotope, General Atomic reactor at General Atomic Company. R/B = release-to-birth ratio.

[d]Average burnup values determined neglecting cesium inventory measurement.

[e]Normalized amount of fiber component.

[f]Not determined.

was released during irradiation, indicating a relatively low gas-permeability value, the residence time in TRIGA and the chlorination time may have been too short to indicate permeability.

Permeability of LTI Coatings of Inert Particles in HT-30

The inert particles from HT-30, which were placed in the magazine end plugs, were examined for radiation-induced permeability change. The permeability was determined by the standard neon-helium content measurement after heat treating in neon-helium at 1375°C, but results were obscured by the HT-30 capsule being backfilled with neon. Table 27 shows that for particles in the lower temperature zones, the indicated permeability decreased during irradiation. However, test samples irradiated at higher temperatures had an indicated increase in permeability, that is, increase in the neon-to-helium ratio. This probably was caused by diffusion of neon into the particles during the relatively long irradiation period and does not necessarily mean that irradiation caused the permeability of these pyrocarbon coatings to increase.

Table 27. Results of Measuring Permeability of Biso-coated Inert Particles from Batch OR-2291-HT[a] Irradiated in HT-30

Fast Fluence[b] (neutrons/m^2)	Irradiation Temperature (°C)	Gas Content[c] per Particle		Ne/He
		He (pmol)	Ne (pmol)	
Control		153	41	0.27
3.6×10^{25}	900	101	23	0.23
7.2	900	116	23	0.20
7.5	1250	101	90	0.89
8.6	1250	112	141	1.26

[a]Coated simultaneously with fertile particles (also designated OR-2291-HT) and later separated by using a gradient density column.

[b]>0.18 MeV (>29 fJ).

[c]Average gas content of ten particles at each flux position.

Other Materials in HT-28 and -29

The material supplied by LASL in HT-28 and -29 was recovered and examined. The extruded graphite specimens in HT-28 and the zirconium-carbide wafers in HT-29 were dimensionally measured and photographed. No outstanding features were observed in either case. The inert particles in the end plugs of both experiments were retrieved, visually examined, and photographed. This information and the materials were shipped to LASL. The GA particles in the experiments were photographed and shipped to GA for further examination. The results from additional postirradiation examinations have been reported separately.[13]

COMPARISON OF NAF WITH IRRADIATION PERFORMANCE

Pressure from both fission gas that originates in the fuel kernel and high stresses caused by irradiation-induced anisotropic dimensional changes may lead to cracks in pyrocarbon coatings. Although the fission-gas pressure can be reduced by providing sufficient porosity in kernel and buffer layer, the irradiation performance of the LTI coatings seems to be very sensitive to microstructural variations. Regions of equally oriented and closely packed crystallites measuring to 1 μm in diameter are present in the mosaic component. The irradiation-induced anisotropic dimensional changes of these large regions lead to a poor performance of the mosaic component. On the other hand this component shows a high preirradiation fracture stress and a low permeability for gaseous fission products. In contrast to this the more or less randomly oriented fibers and the enclosed fine pores will lead to a strong but isotropic irradiation-induced shrinkage of the fiber component. In addition, the initial fracture stress will be low and the permeability for gases relatively high. As the C-axes of the fibers are perpendicular to the fiber axis and the crystallite size L_c is only about 2.5 to 3.4 nm, the minor dimensional changes of the tangled fibers will be buffered by the pores between the fibers. In addition, the fiber component may act as a buffer for the large anisotropic dimensional changes of the mosaic component.

Since the NAF indicates the ratio of the tangled material and the mosaic component, the NAF was compared with the irradiation performance of LTI coatings. The failure fractions of the loose particles were determined by stereoexamination. Particles in the bonded rods were analyzed by chlorine leaching. Visual examination (p. 51) of the loose coated particles from HT-28 and -29 revealed that only four batches contained failed (fractured) coatings. (Chlorine leaching of the fuel rod specimens from HT-30 was discussed on pp. 51— 59.) However, combining these results with the NAF values and irradiation performance of loose, Biso-coated particles from a previous set of capsules[14] revealed several things. Figure 18 shows the failure rate of particles irradiated to fluences between 5×10^{25} and 10×10^{25} neutrons/m^2 [>0.18 MeV (>29 fJ)]. Particles with a NAF lower than 0.95 and with irradiation at all indicated temperatures failed at fluences higher than 5×10^{25} neutrons/m^2. Two batches of irradiated loose particles had failure fractions of 2 and 21%, whereas equivalent particles in rods showed no failures. The reason for the poor performance of these loose particles is not clear. The difference in behavior may result partially from reinforcement of the coatings by the matrix material and the thermal conductivity of rods, which is inherently better than loose beds of particles.

The failure fractions of particles irradiated to fluences ranging from 10×10^{25} to 15×10^{25} neutrons/m^2 are shown in Fig. 19. Particles with a NAF less than 0.95 again had a high failure fraction; particles with a NAF 1.0 or higher did not fail except for one batch of loose particles with 2% failure fraction.

The data shown in Figs. 18 and 19 indicate a strong dependency of LTI coating stability on the coating microstructure described by the NAF. In both diagrams the transition from coatings with poor irradiation performance to those with good behavior is extremely sharp. The minimum NAF value for good irradiation performance must be higher than 1.0, as dictated by HTR design requirements. Since the NAF of a LTI coating becomes larger with increasing deposition temprature and gas flux, that is, deposition rate, the NAF can be adjusted by controlling these parameters.

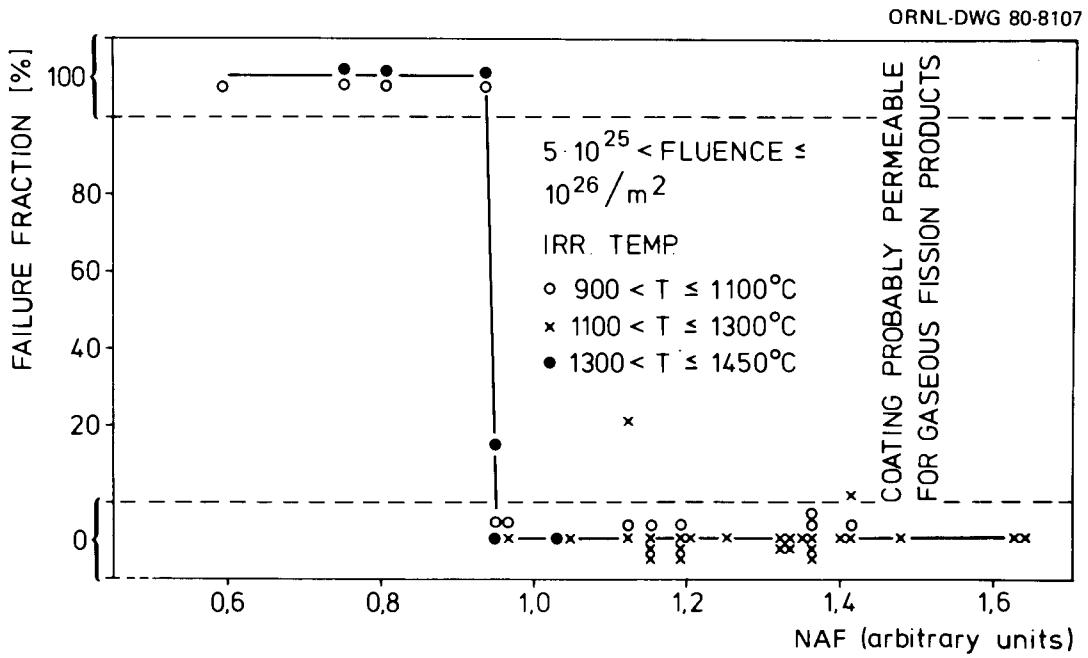

Fig. 18. Failure Fraction of Coatings Irradiated to Fluences of 10^{26} neutrons/m^2 [<0.18 MeV (<29 fJ)] as a Function of Normalized Amount of Fiber Component (NAF) Values.

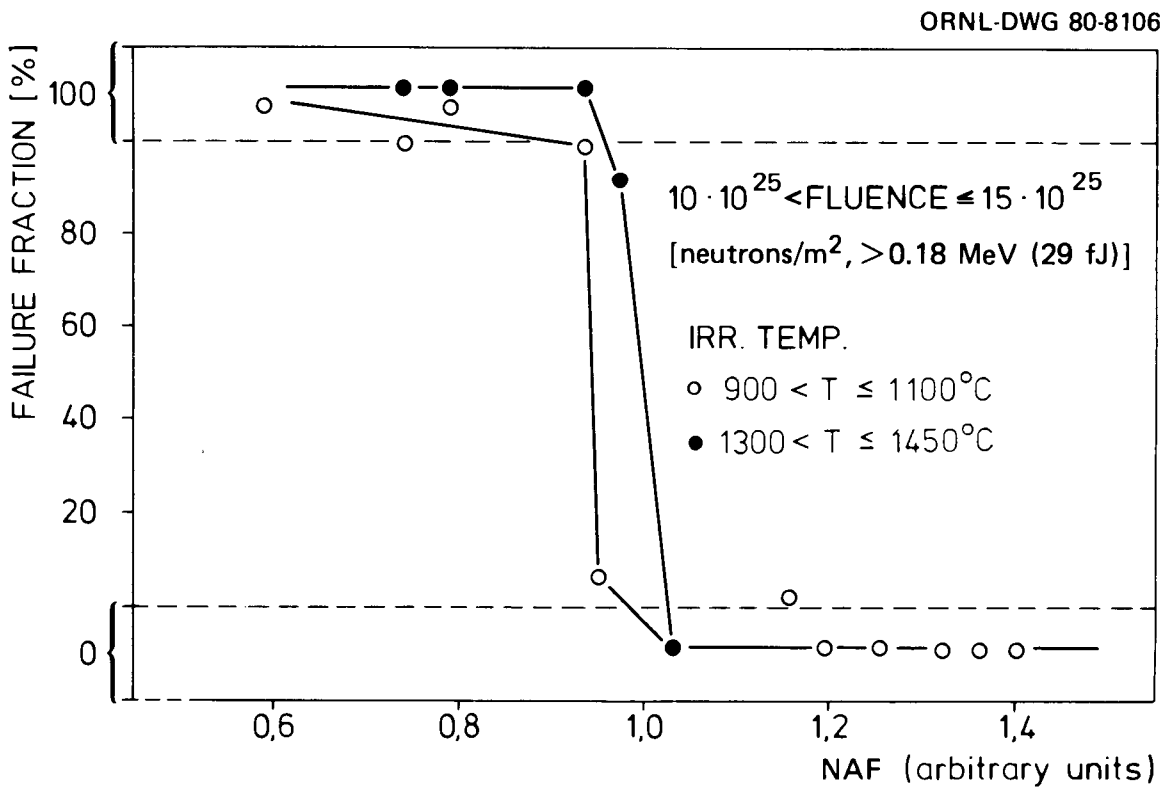

Fig. 19. Failure Fraction of Coatings Irradiated to Fluences of 1.5×10^{25} neutrons/m^2 [<0.18 MeV (<29 fJ)] as a Function of Normalized Amount of Fiber Component (NAF) Values.

PERMEABILITY — GENERAL REMARKS

Two forms of permeable coatings have been identified: preirradiation permeability and irradiation-induced permeability. We will elaborate on these.

Preirradiation Permeability

In the preceding sections neon-helium permeability measurements, microporosity data (NAF), hot gaseous chlorine leach tests, and static-pressure mercury intrusion measurements were discussed. All the above determinations yielded similar but not identical information about the tightness of as-deposited coatings. Neon diffusion, mercury intrusion, and chlorine leach are direct measurements using chemical and physical processes, while the NAF determinations describe the microstructure of the material. All the above tests indicate that an increase in permeability occurs with an increase in deposition temperature and, to a high degree, with deposition rate or hydrocarbon concentration. These changes in deposition conditions lead to an increase in the amount of fibrous component and an increase in pores larger than about 7 nm in diameter. A comparison of deposition conditions with immersion densities of these LTI coatings showed that an increase in deposition temperature led to a decrease in immersion density and to an increase in permeability. In contrast, an increase in deposition rate at a given temperature led to an increase in immersion density and also to higher permeability. Therefore, density and permeability are not unambiguously correlated.

Irradiation-Induced Permeability

As stated previously, all as-deposited coatings that were permeable had high NAF values. In contrast to this, LTI coatings have been identified in irradiation experiments,[14,15] other than HT-28 through -30, that became permeable during irradiation. The coatings in HT-17, -18, and -19 that became permeable had low NAF values. A low NAF indicates that an insufficient amount of the fiber component is in the microstructure of the

coating to accommodate the large irradiation-induced dimensional changes of the anisotropic mosaic component. It was therefore assumed that small cracks developed within the coatings during irradiation that relieved the internal gas pressure and thus prevented the coatings from failing. In fact, subsequent TEM investigations revealed that small cracks were present in the mosaic component of the as-deposited coatings and that the number and size of cracks increased during irradiation.[16] In addition, the mechanical stability of the permeable particles proved to be much lower when compared with impermeable coatings.

CONCLUSIONS

We used various methods to characterize microstructural features of pyrocarbon coatings derived under various conditions and to correlate the performance of coatings with the measured properties. The most consistent results were obtained by using parametric properties derived from SAXS measurements.

Although only four of the MAPP-gas-derived particle batches included in irradiation capsules HT-28, -29, or -30 failed mechanically, the irradiation performance of these particles fits the correlation between failure fractions and NAF values. Depending upon irradiation conditions, coatings with a NAF less than 0.95 to 1.05 will perform poorly. The coatings will either fracture or, as a prestate to fracturing, develop small cracks and release the gaseous fission products. The as-deposited coatings will be permeable to fission gases if the NAF value is greater than 1.45.

The various pore size intervals are related to the microstructural components of pyrocarbon and, as a consequence, to the various material properties. For example, the immersion density of these coatings was related to the number of pores less than 2.5 nm in diameter. The pores ranging from 6 to 25 nm in diameter, which are used to determine the NAF values for coatings, are related to gaseous permeability and irradiation stability. The fracture strength of pyrocarbon is strongly influenced by the number of pores 20 to 100 nm in diameter.

We have shown correlations between NAF values and mercury intrusion, chlorine leach, and neon-helium permeability. A correlation between mercury intrusion vs NAF and neon-helium permeability showed a nonlinear and linear relationship, respectively. Although it was not demonstrated, variations in the mercury intrusion results would occur depending on the pressure applied to the pyrocarbon coatings.

Fertile particles were included in capsules HT-28 through -30 that were prepared in beds containing both dense thoria and inert carbon kernels (diluted beds) in which coating conditions simulated those in a fissile-particle bed. This study demonstrated that certain properties of coatings derived in diluted fissile-type beds differ from those produced in normal fertile-type beds. Thus great care must be exercised if experiments conducted on coatings containing inert kernels are to yield meaningful results that can be correlated to referencable coating conditions.

ACKNOWLEDGMENTS

The authors wish to acknowledge the efforts of many people who made significant contributions in the planning, implementation, and evaluation of this experiment. W. P. Eatherly of the Metals and Ceramics Division and J. A. Conlin and B. H. Montgomery of the Engineering Technology Division participated in the planning, design, construction, and irradiation of these capsules. Metals and Ceramics Division members W. J. Lackey, J. B. Flynn, C. E. DeVore, B. R. Chilcoat, J. W. Geer, and C. Hamby produced the ORNL coatings; H. Keating assisted in coating characterization; and J M Robbins fabricated the fuel rods. W. J. Mason of the Metals and Ceramics Division radiographed the unirradiated particles. The BAF_o, phosgene-leach, and mercury intrusion measurements were performed by personnel in the Fuel Test Techniques Branch of General Atomic Company. Hot gaseous chlorine leaching at ORNL was performed under the direction of D. A. Costanzo of the Analytical Chemistry Division. The neon-helium measurements were made by G. L. Powell of the Y-12 Development Division. Thermal analysis was assisted by A. M. Howard from Purdue University. The authors also wish to express our thanks to our reviewers D. P. Stinton and J. I. Federer of the Metals and Ceramics Division for

their helpful comments and suggestions. We also wish to acknowledge the assistance of those who helped prepare this report — B. G. Ashdown for technical editing and K. A. Witherspoon for word processing and makeup.

REFERENCES

1. J. C. Bokros, "Deposition, Structure, and Properties of Pyrolytic Carbon," pp. 1–110 in *Chemistry and Physics of Carbon*, Vol. 5, ed. by P. L. Walker, Jr., Dekker, New York, 1969.
2. R. L. Beatty, "Irradiation Test Capsules HT-17, -18, and -19," *HTGR Base-Technology Program Prog. Rep. Jan. 1, 1974–June 30, 1975*, ORNL-5108, pp. 269–76.
3. J M Robbins and W. P. Eatherly, "Capsules HT-17 through -19," *Gas-Cooled Reactor Programs Annu. Prog. Rep. Dec. 31, 1973*, ORNL-4975, pp. 133–38.
4. M. J. Kania, T. B. Cindemer, M. T. Morgan, and J M Robbins, *Irradiation Performance of HTGR Fertile Fuel in HFIR Target Capsules HT-12 through HT-15. Part I — Experiment Description and Fission Product Behavior*, ORNL/TM-5305 (Feburary 1977).
5. J. P. Mathers et al., *Equipment Variables and Deposition Conditions Affecting the Plasma Oxidation of Pyrocarbon Coatings on HTGR Fuel Particles*, ORNL/TM-5308 (June 1976).
6. C. S. Yust and P. Krautwasser, "Transmission Electron Microscopy of Propene-Derived Carbon Coatings," *Carbon* 13(2): 125–33 (1975).
7. D. E. Lavalle et al., *The Determination of Defective Particle Fraction in HTGR Fuels*, ORNL/TM-5483 (November 1976).
8. A. Guinier and G. Fournet, *Small-Angle Scattering of X-Rays*, J. Wiley, New York, 1955.
9. P. Krautwasser, *About the Microporosity of Pyrocarbon Coatings Determined by X-Ray Measurements*, KFA Report, JÜL-1202 (1975).
10. P. Krautwasser, C. S. Yust, H. Luhleich, H. Nickel, and E. Pollman, "Identification of Three Components in Pyrocarbon Coatings by Transmission Electron Microscopy (TEM) and Measurements of Microporosity, Inner Surface, Degree of Order, and Crystalline Size," p. 157 in *Proc. Bien. Conf. Carbon, 12th*, Pittsburgh, July 1975.

11. H. Luhleich, L. Sütterlin, H. Hoven, and H. Nickel, "Bestimmung der Verteilung Von Amorphanteilen in Pyrokohl-Enstoff-Hüllschichten mit Hilfe der Kaltoxidation," *Z. Anal. Chem.* 255: 97–103 (1971).

12. M. J. Kania, *HTCAP — A Fortran IV Program for Calculating Coated Particle Operating Temperatures in HFIR Target Irradiation Experiments,* ORNL/TM-5332 (May 1976).

13. Paul Wagner, *High-Temperature Fuel Technology for Nuclear Process Heat: ZrC-Containing Coated Particle Fuels and High-Density Graphite Fuel Matrices,* LA-6984 (December 1977).

14. E. L. Long, Jr., R. L. Beatty, J M Robbins, M. J. Kania, and W. P. Eatherly, *Irradiation Performance of HTGR Biso Fertile Particles in HFIR Experiments HT-17, -18, and -19,* ORNL/TM-6414 (November 1978).

15. R. A. Bradley and B. A. Thiele, "Neutron-Induced Permeability of Pyrocarbon-Coated High-Temperature Gas-Cooled Reactor Fuel Particles," *Nucl. Technol.* 35(2): 353–58 (September 1977).

16. Personal communication, E. Pollmann, Institüt für Reactorwerkstoffe, Kernforschungsanlange, Jülich, Federal Republic of Germany, July 1976.

APPENDIX

DETAILED OPERATING TEMPERATURES FOR THE IRRADIATION LIFETIME OF HFIR TARGET CAPSULES HT-28, -29, and -30

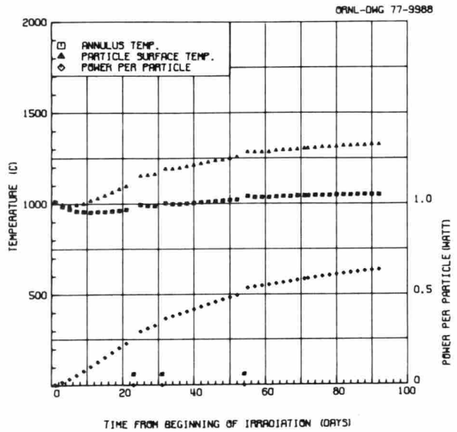

HT-28 PARTICLE HOLDER 8 BATCH OR-2294HT
871.0 MICRON PARTICLE DIAMETER

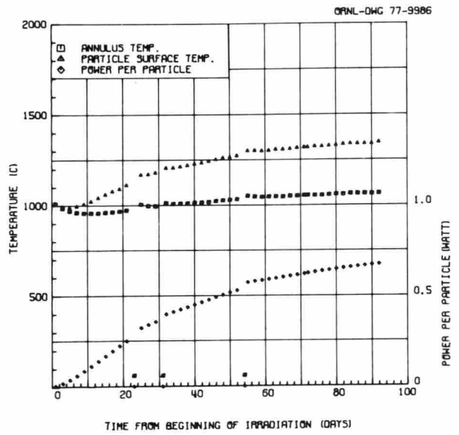

HT-28 PARTICLE HOLDER 10 BATCH OR-2266HT
878.0 MICRON PARTICLE DIAMETER

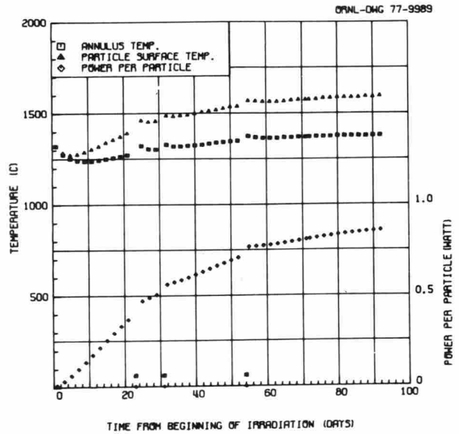

HT-28 PARTICLE HOLDER 21 BATCH OR-2294HT
871.0 MICRON PARTICLE DIAMETER

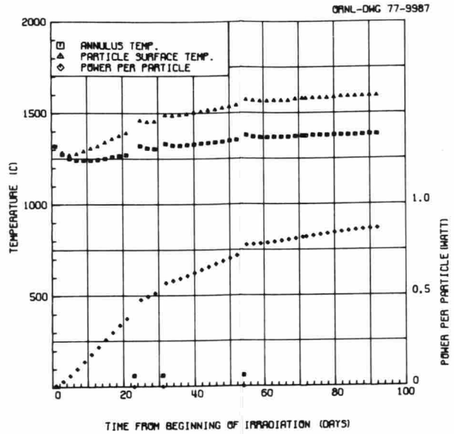

HT-28 PARTICLE HOLDER 23 BATCH OR-2266HT
878.0 MICRON PARTICLE DIAMETER

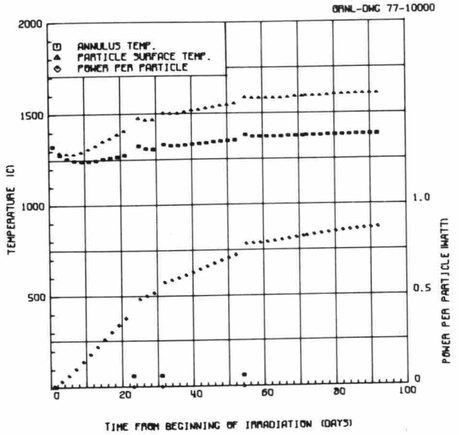

HT-28 PARTICLE HOLDER 29 BATCH OR-2273HT
852.0 MICRON PARTICLE DIAMETER

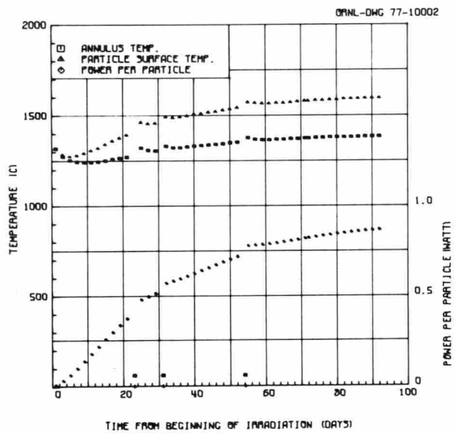

HT-28 PARTICLE HOLDER 30 BATCH OR-2297AHT
878.0 MICRON PARTICLE DIAMETER

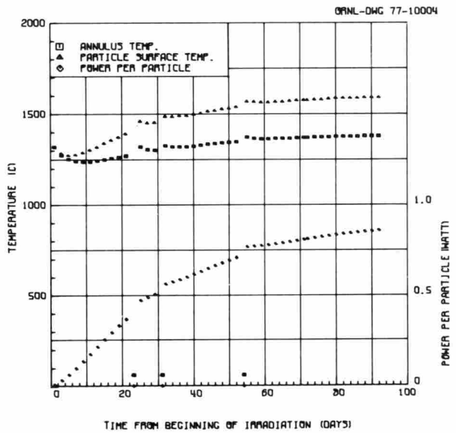

HT-28 PARTICLE HOLDER 32 BATCH OR-2262HT
873.0 MICRON PARTICLE DIAMETER

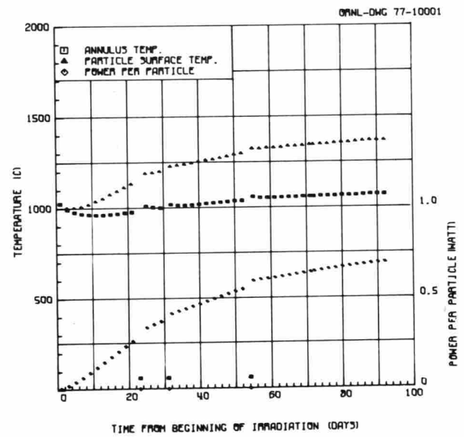

HT-28 PARTICLE HOLDER 42 BATCH OR-2273HT
852.0 MICRON PARTICLE DIAMETER

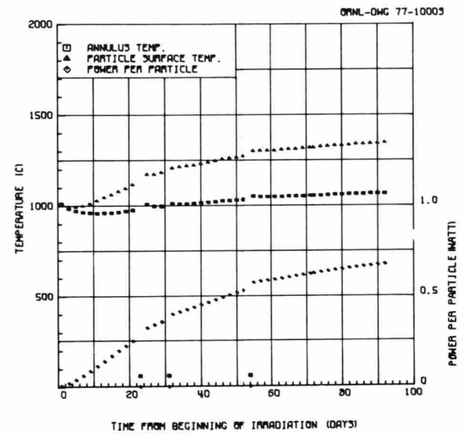

HT-28 PARTICLE HOLDER 43 BATCH OR-2297AHT
878.0 MICRON PARTICLE DIAMETER

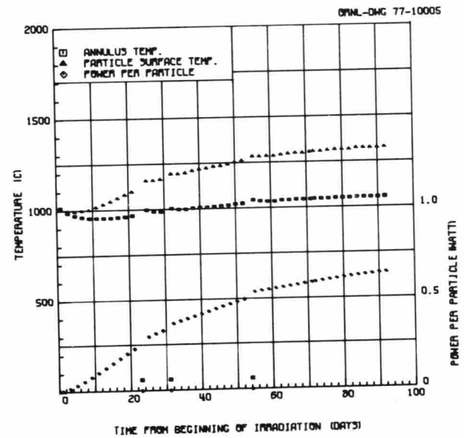

HT-28 PARTICLE HOLDER 45 BATCH OR-2262HT
873.0 MICRON PARTICLE DIAMETER

Fig. A1. Temperature and Power Histories for ORNL Biso-Coated Particles During Irradiation in Capsule HT-28.

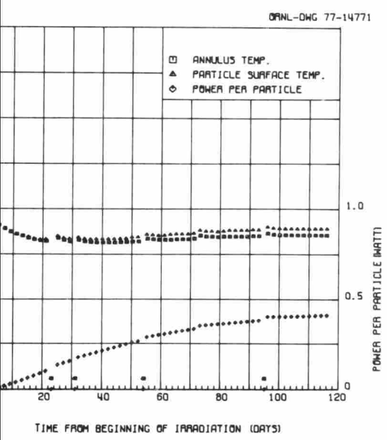

9 PARTICLE HOLDER 2 BATCH OR-2264-HT
883.2 MICRON PARTICLE DIAMETER

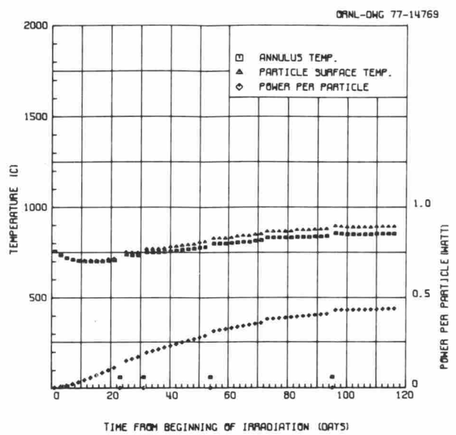

HT-29 PARTICLE HOLDER 4 BATCH OR-2294-HT
871.4 MICRON PARTICLE DIAMETER

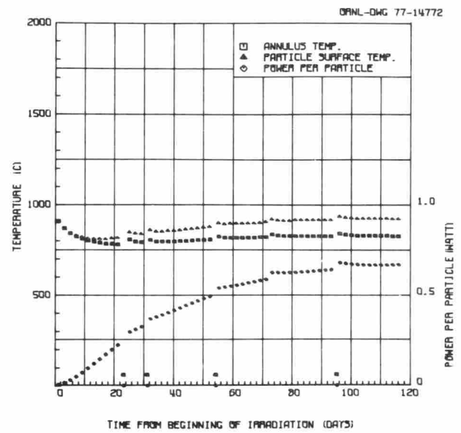

HT-29 PARTICLE HOLDER 15 BATCH OR-2291-HT
872.4 MICRON PARTICLE DIAMETER

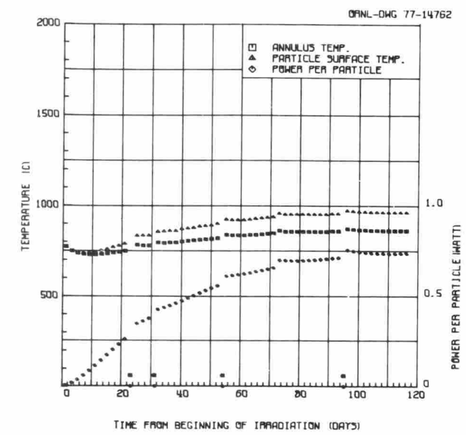

HT-29 PARTICLE HOLDER 23 BATCH OR-2262-HT
873.2 MICRON PARTICLE DIAMETER

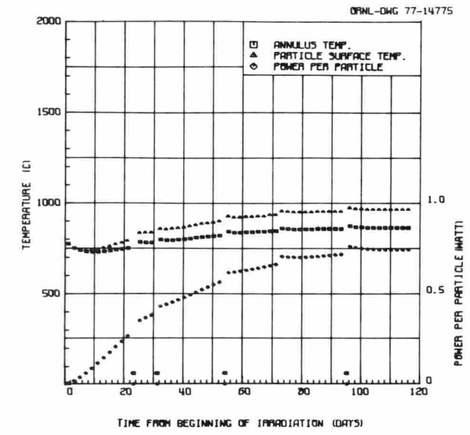

HT-29 PARTICLE HOLDER 29 BATCH OR-2299-HT
880.2 MICRON PARTICLE DIAMETER

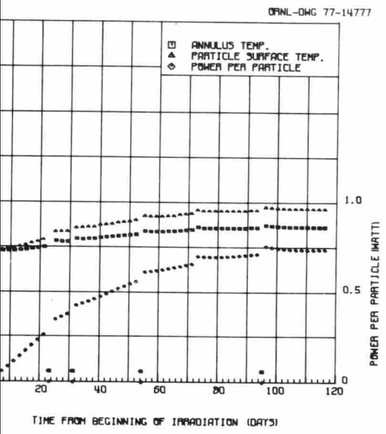

9 PARTICLE HOLDER 30 BATCH OR-2261-HT
875.4 MICRON PARTICLE DIAMETER

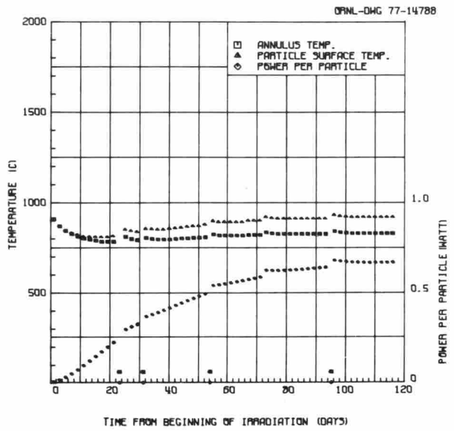

HT-29 PARTICLE HOLDER 38 BATCH OR-2290-HT
886.4 MICRON PARTICLE DIAMETER

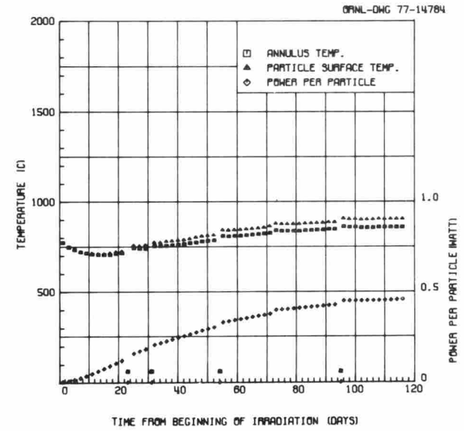

HT-29 PARTICLE HOLDER 48 BATCH OR-2298-HT
863.8 MICRON PARTICLE DIAMETER

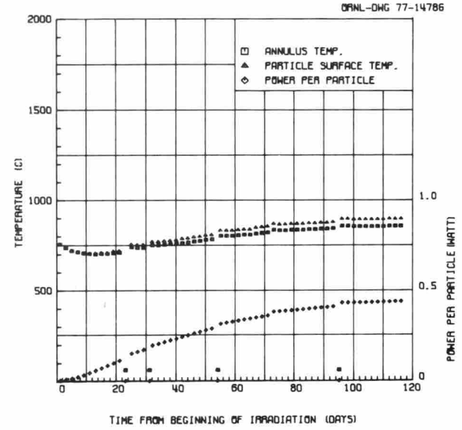

HT-29 PARTICLE HOLDER 49 BATCH OR-2293-HT
879.2 MICRON PARTICLE DIAMETER

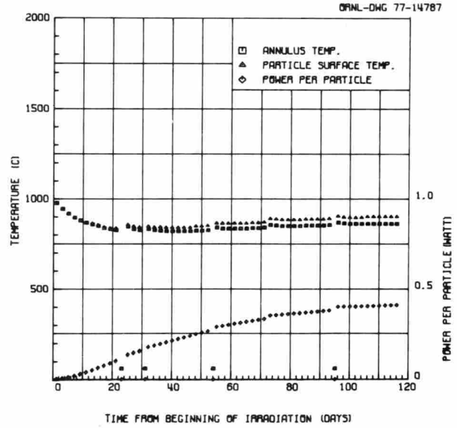

HT-29 PARTICLE HOLDER 51 BATCH OR-2263-HT
872.6 MICRON PARTICLE DIAMETER

Fig. A2. Temperature and Power Histories for ORNL Biso-Coated Particles During Irradiation in Capsule HT-29.

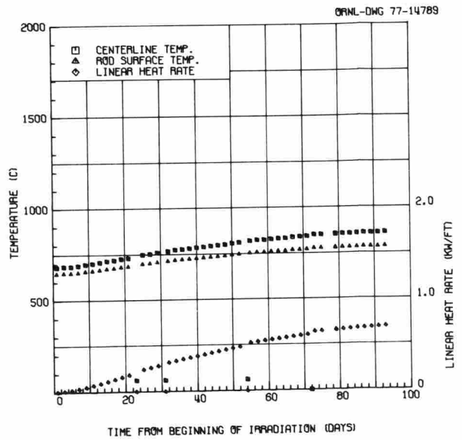

HT-30 FUEL ROD NUMBER 1 BATCH OR-2276-HT
864.0 MICRON PARTICLE DIAMETER

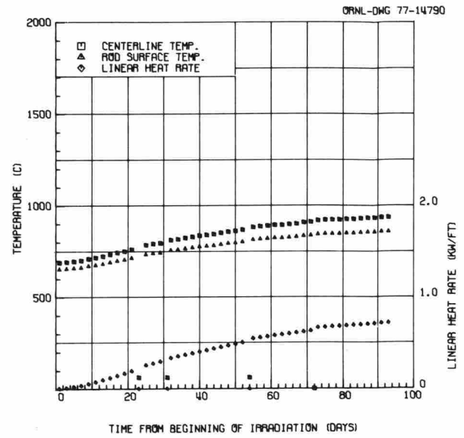

HT-30 FUEL ROD NUMBER 2 BATCH OR-2298-HT
863.8 MICRON PARTICLE DIAMETER

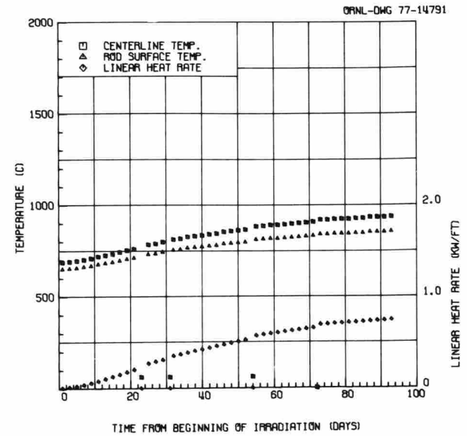

HT-30 FUEL ROD NUMBER 3 BATCH J-488
829.4 MICRON PARTICLE DIAMETER

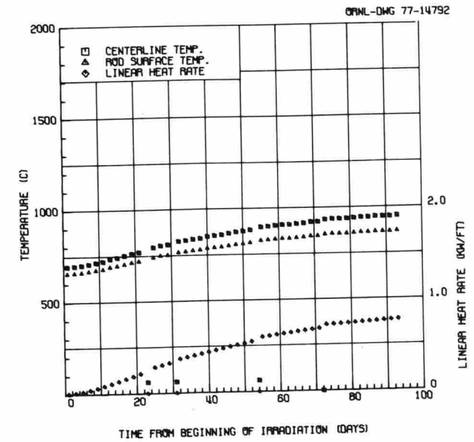

HT-30 FUEL ROD NUMBER 4 BATCH OR-2299-HT
880.2 MICRON PARTICLE DIAMETER

Fig. A3. Temperature and Power Histories for ORNL Fuel Rods in a Low-Temperature Magazine During Irradiation in Capsule HT-30.

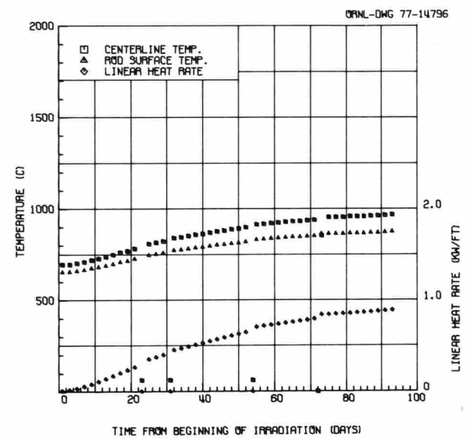

HT-30 FUEL ROD NUMBER 8 BATCH OR-2294-HT
871.4 MICRON PARTICLE DIAMETER

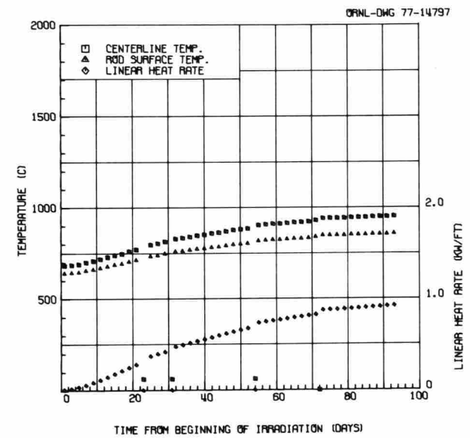

HT-30 FUEL ROD NUMBER 9 BATCH OR-2265-HT
888.6 MICRON PARTICLE DIAMETER

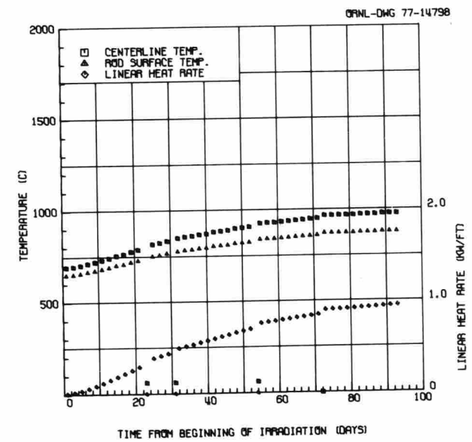

HT-30 FUEL ROD NUMBER 10 BATCH OR-2266-HT
878.2 MICRON PARTICLE DIAMETER

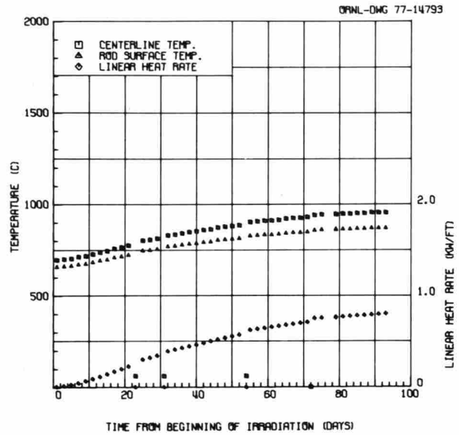

HT-30 FUEL ROD NUMBER 5 BATCH OR-2290-HT
886.4 MICRON PARTICLE DIAMETER

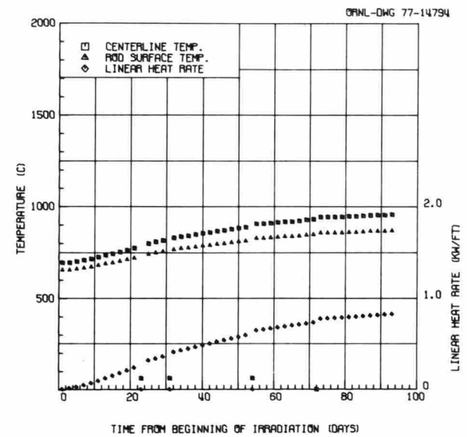

HT-30 FUEL ROD NUMBER 6 BATCH OR-2291-HT
872.4 MICRON PARTICLE DIAMETER

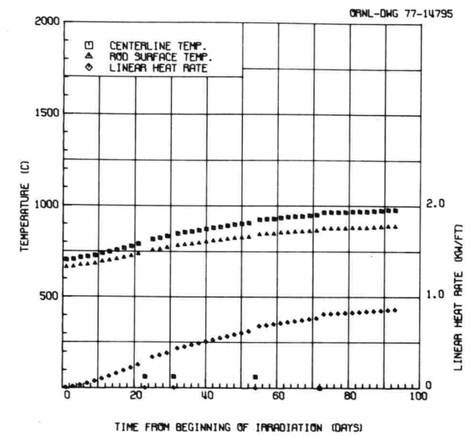

HT-30 FUEL ROD NUMBER 7 BATCH OR-2293-HT
879.2 MICRON PARTICLE DIAMETER

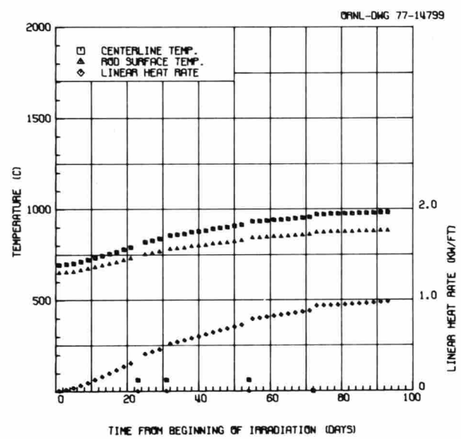

HT-30 FUEL ROD NUMBER 11 BATCH OR-2274-HT
888.0 MICRON PARTICLE DIAMETER

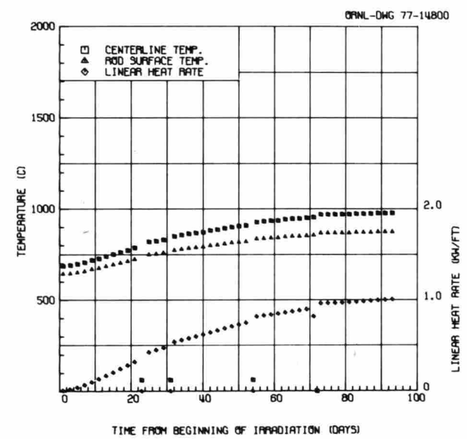

HT-30 FUEL ROD NUMBER 12 BATCH OR-2275-HT
867.8 MICRON PARTICLE DIAMETER

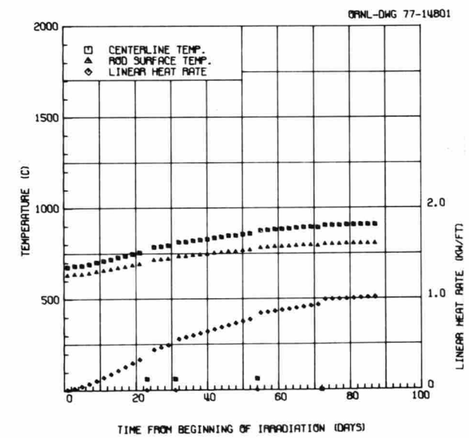

HT-30 FUEL ROD NUMBER 13 BATCH J-489
800.0 MICRON PARTICLE DIAMETER

Fig. A3. (Continued)

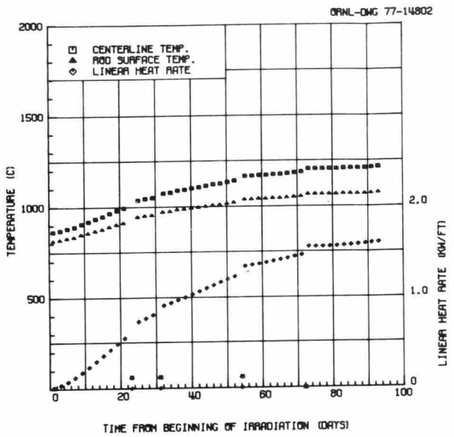

HT-30 FUEL ROD NUMBER 14 BATCH J-489
800.0 MICRON PARTICLE DIAMETER

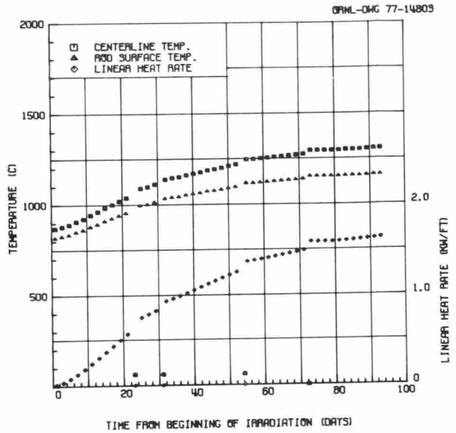

HT-30 FUEL ROD NUMBER 15 BATCH OR-2276-HT
864.0 MICRON PARTICLE DIAMETER

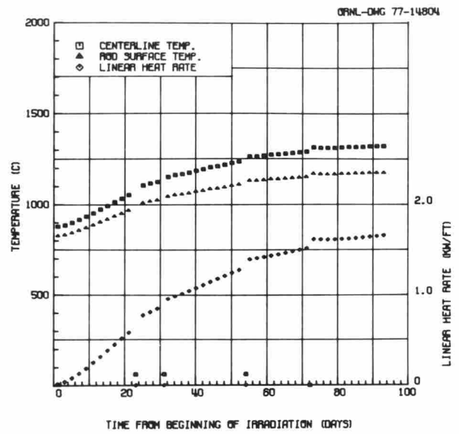

HT-30 FUEL ROD NUMBER 16 BATCH OR-2298-HT
863.8 MICRON PARTICLE DIAMETER

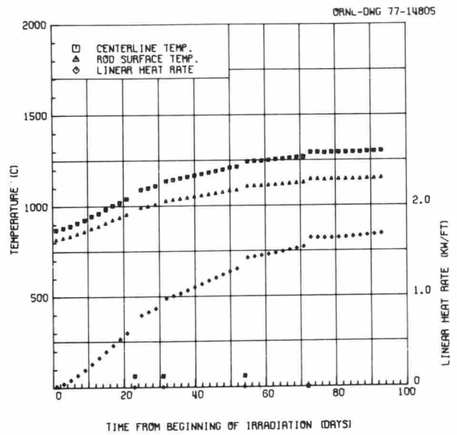

HT-30 FUEL ROD NUMBER 17 BATCH OR-2299-HT
880.2 MICRON PARTICLE DIAMETER

Fig. A4. Temperature and Power Histories for ORNL Fuel Rods in a High-Temperature Magazine During Irradiation in Capsule HT-30.

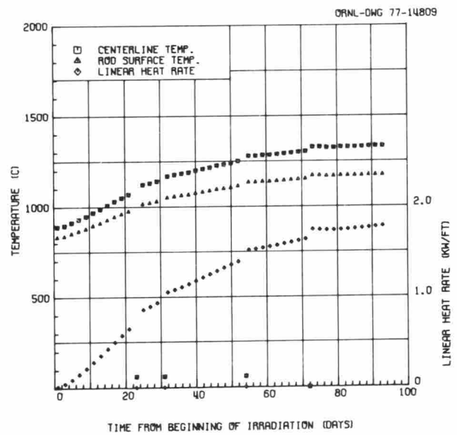

HT-30 FUEL ROD NUMBER 21 BATCH OR-2294-HT
871.4 MICRON PARTICLE DIAMETER

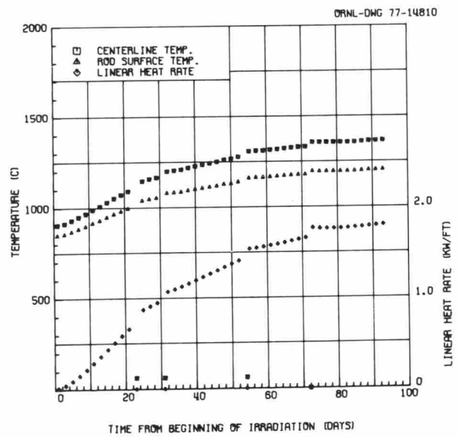

HT-30 FUEL ROD NUMBER 22 BATCH OR-2265-HT
888.6 MICRON PARTICLE DIAMETER

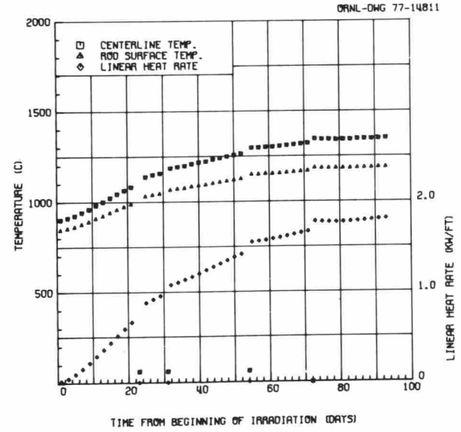

HT-30 FUEL ROD NUMBER 23 BATCH OR-2266-HT
878.2 MICRON PARTICLE DIAMETER

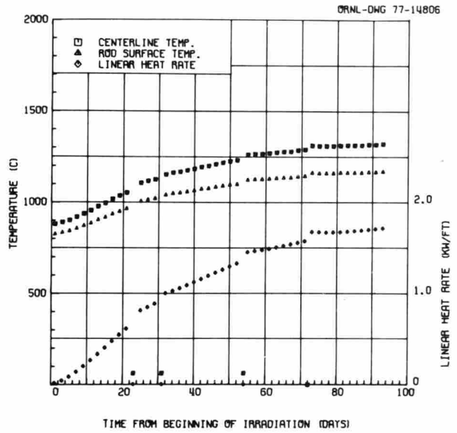

HT-30 FUEL ROD NUMBER 18 BATCH OR-2290-HT
886.4 MICRON PARTICLE DIAMETER

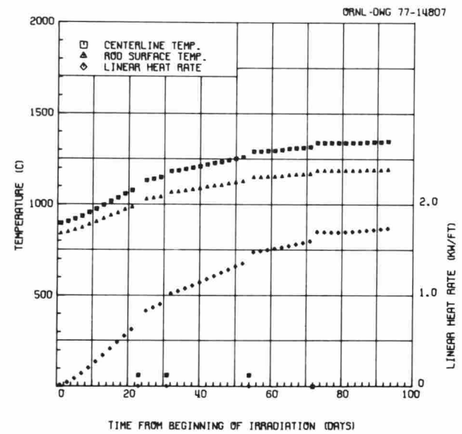

HT-30 FUEL ROD NUMBER 19 BATCH OR-2291-HT
872.4 MICRON PARTICLE DIAMETER

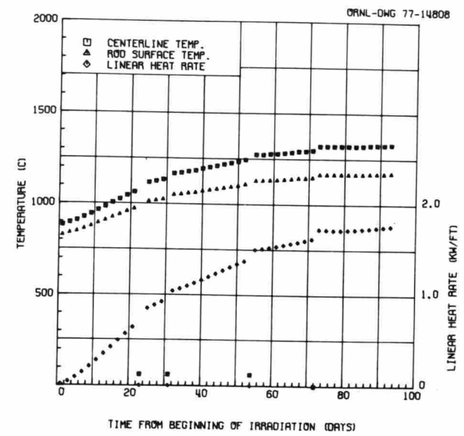

HT-30 FUEL ROD NUMBER 20 BATCH OR-2293-HT
879.2 MICRON PARTICLE DIAMETER

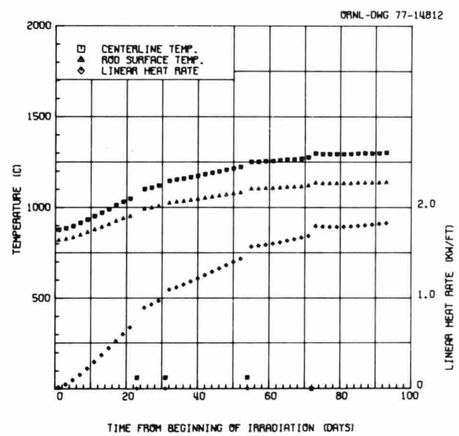

HT-30 FUEL ROD NUMBER 24 BATCH OR-2274-HT
888.0 MICRON PARTICLE DIAMETER

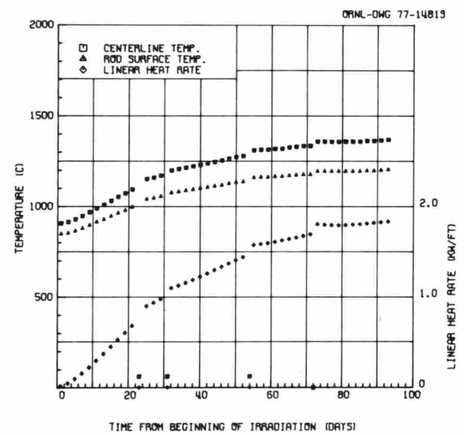

HT-30 FUEL ROD NUMBER 25 BATCH OR-2275-HT
867.8 MICRON PARTICLE DIAMETER

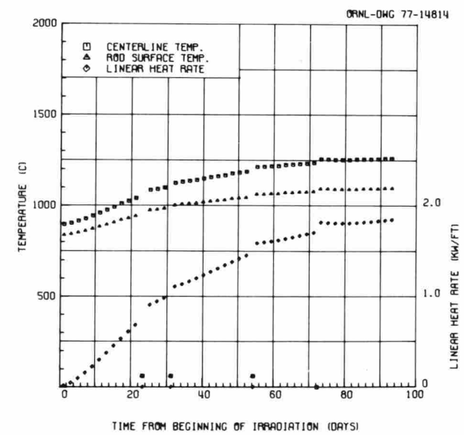

HT-30 FUEL ROD NUMBER 26 BATCH J-488
829.4 MICRON PARTICLE DIAMETER

A4. (Continued)

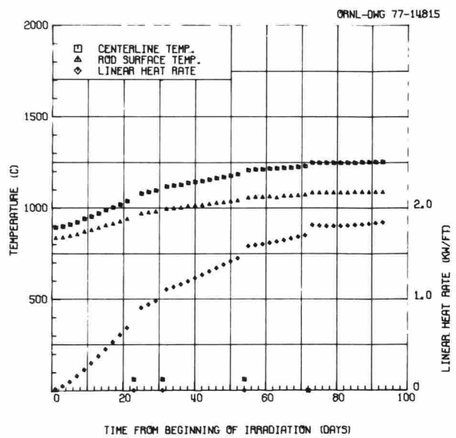

HT-30 FUEL ROD NUMBER 27 BATCH J-490
808.6 MICRON PARTICLE DIAMETER

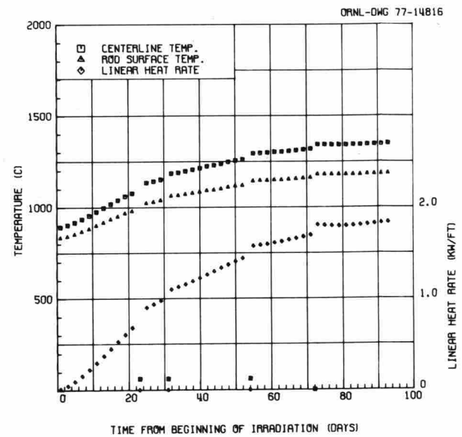

HT-30 FUEL ROD NUMBER 28 BATCH OR-2272-HT
845.6 MICRON PARTICLE DIAMETER

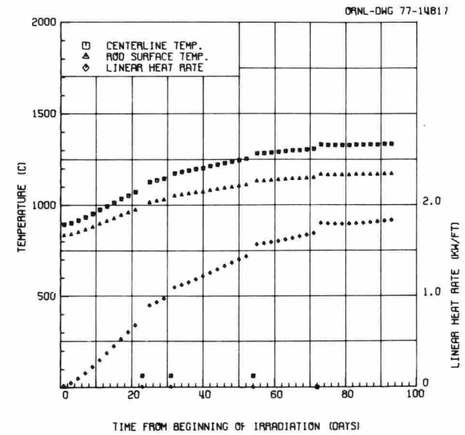

HT-30 FUEL ROD NUMBER 29 BATCH OR-2273-HT
852.4 MICRON PARTICLE DIAMETER

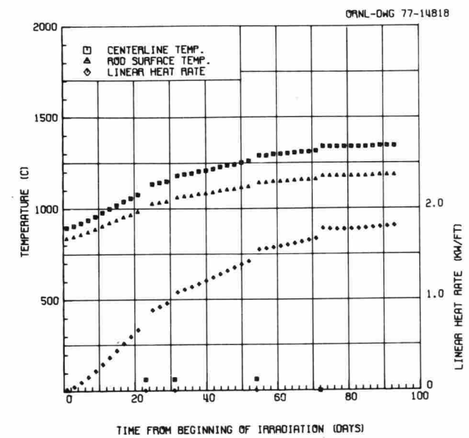

HT-30 FUEL ROD NUMBER 30 BATCH OR-2297-HT
878.4 MICRON PARTICLE DIAMETER

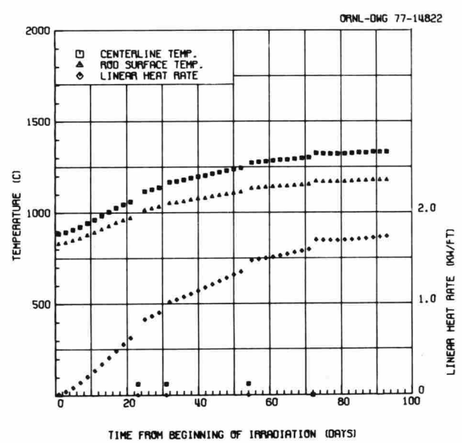

HT-30 FUEL ROD NUMBER 34 BATCH OR-2271-HT
844.8 MICRON PARTICLE DIAMETER

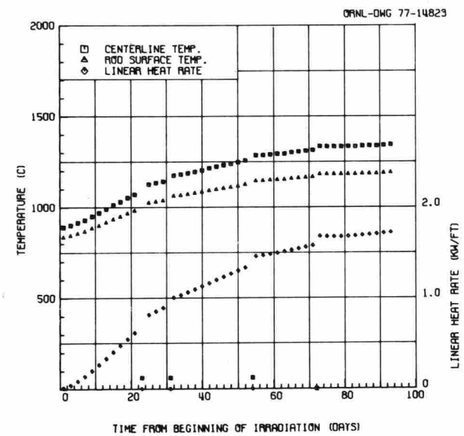

HT-30 FUEL ROD NUMBER 35 BATCH OR-2269-HT
847.4 MICRON PARTICLE DIAMETER

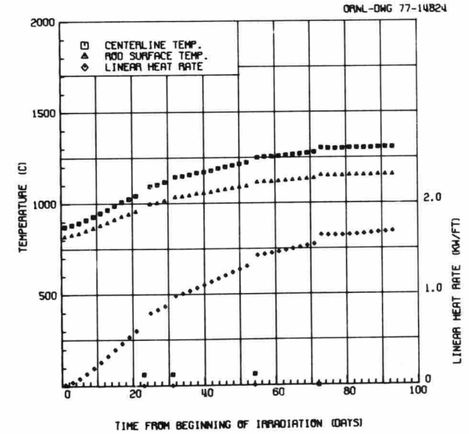

HT-30 FUEL ROD NUMBER 36 BATCH OR-2264-HT
883.2 MICRON PARTICLE DIAMETER

Fig. A5. Temperature and Power Histories for ORNL Fuel Rods in a High-Temperature Magazine During Irradiation in Capsule HT-30.

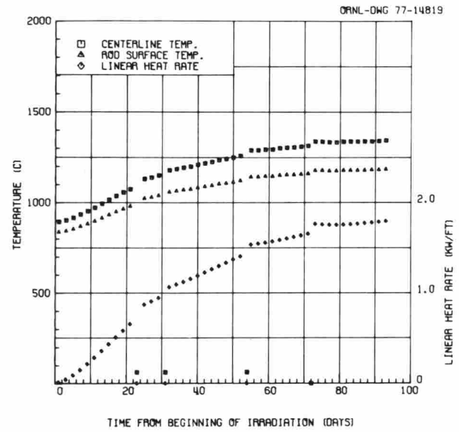

HT-30 FUEL ROD NUMBER 31 BATCH OR-2296-HT
878.8 MICRON PARTICLE DIAMETER

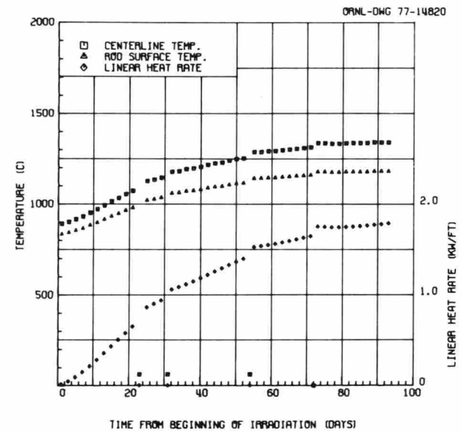

HT-30 FUEL ROD NUMBER 32 BATCH OR-2262-HT
873.2 MICRON PARTICLE DIAMETER

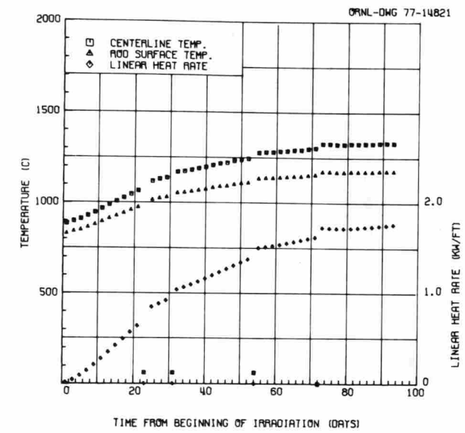

HT-30 FUEL ROD NUMBER 33 BATCH OR-2261-HT
875.4 MICRON PARTICLE DIAMETER

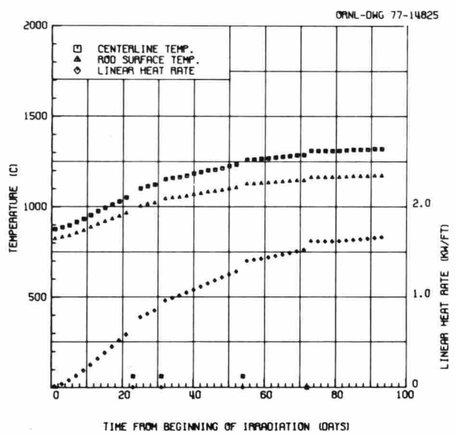

HT-30 FUEL ROD NUMBER 37 BATCH OR-2263-HT
872.6 MICRON PARTICLE DIAMETER

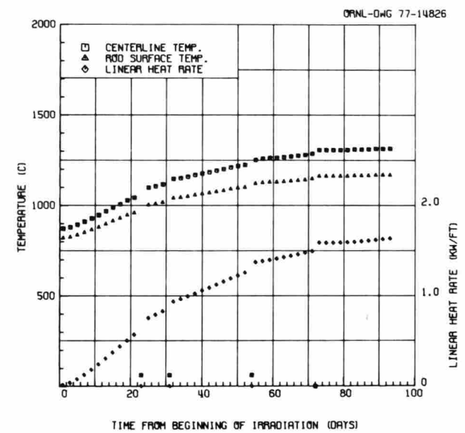

HT-30 FUEL ROD NUMBER 38 BATCH OR-1849-HT
816.2 MICRON PARTICLE DIAMETER

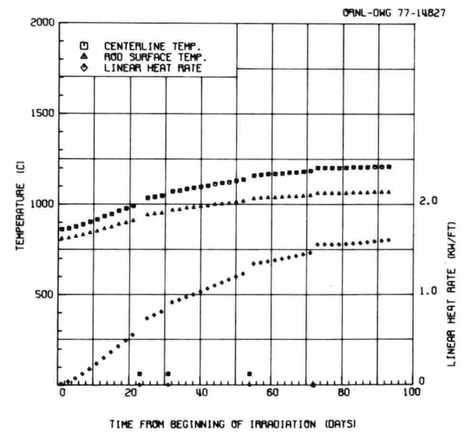

HT-30 FUEL ROD NUMBER 39 BATCH J-491
814.4 MICRON PARTICLE DIAMETER

Fig. A5. (Continued)

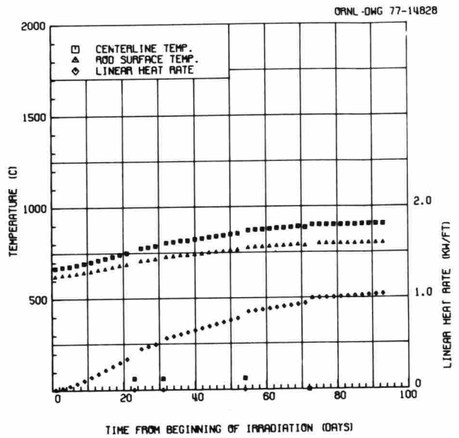

HT-30 FUEL ROD NUMBER 40 BATCH J-491
814.4 MICRON PARTICLE DIAMETER

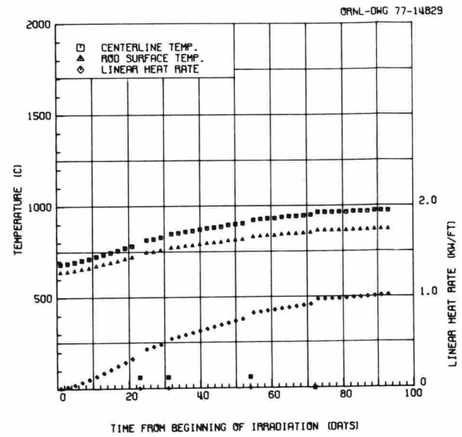

HT-30 FUEL ROD NUMBER 41 BATCH OR-2272-HT
845.6 MICRON PARTICLE DIAMETER

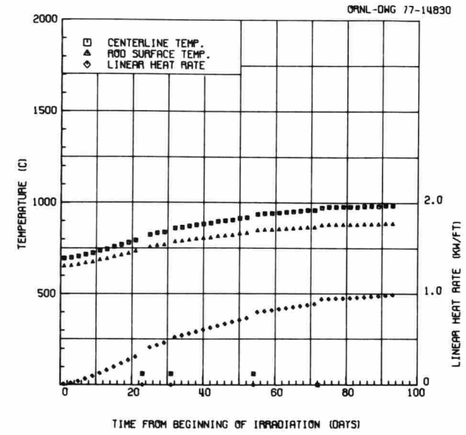

HT-30 FUEL ROD NUMBER 42 BATCH OR-2273-HT
852.4 MICRON PARTICLE DIAMETER

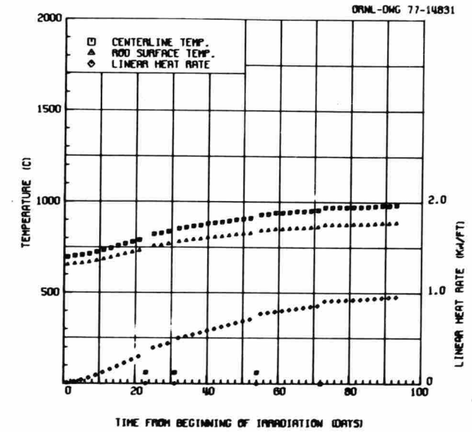

HT-30 FUEL ROD NUMBER 43 BATCH OR-2297-HT
878.4 MICRON PARTICLE DIAMETER

Fig. A6. Temperature and Power Histories for ORNL Fuel Rods in a Low-Temperature Magazine During Irradiation in Capsule HT-30.

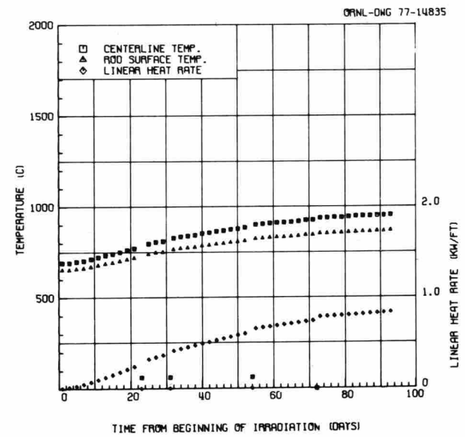

HT-30 FUEL ROD NUMBER 47 BATCH OR-2271-HT
844.8 MICRON PARTICLE DIAMETER

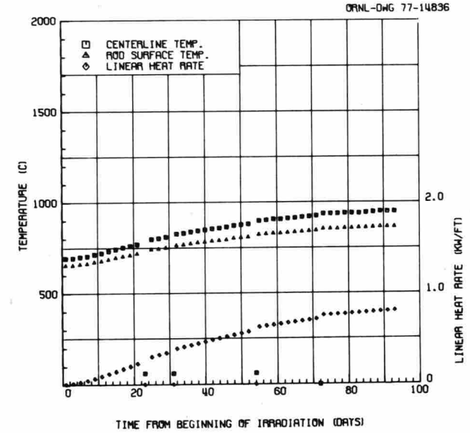

HT-30 FUEL ROD NUMBER 48 BATCH OR-2269-HT
847.4 MICRON PARTICLE DIAMETER

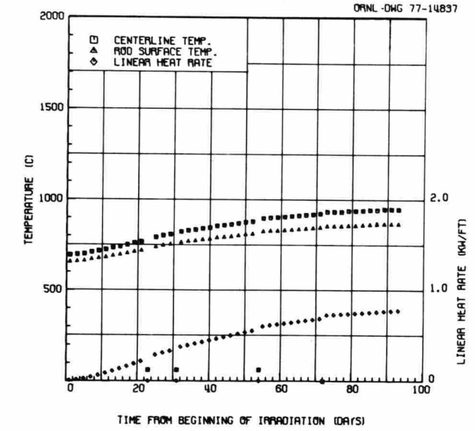

HT-30 FUEL ROD NUMBER 49 BATCH OR-2264-HT
883.2 MICRON PARTICLE DIAMETER

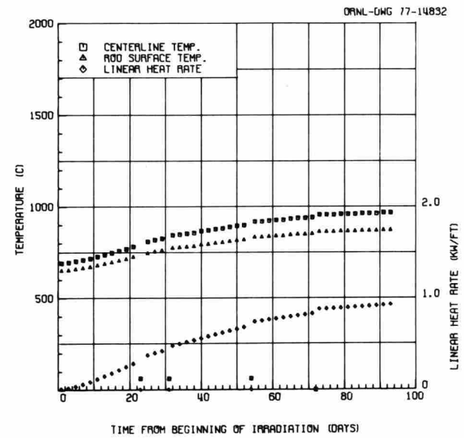

HT-30 FUEL ROD NUMBER 44 BATCH OR-2296-HT
878.8 MICRON PARTICLE DIAMETER

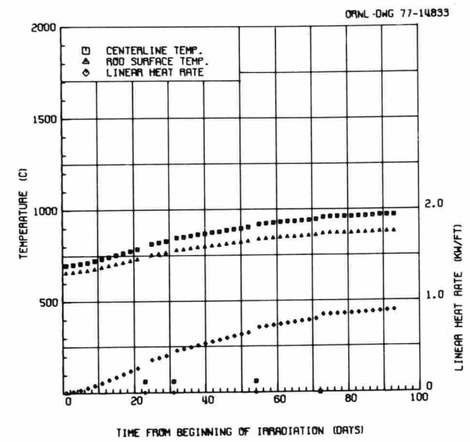

HT-30 FUEL ROD NUMBER 45 BATCH OR-2262-HT
873.2 MICRON PARTICLE DIAMETER

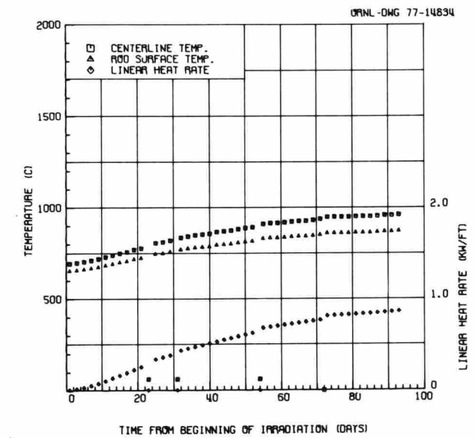

HT-30 FUEL ROD NUMBER 46 BATCH OR-2261-HT
875.4 MICRON PARTICLE DIAMETER

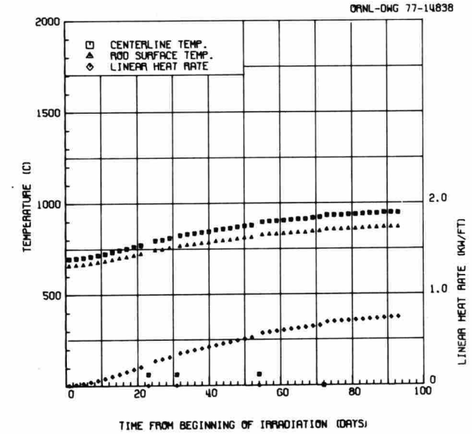

HT-30 FUEL ROD NUMBER 50 BATCH J-490
808.6 MICRON PARTICLE DIAMETER

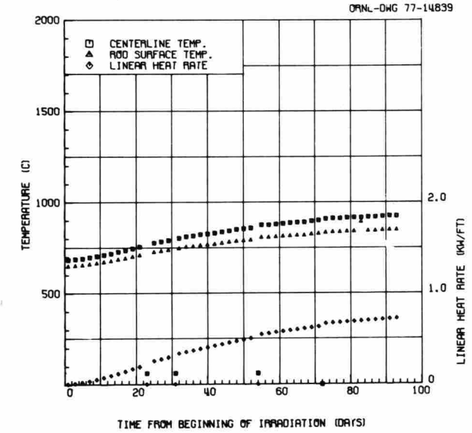

HT-30 FUEL ROD NUMBER 51 BATCH OR-2263-HT
872.6 MICRON PARTICLE DIAMETER

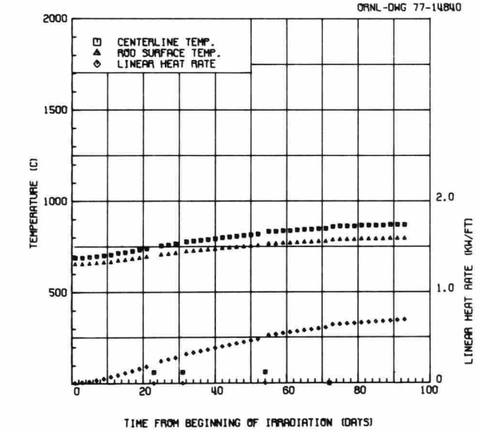

HT-30 FUEL ROD NUMBER 52 BATCH OR-2295-HT
881.4 MICRON PARTICLE DIAMETER

Fig. A6. (Continued)

ORNL/TM-7298
Distribution
Category UC-77

INTERNAL DISTRIBUTION

1–2. Central Research Library
3. Document Reference Section
4–5. Laboratory Records Department
6. Laboratory Records, ORNL RC
7. ORNL Patent Section
8–12. R. L. Beatty
13. A. J. Caputo
14. W. P. Eatherly
15–17. M. R. Hill
18. F. J. Homan
19–28. P. R. Kasten
29. W. J. Lackey
30. T. B. Lindemer
31. J. S. Lin
32–41. E. L. Long, Jr.
42–46. C. S. Morgan
47. R. L. Pearson
48. J M Robbins
49. D. P. Stinton
50. V. J. Tennery
51. R. R. Thoms
52. T. N. Tiegs
53. C. S. Yust
54. A. L. Bement (Consultant)
55. E. H. Kottcamp, Jr. (Consultant)
56. Alan Lawley (Consultant)
57. T. B. Massolski (Consultant)
58. M. J. Mayfield (Consultant)
59. R. H. Redwine (Consultant)
60. J. T. Stringer (Consultant)

EXTERNAL DISTRIBUTION

61–62. DOE, DIVISION OF NUCLEAR POWER DEVELOPMENT, Washington, DC 20545

Director
G. A. Newby

63. SAN-DEVELOPMENT, SAN DIEGO AREA OFFICE, P.O. Box 81325, San Diego, CA 92138

Senior Program Coordinator

64. DOE, SAN FRANCISCO OPERATIONS OFFICE, 1333 Broadway, Wells Fargo Building, Oakland, CA 94612

Manager

65–66. DOE, OAK RIDGE OPERATIONS OFFICE, P.O. Box E, Oak Ridge, TN 37830

Office of Assistant Manager for Energy Research and Development
Director, Nuclear Research and Development Division

67–231. DOE, TECHNICAL INFORMATION CENTER, P.O. Box 62, Oak Ridge, TN 37830

For distribution as shown in TID-4500 Distribution Category, UC-77 (Gas Cooled Reactor Technology)

☆U.S. GOVERNMENT PRINTING OFFICE: 1980-640-245/163